Università degli studi ROMA TRE

Scuola Dottorale in Ingegneria/ PhD School of Engineering

Sezione Scienze dell'Ingegneria Civile/ Civil Engineering Section

XXIII Ciclo

Tesi di Dottorato/ Doctoral Thesis

Extreme waves in coastal areas: landslide tsunami modeling and storm waves long term statistics

Dottorando/ Student: Francesca Montagna

Docente guida/ Tutor: Prof. Leopoldo Franco

Dr. Giorgio Bellotti

Coordinatore del dottorato/ PhD Coordinator: Prof. Leopoldo Franco

Roma, Febbraio 2011

Collana delle tesi di Dottorato di Ricerca
In Scienze dell'Ingegneria Civile
Università degli Studi Roma Tre
Tesi n°28

Acknowledgements

I would like to thank those who made this thesis possible. Firstly my advisors Prof. Leopoldo Franco and Dr. Giorgio Bellotti. Their guidance has been very useful for me, not only to carry out this PhD and this research, but also to make new experiences and to approach problems always questioning and trying to find the best solutions.

I spent a visiting period, during my PhD years, at the IHCantabria. I'm grateful to Prof. Losada, Melisa and Fernando and to all the people I met at the institute for the great experience that I had and for what I learnt.

I have also to thank my colleagues, or friends, Claudia, Alessandro, Antonio, Elisa, Marcello, Michele, Pietro and Federico for all the good times and conversations that we had. They did not just shared their knowledge on engineering items with me, but they made every day spent at the University a pleasure.

A special thanks to my family, who always give me support and important advices.

Thanks also to Davide, for standing by my side during my PhD and for encourage me.

All my friends should deserve to be mentioned for their support and urge to do the best, especially Sara, Sara, Giulia, Giulia and Ilaria.

Abstract

Nowadays many coastal disaster have been experienced all around the world and some of them can be linked to extreme events, as flooding, extreme sea waves, tsunamis, etc. In this thesis two different coastal extreme events, landslide generated tsunamis and extreme sea waves, have been studied because of the high risk related to their occurrence and to the high economical relevance of coastal areas. Because of the different rate of occurrence of the two kind of events, different approaches have been used. The commercial fully 3D numerical model, FLOW 3D, has been used to study landslide generated tsunamis. In particular it has been used to model and analyze fluid-structure interaction and also the generation and propagation in the near and far field of the tsunamis. The model has been firstly successfully validated, comparing the results of numerical simulations to the results of 2D and 3D physical experiments, in particular focusing on landslide generated tsunamis around a conical island. Then the spatial distribution of the generated run-up around the island has been analyzed. The high accuracy achieved suggests the use of the model for few, accurate precomputed inundation maps. The model has also been used to carry out parametric analysis, showing how different parameters influence landslide generated tsunamis and how the numerical model allows to obtain numerous and reliable data with reasonable computational costs. It can finally be noted that the model could be considered an helpful tool for an Early Warning System of tsunami events.

The analysis of extreme sea waves has been carried out considering the fact that almost 20 years of recorded data along the Italian coast are available and so that an accurate extreme statistical analysis can be carried out. In this thesis two different statistical distributions have been applied on the data recorded by eight RON (Rete Ondametrica Nazionale) buoys. In particular a stationary and then a no-stationary GPD-Poisson model have been used. The first one has given results similar to the one obtained with the statistical analysis reported on the Italian Wave Atlas (2004),

the second has analyzed the intra-annual variability of extreme sea waves. This analysis has been carried out considering the statistical distribution parameters as time dependent, varying throughout a year. This procedure allows a better explanation of the variability of extreme significant wave heights throughout a year, its seasonality, and could help, for instance, to define working windows for maritime works in the open sea or to define design waves for seasonal structure.

Sommario

Al giorno d'oggi in tutto il mondo si verificano molti disastri che coinvolgono le zone costiere e spesso questi possono essere legati a eventi estremi come inondazioni, tsunamis, forti mareggiate,etc. In questa tesi sono affrontati e studiati due differenti eventi estremi che possono colpire le zone costiere, gli tsunamis causati da frane e le onde estreme di tempesta. Sono stati affrontati questi temi per la rilevanza economica delle zone costiere e per il grande rischio legato al verificarsi di questi eventi.

Chiaramente gli tsunami generati da frana e le onde estreme di tempesta si verificano con una frequenza molto diversa ed è per questo che i due fenomeni sono stati affontati con due differenti punti di vista ed in particolare con due diversi strumenti. Poichè gli tsunamis hanno una frequenza di accadimento molto bassa ma con grandissimi effetti sulle zone interessate, è di grande rilevanza capire il fenomeno e modellizzarlo, così da poter individuare quali possano essere le zone colpite da un possibile evento, i tempi necessari per una possibile evacuazione delle aree interessate e studiare le conseguenze di un così catastrofico evento.

In questa tesi è stato utilizzato il modello numerico commerciale tridimensionale FLOW-3D per studiare gli tsunamis generati da frane. In particolare il modello è stato utilizzato per modellizzare e analizzare le interazioni fluido-struttura, ovvero l'interazione frana-fluido, e la generazione e propagazione nel campo vicino e lontano delle onde di tsunamis. Il codice di calcolo FLOW-3D è stato applicato con successo al fine di riprodurre il campo di onde generate da frane che impattano violentemente la superficie libera. La validazione è stata effettuata confrontando i risultati numerici con i dati ricavati da prove su modelli fisici 2D e 3D, dando particolare rilievo a esperimenti di laboratorio 3D che riproducono onde di tsunamis generate da frane che scivolano lungo i fianchi di un'isola conica. Successivamente è stata analizzata la risalita delle onde sulle coste dell'isola per evidenziare quali possano essere le zone più colpite. I buoni risultati ottenuti e l'accuratezza del modello suggeriscono l'utilizzo

dello stesso per generare mappe di inondazione che possano essere utilizzate per ipotizzare possibili scenari e quindi definire, ad esempio, eventali zone di evacuazione in un sistema di allerta in tempo reale. Il modello è anche stato utilizzato per studi parametrici per evidenziare quali siano le grandezze che possono maggiormente influenzare il campo di onde generato. Inoltre questi studi evidenziano come il modello possa essere utilizzato per generare una grande mole di dati che siano affidabili, con tempi e costi ridotti rispetto a quelli necessari per ottenere uguali risultati con esperimenti di laboratorio.

Le analisi delle onde estreme di tempesta sono state condotte utilizzando accurati modelli statistici, grazie alla disponibilità di registrazioni ondametriche direzionali di circa 20 anni, raccolte intorno alle coste italiane. In questa tesi sono state applicate, sui dati resi disponibili da otto boe della Rete Ondametrica Nazionale, RON, differenti distribuzioni statistiche. In particolare sono stati utilizzati un modello GPD-Poisson stazionario e uno non stazionario. Il primo ha dato risultati simili a quelli riportati sull'Atlante delle Onde Italiane (2004), ottenuti con un modello statistico stazionario simile a quello in esame, mentre il secondo ha permesso di analizzare la variabilità delle onde estreme di tempesta nell'arco di un anno. Questo è stato possibile considerando i parametri della distribuzione variabili nel tempo, ovvero in un anno. Questa procedura permette di studiare la variabilità delle onde estreme nell'arco dell'anno, e quindi nelle diverse stagioni, e può rivelarsi molto utile nel campo dell'ingegneria marittima, ad esempio, per definire finestre temporali di lavoro in mare aperto o definire onde di progetto per strutture a carattere stagionale.

Contents

List of Figures

List of Tables

List of Symbol

NS	Navier-Stokes Equations	[...]
RANS	Reynolds Averaged Navier-Stokes Equations	[...]
LSWE	Linear Shallow Water Equations	[...]
NLSWE	Nonlinear Shallow Water Equations	[...]
VOF	Volume of Fluid	[...]
ζ	Landslide falling height	$[m]$
η	Water free surface elevation	$[m]$
R	Run-up gauges	[...]
S	Off-shore sea level gauges	[...]
$R_{u,d)}^{(1,2)}$	First/second wave run-up/down	$[m]$
$A_{u,d)}^{(1,2)}$	Positive/negative amplitude of the first/second wave	$[m]$
r, θ	Curvilinear coordinate	$[m,^\circ]$
a,b,c	Ellipsoid semiaxis	$[m]$
Tr	Return Period	$[year]$
Hs	Significant wave height	$[m]$
t	time	$[s]$
GEV	Generalized Extreme Value Distribution	[...]
POT	Peak Over Threshold	[...]
GPD-Poisson	Generalized Pareto Distribution	[...]
u	Threshold	$[m]$
ν	Mean annual number of occurrence	[...]
μ	Location parameter (GEV)	$[m]$
ψ	Scale parameter (GEV)	[...]
ξ	Shape parameter (GEV, GPD)	[...]
λ	Poisson parameter	$[m]$
σ	Scale parameter (GPD)	[...]
l	log-likelihood function	[...]

Chapter 1

Introduction

1.1 Introduction and motivation

In recent years a growing number of disasters in coastal zones due to large typhoons, sea level rise, tsunami triggered by large earthquakes and landslides has been experienced. In the 1990s, more than 90% of those killed in natural disasters lost their lives in hydro-meteorological events (mainly droughts, floods and wind storms, GEO-3) (Keasavan and Swaminathan, 2006). As highlighted in Martinelli et al. (2010), all the available assessments over the last 20 years up to the most recent IPCC Assessment (Alcamo et al., 2007) and the results of the SURVAS Project (Nicholls and de la Vega-Leinert, 2008) show that Europe's coasts are threatened by sea level rise and climate change in a variety of ways. Significant coastal areas in countries such as England, Denmark, Germany, Italy, Poland and most especially the Netherlands are already below normal high tide levels. Sea level rise will cause several direct impacts, such as inundation and displacement of wetlands and lowlands, coastal erosion particularly adjacent to inlets, increased storm flooding and damage (Nicholls et al., 2007). So in coastal zones spatial planning it is sensible to consider changes relating to the behaviour of the sea.

As the risk of flooding is a product of both the probability of a flood event and its potential consequences, it is necessary to study both carefully (Hawkes et al. 2008). An increasing relevance is nowadays put on these items and this is confirmed, for instance, by the FLOODsite Project. In November 2007, the Parliament and Council of the European Union published the wording of a new European Directive on the assessment and management of flood risks and FLOODsite is listed as one of the European actions which support the Directive (http://www.floodsite.net/html/project_overview.htm).

It must further be highlighted that a great risk is also associated to tsunami flooding. Many studies have been carried out on this topic and the interest on it is testified, for instance, by the great tsunami program (2008-2017) of NOAA (National Oceanographic and Atmospheric Administration) to forecast, detect and mitigate tsunami. Also in Italy tsunamis risk has become a subject of several studies and in between them it could be mentioned the Italian PRIN project of 2004 and 2007 on tsunami modeling, prediction and on the development of a real time warning system.
Because of these evidences, for a complete design of maritime structures and for a correct coastal management, extreme sea waves and tsunamis must both be considered, because not only economical costs but also the risks associated to safety and to environmental quality must be accounted for. In the maritime field the higher is the global risk associated to the structure, the higher is the level of the external hydraulic loads considered for the design. Usually for maritime works a design wave is chosen. It has to represent the environmental conditions considered dangerous for the stability of maritime structures, also accounting for storm surge and sea level changes. In general the design wave can either be a significant wave, representing a sea state, or an individual wave, representing the maximum height within a given sea state; for exceptional areas or structures, as a nuclear plant near the coast, also tsunami waves could be considered as design waves.
The risk associated to the design wave is generally specified by means of the return period (Tr) of sea states and by the occurrence probability during the work's lifetime. When considering wind generated waves this is possible because of available recorded or hindcasted data that allow to evaluate, with statistical tools, the occurrence of extreme events. When a tsunami wave is chosen as a design wave it is not possible to use statistical tools, due to lack of data. An alternative to the statistical study is to compute possible tsunami scenarios and to evaluate, with numerical or analytical tools, the generated and propagating waves. In this way it would be possible to assess the tsunami hazard of a site and to correctly design the structures. Nowadays many researches are underway in order to both predict extreme events and protect coastal areas. In Italy almost all maritime works have been designed considering wind generated sea state but, because of the knowledge of some tsunami events occurred along the Italian coast in the past, the interest on this dangerous phenomena is increased although tsunamis have not a devastating effect on maritime structures.

1.2 Tsunamis

Tsunamis are long waves triggered by a sudden disturbance of the sea/ocean floor or the sea/ocean surface, which is usually caused by earthquakes, landslides or volcanic eruptions. The word tsunamis comes from the Japanese, with the meaning "harbor wave", and is related to the excitation of seiches induced into a harbor when the long tsunamis wave enters the closed basin. Both energy and momentum can take tsunamis waves thousands of kilometers across the open ocean, carrying destruction on far shores hours after the impulse generating event. In deep water conditions, tsunamis can travel at celerities of 600-800 kilometers per hour, presenting wave heights of the order of some centimeters, wavelengths of the order of hundreds of kilometers. As the wave approaches shallow water near the coast, the wave celerity is reduced and the wave height significantly increases, sometimes exceeding even the value of 20 m, with wave periods up to 20/30 minutes. Tsunamis are able to produce high wave run-ups which can flood the coastal areas and even destroy a coastal city, and they are so dangerous because can be rarely detected in open seas. Therefore the analysis of this phenomenon is very important, especially considering the safety aspects related to the human activities along the coasts. Tsunamis waves have largely occurred in the oceans and well known is the tragic event of Sumatra Island, in the Indian Ocean, occurred the 26^{th} of December 2004 which caused the loss of about 300,000 human lives; however very dangerous events have been also registered in the Mediterranean sea, such as that occurred the 21^{st} of July, AD 365, at Alexandria, which caused 50,000 deaths, and the one occurred the December 28^{th}, 1908, at Messina, which caused 120,000 deaths. Regarding the Mediterranean Sea, it is worth to mention the event occurred at the Stromboli volcano, on December 30, 2002, because it is the case study of the present work. No human lives were lost, but the wave damaged properties along the shorelines of the Stromboli island and excited resonant modes of harbors along the coasts of Calabria.

1.2.1 Tsunamis generated by landslides

Waves generated by submarine or subaerial landslides are a particular type of tsunami waves. They can be triggered by landslides falling in artificial reservoirs, as the event of the Vayont reservoir, Italy, 1963 (Panizzo et al., 2005) or in natural lakes, or moreover in sea shorelines, as the event of Lituya Bay, Alaska, 1958 (Miller, 1960; Fritz et al., 2001), where the induced run-up is the largest known, or the one of Stromboli volcano, Italy, 2002 (Tinti et al., 2005, 2006a, 2006b). Differently from tsunami waves triggered by a submarine disturbance, the subaerial landslide generated waves produce splashes and complex three dimensional water flows in the vicinity of the impact area. It also could be underlined that the generation process, in case of landslide generated tsunamis, takes a longer time than in case of earthquake tsunamis and that, because of the different areas and volumes involved in the generation, coseismic displacements or vertical seafloor deformations often generate tsunamis with larger wavelength and longer period.

When impulse waves are generated directly on the shore, they can remain close to the coast due to refraction phenomena, being them a great hazards for coastal populations and infrastructures, because of their consequences of flood and inundation, and because of the little time for warning due to their proximity to the shore. In case of artificial reservoirs the most dramatic consequences are dam overtopping, flooding of the lake shorelines, and seiching waves of the basin. It is clear how the understanding and the forecasting of landslide generated waves is important both for the safety of people and properties which are close to the impact area, and for the artificial reservoirs and dam management.

The generation of impulsive waves due to the impact of subaerial landslide into water is a complex phenomenon, involving several physical aspects. A first simplification can be done considering the whole phenomenon distinct in four phases, as it was proposed by Huber and Hager (1997). As it can be seen from the sketch in Figure 1.1, in the first step the landslide starts moving, accelerates and then falls into water. The study of this part of the process lies in the scientific field of geology and soil mechanics. Step 2 sketches the impact of the landslide into water. This part of the process is at the base of wave generation, due to the energy exchange mechanism between the landslide and the water. The principal landslide parameters, (i.e. volume, impact velocity, density, shape of the front, slope inclination angle) influence the features of the subsequent water wave motion. A qualitative description of the generation of waves by subaerial landslides could be found in Liu et al. (2005) and in Di Risio et al. (2009a). When a landslide enters the water body, generates a leading positive radiating wave pushing the fluid ahead, then, once the landslide is completely submerged, a trailing wave through is generated. Because of the strong free surface gradient generated alongshore, converging flows collide and rebound along the centerline of the landslide. The rebound then generates an high positive wave radiating offshore. Then the perturbation travels for long distances, producing high water waves in the shallow water areas, so it comes the third step, where impulsive waves propagate into the reservoir or in the open sea, presenting a wave energy dispersion which is both longitudinal and directional. During the propagation wave features change as a function of the water depth, and refraction, diffraction and shoaling may occur. Finally, step 4 is related to the impulsive wave interaction with shorelines or structures.

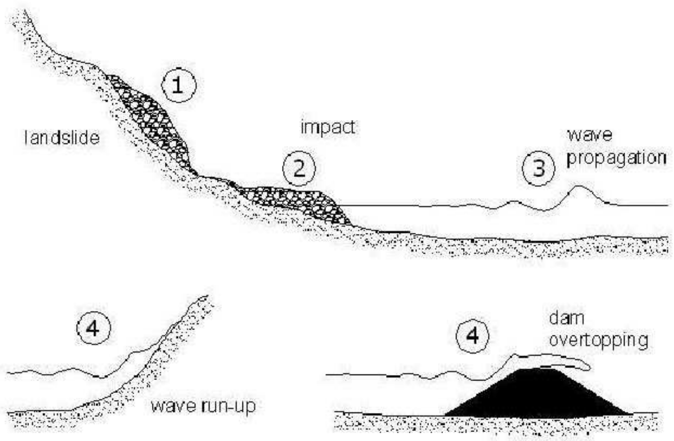

Figure 1.1: Principal phases in the phenomenon of subaerial landslide generated waves.

As far as the generated water waves are concerned, they may present very different shapes and dispersive features. Prins (1958), Wiegel et al. (1970) and Noda (1970) performed several physical experiments generating impulse waves by the falling of a solid block in a two dimensional wave flume. They concluded that, depending on the local water depth, the energy exchange between the landslide and the water, and the landslide volume, impact waves present different characteristics. Their experimental observation can be summarized by Figure 1.2, which presents a map of different wave types observed during impulse waves generation due to the vertical fall of a box (λ is the box width, d is the local water depth, $Fr = v/\sqrt{gd}$ is the dimensionless box falling velocity; figure 1.3).

The typical time series of water surface elevation at a given point are represented on the right part of Figure 1.2. Basically four types of impact waves were observed by these authors: (A) leading wave with oscillatory

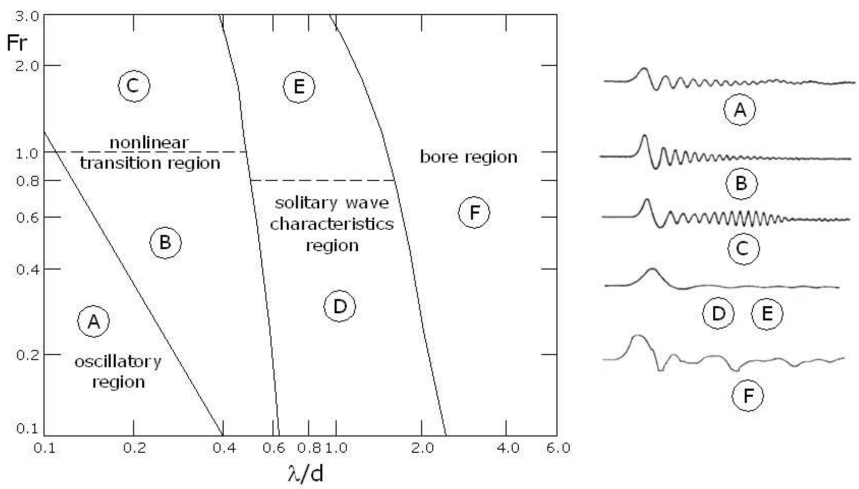

Figure 1.2: Different types of impulse waves defined as function of the landslide volume, represented by the dimensionless parameter λ/d, and the landslide velocity, represented by the Froude number Fr (picture taken from Noda, 1970).

wave characteristics, (B–C) leading wave with solitary wave characteristics, followed by a trough connecting it with the dispersive wave pattern, (D–E) leading wave being a single wave with solitary wave characteristics, separated by the dispersive wave pattern, (F) solitary wave with complex form (bore in the first stage). As a general rule the generated waves type vary from (A) to (F) gradually as the values of λ/d and Fr increase. When the dimensions of the falling body are large in comparison to water depth, solitary waves are to be expected, viceversa a train of dispersive waves is likely to be generated in relatively deep water.

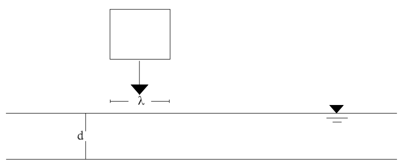

Figure 1.3: Definition of λ and d.

The tsunamis generation and propagation can be analyzed in the *near field* (in the vicinity of the impact area) or in the *far field* (where propagation takes place). The water wave field can be recognized to change from the *near field*, where the water motion is complex and threedimensional, presenting splashes and bores, to the *far field*, where the water motion is dominated by propagating water waves. In the definition of *near* or *far field*, some further considerations can be made. Considering the ratio between the volume of the landslide and that of the water body, where impulsive flows take place, three different cases can be recognized (see Figure 1.4): the first case (A), is the case of a large landslide falling into a small reservoir, the third case (C) contrary, is when a small landslide falls into a large reservoir or in the open sea, and the second panel (B) of Figure 1.4 shows an intermediate case. The situation sketched in the panel A, is the limit of a case where the far field does not exist, that one on the panel C, shows a case where the near field is small compared to the far field, the intermediate situation (panel B) consists of near field and far field of comparable extents. So it is important to consider which could be the dominant aspects of the phenomenon before modeling subaerial landslide generated waves (Cecioni 2010).

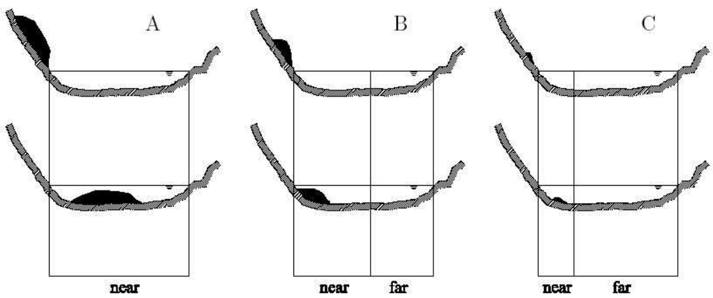

Figure 1.4: Three different main cases defined as a function of the ratio between the volume of the landslide and that of the water body.

1.3 Extreme wave climate

Many extreme wave climate events have caused big catastrophes. There could be mentioned recent events as the hurricane Mitch of 1998, Katrina of 2005, or, just focusing on the Mediterranean sea, the Parsifal Storm on

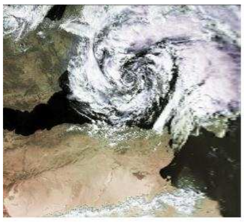

Figure 1.5: Cyclone over the Mediterranean Sea, October 1996.(Credit: NASA / ESA).

November the 2nd 1995 that in the Gulf of Lion sank the 16 meter yacht Parsifal claiming six lives out of the nine member crew (Bertotti, 1998), or the exceptional storm of December the 20th 1999 in the Tyrrhenian Sea.

The geographical pattern of extreme wind waves is related to the presence of strong winds. In the Mediterranean region waves, as a large spectrum of environmental variables and phenomena, are associated with cyclones (figure 1.5). These are characterized by inward spiraling winds that rotate counter clockwise centered on areas of low atmospheric pressure. The study of Lionello et al. (2006) show that cyclones are important when information more complete than that provided by the average geopotential (or sea level pressure) field is required and when aspects of the probability distribution characterizing the statistics of the atmospheric circulation besides its average values are investigated. Consequently, statistical analysis of cyclones is important especially for the "tails" of probability distributions, that is the part characterizing extremes values of variables such as precipitation, winds, waves, storm surges. The Mediterranean area, although located to the south of the main Atlantic storm track that more directly affects western and northern Europe, is quite frequently subjected to sudden events of extreme and adverse weather, often having high social and economic impacts. It is important to note that the link between the intensity of cyclones and hazardous extreme events is not simple and different characteristics can be involved as different impacts are considered. The intensity of circulation (winds), precipitation (with consequent floods) and of the cyclone itself (measured as the minimum value of the sea level pressure or the strength of the overall associated circulation) are not necessarily related in a simple (linear) way and for that reason in Lionello et al. (2006) all these phenomena are analyzed.

The highest possible waves in many locations are often associated with the contribution of swell to the combined wave field and they occur especially during a certain season of a year. In the Mediterranean region, because of the limiting fetch, contribution of swell is small and, depending on the period of the year and on the location, extreme wave condition could be found in the western or in the eastern Mediterranean Sea. Table 1.1 shows the most active storm regions of the Mediterranean and their seasonality (Lionello et al.2006).

Table 1.1: Cyclogenetic regions in the Mediterranean area, respective seasons with significant activity and average cyclones radius (Lionello et al. 2006).

AREA	SEASONALITY	RADIUS(KM)
Sahara	spring-summer	530-590
Gulf of Genova	whole year	380-530
Southern Italy	winter	520
Cyprus	spring-summer	330-460
Middle East	spring-summer	320-460
Aegean Sea	winter, spring	500
Black Sea	Whole year	380-400
Iberia Peninsula	spring	410

Extreme wave climate could be considered as a limiting factor both in the biology and morphology of the coastal area and also determines the uses of the coast, making their characterization so necessary for coastal management and maritime works. Within this context, in order to study the occurrence of extreme wave climate, it is possible to focus on the extreme values of significant wave heights. Fortunately in the last decades almost all over the world wave measurements have started, allowing to generate consistent database of significant wave heights.

There are four major sources of wave data (buoy data, voluntary observing ship (VOS) data, model hindcasts and satellite altimeter data) that can contribute to study wave climate. Buoy data, although they usually present gaps in their records and do not have an homogeneous spatial distribution, are the most reliable records, especially when considering extreme values.

In particular different research works have been carried out to study extreme events and wave climate variability along the Italian coast, thanks also to the available data recorded by the RON, the National Wave

Recording Network (Piscopia et al, 2002; Lionello et al. 2005; Lionello et al. 2008). One of the most complete and accurate study, called The Italian Wave Atlas, was published in 2004 by APAT (now ISPRA, Istituto Superiore, per la Protezione e la Ricerca Ambientale) and by University of Roma Tre. In this Atlas useful information on average and extreme directional wave characteristics for coastal engineering designs has been provided. These have been obtained by a large and accurate statistical analysis on the recorded data by the RON, active from 1989. The study was motivated by the fact that, because of the complex geographical configuration of the peninsula and the variable exposure to sea wind of the Italian coast, the wave climate is extremely variable between one location and the other. It is also evident that in maritime project a detailed knowledge of local directional wave climate in necessary.

1.4 Aims and structure of the present work

Coastal extreme events in the recent past have captured scientific attention, because of the high risk related to their occurrence and to the high economical relevance of coastal areas. The design of maritime works and coastal management is conditional upon them. For that reason many mathematical, physical and statistical models have been implemented to get better insight the processes and to plan defense strategies.

This work is structured in two parts.

The first part deals with landslide generated tsunamis. They are studied using a 3D numerical model, FLOW 3-D, in order to simulate, understand and predict the generation and propagation of tsunami waves. In this work the usefulness and the accuracy of the model will arise. It will be also shown that the model is applicable at reasonable costs for few accurate simulations that may be used for preparing precomputed inundation maps of coasts prone to the risk of tsunamis inundation, an so to evaluate quickly, in case of occurrence of a tsunami, the areas that must be evacuated.

The second deals with extreme wind waves. They are studied with a no-stationary statistical approach, able to model extreme sea waves seasonality. This approach allows to improve the knowledge of some important natural coastal processes and to refine the definition of a given return-period wave height, providing more accurate design wave conditions for maritime works.

The present document is structured in 4 chapters. In the first one the topics and the aims of the work are already outlined. *Chapter 2* deals with landslide generated tsunami. Firstly a literature review on tsunami modeling, and, in particular, about landslide generated tsunamis is presented and then the numerical model, FLOW-3D, is used to simulate landslide tsunami generation and propagation, is illustrated and validated using the results of two physical experiments. The results of some parametric studies carried out using FLOW-3D are then described. Conclusions on landslide generated tsunamis follow. In *Chapter 3* a literature review about statistics of extreme events and, in particular, on extreme storm waves is reported. Then the results of a new statistical model applied on the extensive wave data set collected around the Italian coasts are presented. Conclusions on the Italian extreme storm waves follow. *Chapter 4* presents the general conclusions of this work.

Chapter 2

Numerical investigation on landslide generated tsunamis

2.1 Tsunami waves modeling. Literature review

Tsunamis are generally regarded as long waves in comparison with wind generated waves. Thus traditionally mathematical models based on the Nonlinear Shallow Waters Equations (NLSWE) were used to simulate the wave field. Other research works reveal that linear shallow water theory is also suitable to model tsunami propagation, in the regions where the wave amplitude is much smaller than the water depth, i.e. the ocean zone before the shoaling effects. The entire process of tsunami generation, evolution and run-up, however, needs a complete model that considers both frequency dispersion and nonlinearity, because the former becomes important when a tsunami propagates for a long distance and the latter could also dominate as a tsunami enters the run-up phase. During the generation and run-up phases is also extremely important to take into account fluid/structure interaction. The NLSWE however, although able of taking into account amplitude-dispersion of the waves, cannot reproduce the frequency-dispersion, which as mentioned before may be of relevant importance. When studying the propagation of these waves over large geographical areas it is common that the height of tsunamis is several order of magnitudes smaller than the water depth. The typical wave height of a large, destructive tsunamis is of 1 m, while the water depth over which it propagates may be of 100, 1000 m. The steepness of the waves is also extremely small, since the length is of the order of the kilometers. This suggests that nonlinear effects may be neglected or at least may be of secondary importance in comparison to the proper reproduction of the frequency-dispersion. It is worth to mention however that the above considerations mostly apply for the far field and not in proximity of the coast (i.e. in very shallow waters), where the nonlinear effects become important. Run-up of long waves on beaches of complicated bathymetry is studied numerically, mainly in the framework of shallow-water theory, see for instance (Liu et al. 1995, Brocchini et al. 2001). When a tsunami occurs the wave field has large variability in temporal and spatial scales, especially with different near-shore conditions, where full 3-D flow characteristics appear.

In the last decades the Boussinesq-type equations (Peregrine, 1967; Madsen et al, 1991; Wei and Kirby, 1995; Nwogu, 1993) have therefore become the most suitable model for the tsunamis simulation. These equations allow the reproduction of wave nonlinearity, relevant in the coastal shallow areas, but they take into account of a weakly frequency dispersion of water waves, thus being able to simulate its propagation a bit further in the deep water conditions. Several versions of this type of models are available. The complexity of the model equations (and therefore the computational costs), however grows with the increased ability of the models of reproducing the nonlinear and the frequency-dispersive effects.

Other efforts have been carried out in the numerical modeling to properly simulate also nearshore tsunami propagation and run-up. In particular could be mentioned the studies of Choi et al. (2008) and Chopakatla et al. (2008). In his work Choi underlines how an anomalously large run-up height could be mainly caused by a unique geometrical shape, as in the case of the 1993 earthquake in the Japan (East) Sea that caused more than a 30m run-up height near Hamatsumae (Hokkaido Tsunami Survey Group, 1993), where there is a channel on the beach whose cross-slope shape is parabolic in form. In the works of Choi and Chopakatla tsunami has been simulated as a N wave and the wave propagation and the run-up have been studied with the commercial code Flow-3D, that is a fully 3D model that solves the Navier Stokes equation and tracks free surfaces with a Volume of Fluid method (VOF). It must be underlined that this model is not vertically integrated as the NLSWE, furnishing a more realistic representation of the reality, considering also fluid-structure interaction.

2.1.1 Landslides generated tsunami. Literature review

Either subaerial or submerged landslide generate tsunamis if they occur at the boundary of a water body (e.g. Miller 1960, Synolakis et al. 2002, Panizzo et al. 2005, Fritz et al. 2009). When a solid or granular landslide interacts with water, a transient free surface perturbation will be generated and the waves both radiate offshore and propagate alongshore. Nowadays many physical, numerical and analytical studies, have been carried out trying to go inside these complex phenomena that concern fluid-structure interaction, wave generation and propagation. Landslide generated tsunamis require a different characterization than earthquake tsunamis, due to the fact that the length scale of a landslide, and the resulting tsunami, is typically much less than that of an earthquake. The physical implication of this fact is that landslide tsunamis are not necessarily best characterized as long waves, in fact, if typical wavelength of earthquake tsunami ranges from 20 to 100 km, wavelength of landslide tsunami could reach generally 10 km.

The first experiments aimed at analyzing the physical phenomena occurring in the tsunami generation area and in the near and far-field were carried out by Russell (1838; 1845) with a falling box that generates free surface transient perturbations in a channel. This impulse waves generation method was used by many authors, for instance by Monaghan and Kos (2000), who used a Smooth Particle Hydrodynamics (SPH) method to study shallow water wave generation, due to the impact of a falling rigid block (2D).

Fritz carried out 2D physical experiments on granular subaerial landslide generated impulse waves (Fritz et al. 2004) based on the generalized Froude similarity. He identified the slide Froude number as the dominant parameter for the maximum wave envelope of crest and trough amplitudes and for the period and wavelength of the leading wave. Some experiments were conducted with deformable underwater landslide (Fleming et al., 2005; Ataie-Ashtiani and Nik-Khah, 2008b). It was observed that both sand bags and granular underwater landslide induce lower waves if compared with solid blocks ones (Ataie-Ashtiani and Nik-Khah, 2008b)and that landslide shape does not affect significantly the induced wave height (Ataie-Ashtiani and Nik-Khah, 2008a).

Models based on a direct solution of Navier-Stokes (NS) equations, and featuring a free surface tracking algorithm, have also been used. In Heinrich 1992 and Assier Rzadkiewicz et al. 1997 two-dimensional (2D) NS simulations were performed, with a Volume Of Fluids (VOF) type free surface tracking, of both underwater and subaerial landslide tsunamis. Gisler et al. in their work of 2006 proposed a modeling of the La Palma case study based on a compressible NS model.

Abadie and Grilli (2008) performed a study on landslide generated waves using a 2D numerical model, Aquilon (developed in the Trefle laboratory, UMR 8508), based on Navier-Stokes (NS) equations, with a VOF algorithm to track the interfaces. In this work, although a 2Dmodel was used, it was shown the very good accuracy of the coupling NS and VOF.

Most of these studies focused on the waves propagating towards the open sea,using a 2D approach, with the main goal of defining the properties of these waves as a function of the parameters that may be used to describe the landslide and focusing on wave generation. In the studies that have analyzed the phenomenon using a 3D approach, it has been observed that when the landslides occur at a sloping coast two systems of waves are generated: the waves radiating toward offshore and the waves that are trapped along the shore due to the refraction, called edge waves (Ursell,1952; Lynett and Liu, 2005; Johnson, 2007). The waves trapped, and thus propagating, along the coast are of special practical interest since they are responsible of the inundation of the coastal regions close to the generation area. Ursell (1952) showed that waves on straight coast can remain trapped close to the shoreline depending on the beach slope, α, (edge wave modes). In particular, he showed that the number of possible edge waves modes n_M has to satisfy the following relationship:

$$n_M \leq \frac{1}{2}\left(\frac{\pi}{2\alpha} - 1\right) \tag{2.1}$$

The paper of Liu et al. of 2005 presents a large set of numerical experiments designed to examine the maximum run-up generated by three-dimensional submerged and subaerial, solid body landslides and a depth-integrated numerical model that allows to efficiently simulate landslides in shallow and intermediate water. In that paper an identification of the parameters that most influence maximum run-up is performed. Most notably, a very clear division between the near and far field is observed. The far field is defined as the region displaced from the projection of the landslide, on the nearby beach, where edge waves may dominate the wave pattern. For submerged slides a nondimensional estimation of the maximum run-up just landward of the slide is found as well as the location and magnitude of the secondary run-up peak. This secondary peak is due to the propagation of edge waves and is in some cases larger than the peak immediately landward of the slide.

Sammarco and Renzi (2008) developed an analytical two-horizontal dimension model to analyze the different physical features of landslide-induced tsunamis along a straight coast. Their model is based on the forced linear long-wave equation of motion (LSWE). In particular they noted that after a short transient immediately following the landslide generation, the wave motion starts to be trapped at the shoreline and finally only transient long-shore traveling edge waves are present. Longer waves travel faster and are followed by a tail of shorter waves, while new crests are created. Unlike transient waves generated and propagating in water of constant depth, for landslide-induced tsunamis along a sloping beach the larger waves are not in the front of the wave train, but are shifted toward the middle of it. Experimental comparison shows the validity of the model in reproducing the physical behavior of the system. It has to be noted that the same authors demonstrated analytically that perfect trapping is not possible in a polar-symmetric topography for ideal conical island (Renzi and Sammarco, 2010).

It could be also underlined that recent numerical works have shown that for typical submarine landslide setups, frequency dispersion can play an important role in determining both the offshore wave field and the shoreline movement (e.g., Lynett and Liu, 2002) and that when sub-aerial landslide tsunami propagate over a deep sea/ocean, they evolve into a train of waves, due to the frequency dispersion effects (Bellotti et al. 2008).

These considerations underline some crucial points that must be considered when studying landslide generated tsunami, as the importance of a 3D approach, a good modeling of fluid/structure interaction, in the phase of wave generation, and frequencies dispersion, in the phase of wave propagation.

Among the recent works it can be also cited the one of Enet and Grilli (2007). They performed large three dimensional laboratory experiments to study tsunamis generated by rigid underwater landslides, with the main purpose of both gain insight into landslide tsunami generation processes and provide data for subsequent validation of a three dimensional numerical model. The experiments were carried out in a wave tank of the Ocean Engineering Department at the University of Rhode Island, USA. In their model the landslide is reproduced with a smooth and streamlined rigid body which slides down a plane slope, starting from different underwater positions. They have carried out a detailed study of the law of landslide motion and relative discussions about the generated waves features. They have confirmed the importance of initial acceleration and terminal velocity of the rigid body. Watts and Grilli carried out research studies on tsunami generated by landslides (Watts et al., 2003; Grilli and Watts, 2005). They build up GEOWAVE which is a comprehensive tsunami simulation model formed by combining the Tsunami Open and Progressive Initial Conditions System (TOPICS), for the wave maker and tsunami generation, with the FUNWAVE model for the tsunami propagation and inundation. TOPICS uses curve fits of numerical results from a fully nonlinear potential flow model to provide approximate landslide tsunami sources for tsunami propagation models, based on marine geology data and interpretations. While the simulation of tsunami propagation and inundation is carried out with the long wave propagation model FUNWAVE, which is based on fully nonlinear Boussinesq equations, with an extended dispersion equation, in the sense that it matches the linear dispersion relationship for deep water waves. They included a breaker model in FUNWAVE in order to simulate inundation of dry land. In their work, Grilli and Watts (2005) performed numerical and experimental models of tsunami generated by landslide slumps and slides.

With regard to the landslide generated tsunami, the works of Di Risio et al. (2009a; 2009b) need to be mentioned. The paper of Di Risio et al. (2009a) describes three dimensional laboratory experiments carried out at the Environmental and Maritime Hydraulic Laboratory (LIAM) of the University of L'Aquila, Italy, and reproduce a rigid landslide body sliding on a plane slope. The paper of Di Risio et al. (2009b) describes other three dimensional experiments which simulate an equal landslide body sliding down the flank of a conical island, built in the middle of a large wave tank. This is similar to the work of Briggs at al. 1995. The physical model is built at the Research and Experimentation Laboratory for Coastal Defence (LIC), of the Technical University of Bari, Italy. These last experiments will be further better explained because used for the validation of the numerical model used in this work.

2.2 The numerical model

As observed in the previous paragraph, when a solid or granular landslide interacts with water, a transient free surface perturbation is generated and the waves both radiate offshore and propagate alongshore. In order to study wave propagation and especially wave run-up, among the many different types of models, the fully three-dimensional ones are expected to give very accurate results, and therefore they appear to be highly attractive (Weiss et al. 2009, Liu et al. 2005). However these models have high computational costs that may strongly limit their application in real life. Furthermore one key point to be addressed is how much they are accurate and what is the trade off between these models and codes based on simplified approaches. In this thesis the fully three dimensional Computational Fluid Dynamics commercial code FLOW-3D (Flow Science, Inc., Sante Fe, N.M.) will be applied to simulate waves generated by subaerial and submerged landslides and the results will be compared against available experimental data, in order to validate the model and to evaluate the balance between accuracy and computational costs. Two different experiments, described in Di Risio et al. (2005) and Di Risio et al. (2009a), have been used to validate the model. In the former some simple physical experiments, reproducing the Scott Russell's wave generator, are carried out in a small two-dimensional wave flume, while in the last tests reproducing waves generated by landslides along the flank of a conical island are described.

Researches based on the commercial CFD code FLOW-3D have already been presented in the field of Coastal Engineering (Choi et al. 2007, Choi et al. 2008, Chopakatla et al. 2008). The model solves the Reynolds Averaged Navier-Stokes Equations and the continuity equation for incompressible flow along with the true volume of fluid method (VOF, Hirt and Nichols 1981) in order to compute the free surface motion. Different algorithms to solve the equations are implemented in FLOW-3D. The GMRES (generalized minimum residual) method has been selected for this work. It consists of computing, at each time step, the pressure variation used to update the velocity field. At each computational time-step the fraction of fluid of each cell (F) is estimated using a transport equation solved by using velocity field and content of fluid in each cell at the previous time step. Then the new values of F are used to update the fluid free surface with a VOF method.

The program uses a fractional area/volume obstacle representation (FAVOR) technique when objects with a complex geometry are to be represented into the computational domain. The model is able to consider the interaction between moving objects and the fluid, a crucial aspect when modeling landslide generated waves. This is pursued by using the general moving object module (GMO) of the code. It can simulate rigid bodies motion either user-prescribed (prescribed motion) or dynamically coupled with fluid flow (coupled motion). When the prescribed motion approach is used, the user specifies the time history of the object(s) movements and the fluid flow is affected by the object motion. When the coupled motion approach is adopted the object(s) and the fluid are coupled dynamically. In both cases, a moving object has six degrees of freedom and can rotate around a fixed point or a fixed axis. At each computational time step, the hydrodynamic forces and torques due to pressure and shear stress on the objects are computed. Source terms are added in the continuity equation and the VOF transport equation in order to describe the hydrodynamic effects of moving objects. In particular, the shear velocity at the moving object boundaries is accounted for into shear stress terms in the momentum equations (Flow Science 2007).

Grid resolution and (initial) time-step strongly affect numerical results. FLOW-3D allows to divide the domain into several grids of different resolution (multi-block meshes) or to use nested grids. Moreover, the time step size is variable and adjusted by respecting the Courant limit. The minimum time step depends on its initial value and can be selected by the user.

2.2.1 The basic equations

The resulting general momentum equations in the three coordinate directions considering fluid motion, GMO motion, the viscosity of the fluid and porous media are:

$$\begin{cases} \frac{\partial \mathrm{u}}{\partial \mathrm{t}} + \frac{1}{V_F}\left\{uA_x\frac{\partial u}{\partial x} + vA_y\frac{\partial u}{\partial y} + wA_z\frac{\partial u}{\partial z}\right\} - \xi\frac{A_y v^2}{xV_F} = -\frac{1}{\rho}\frac{\partial p}{\partial x} + G_x + \\ +f_x - b_x - \frac{R_{SOR}}{\rho V_F}(u - u_w - \delta u_s) \\ \\ \frac{\partial \mathrm{v}}{\partial \mathrm{t}} + \frac{1}{V_F}\left\{uA_x\frac{\partial v}{\partial x} + vA_y\frac{\partial v}{\partial y} + wA_z\frac{\partial v}{\partial z}\right\} - \xi\frac{A_y uv}{xV_F} = -\frac{1}{\rho}\left(R\frac{\partial p}{\partial x}\right) + G_y + \\ +f_y - b_y - \frac{R_{SOR}}{\rho V_F}(v - v_w - \delta v_s) \\ \\ \frac{\partial \mathrm{w}}{\partial \mathrm{t}} + \frac{1}{V_F}\left\{uA_x\frac{\partial w}{\partial x} + vA_y\frac{\partial w}{\partial y} + wA_z\frac{\partial w}{\partial z}\right\} - = -\frac{1}{\rho}\frac{\partial p}{\partial z} + G_z + \\ +f_z - b_z - \frac{R_{SOR}}{\rho V_F}(w - w_w - \delta w_s) \end{cases} \tag{2.2}$$

Before illustrating the terms that constitute these equations, it must be underlined that them could be used both with cartesian (x,y,z) and cylindrical (r,θ, z) coordinates. When using cylindrical coordinates in 2.2 x must be replaced with r and y with θ, the coefficient ξ must be 1, otherwise 0. The coefficient R, that is a ratio between a reference radius, r_m, and r must be 1 when cartesian coordinates are used.

In the equation 2.2 *(u, v, w)* are the fluid velocity components, V_F is the fractional volume open to flow, (G_x, G_y, G_z) are body accelerations, (f_x, f_y, f_z) are viscous accelerations, (A_x, A_y, A_z) are respectively the fractional area open to flow in the x, y and z direction and (b_x, b_y, b_z) are flow losses in porous media. The final terms account for the injection of mass at a source represented by a geometry component, in fact (u_w, v_w, w_w) represent the velocity of the source component which will generally be non-zero for a mass source at a General Moving Object (GMO). The term (u_s, v_s, w_s) is the velocity of the fluid at the surface of the source relative to the source itself.
The Mass Continuity Equation is expressed as follows:

$$V_F\frac{\partial \rho}{\partial t} + \frac{\partial}{\partial x}(\rho u A_x) + R\frac{\partial}{\partial y}(\rho v A_y) + \frac{\partial}{\partial z}(\rho w A_z) + \xi\frac{\rho u A_x}{x} = R_{DIF} + R_{SOR} \tag{2.3}$$

where, beyond the terms already presented for the preview equation, R_{DIF} is a turbulent diffusion term, R_{SOR} is a mass source and A_x, A_y, A_z are respectively the fractional area open to flow in the x, y and z-directions. The mass source term, when the FAVOR (Fractional Area-Volume Obstacle Representation) is used,accounts also for the additional volume source generated on the boundary of a moving object.

Fluid configurations are defined in terms of a volume of fluid (VOF) function,*F(x,y,z,t)* that represent the volume of fluid per unite volume and satisfies the equation:

$$\left[\frac{\partial}{\partial x}(FA_x u) + R\frac{\partial}{\partial y}(FA_y v) + \frac{\partial}{\partial z}(FA_z w) + \xi\frac{FA_x u}{x}\right] = F_{DIF} + F_{SOR} \tag{2.4}$$

where F_{DIF} is a diffusion term different for two fluid mixing and the term F_{SOR} is the time rate of change of the volume fraction of fluid associated with the mass source.

2.3 2D numerical investigation: the Scott-Russel wave generator

2.3.1 The experiments

A series of experiments for water wave generation by a solid body plunger (Scott Russell Wave Generator) has been carried out at LIAM laboratory, L'Aquila University, Italy (Di Risio, 2005). The experiments were performed in a three-dimensional flume 12 m long, 0.45 m deep and 0.3 m wide (figura:2.1,a). A rectangular box with width = 0.3 m (same as the flume), height = 0.1 m (vertical direction) and variable length (in the flume direction) is released vertically at one end of the flume to generate waves. The space between the box and the vertical walls of the flume is less than 1 mm. The specific weight of the box is 1.33 t/m^3. Three lengths of the rectangular rigid body (0.05 m, 0.1 m and 0.15 m) are used. Twenty one tests have been carried out. Three different initial elevations of the box are tested: partially submerged (the bottom of the box is 3 cm below the still water level); at the still water level and aerial (3 cm above the still water level). The water depth in the flume is also varied: 6 cm, 10 cm, 18 cm, and 23 cm. In order to measure the free surface elevation of the fluid five gauges have been placed. A video camera (Canon XM1) has framed the impact area with a frame acquisition rate of 25Hz. The free surface elevation data and the displacement of the rigid body have been used in the past for a comparative study (Yim et al. 2008) between two different kinds of 2D numerical simulation. The first one was a VOF (volume of fluid) algorithm, and the second a SPH (Smoothed Particle Hydrodynamics) algorithm. For their simulations the authors have chosen three representative cases (L10H10M3, L10H10P3, and L10H18P3) among the 21 tests, and for all of them the simulation results have shown a good agreement with the experiments. Here the same three cases have been analyzed:

- L10H10M3: length of the body 10 cm, water depth 10 cm and body elevation 3 cm under the still water level.

- L10H10P3: length of the body 10 cm, water depth 10 cm and body elevation 3 cm over the still water level.

- L10H18P3: length of the body 10 cm, water depth 18 cm and body elevation 3 cm over the still water level.

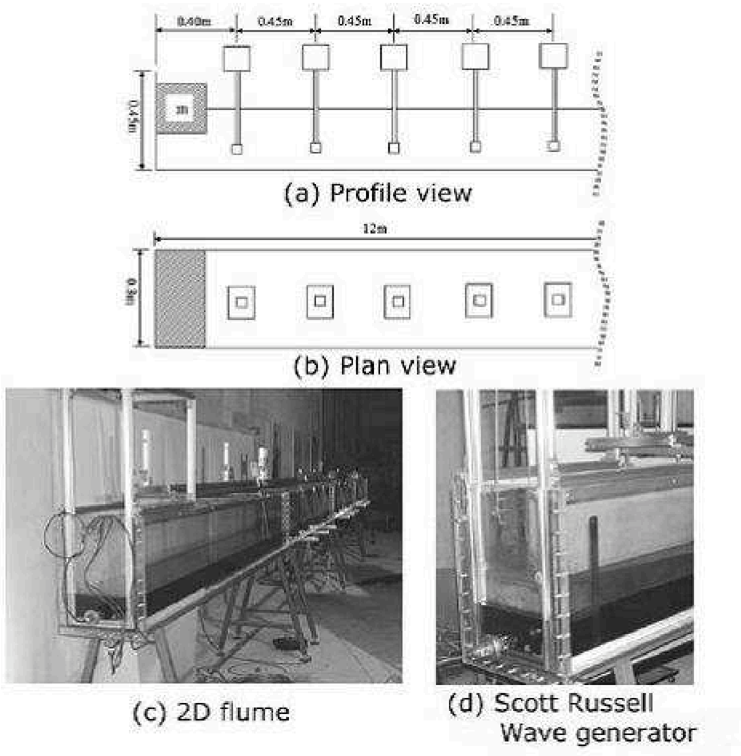

Figure 2.1: a) and b) locations of wave gauges, c) picture of the 2D flume, d) Scott Russell wave generator.

2.3.2 The application of the numerical model

Different tests have been carried out to compare experimental and simulated results, but the best fitting of the experimental data, using FLOW-3D, has been achieved with the same grid size and turbulence parameters used by Yim in his work. The simulation has been conducted using a 2D domain of 2mX0.4m in the x and z direction respectively,covering a time period of 3 s. The grid of the computational domain is formed by 400 cells in the x direction and 160 cells in the z direction, and so x=0.5 cm and z=0.25 cm.

Free slip conditions have been applied on the sides of the falling body and on all the boundary of the computational domain except at the right side end, where there is an outflow condition. The fluid has been considered viscous and the turbulence model chosen is the k-ε in the formulation of Rodi (1980), as in the work of Yim. The movement of the rigid body has

Figure 2.2: Comparison between the numerical and the physical domain.

been imposed as that obtained during the experiments. The solver of the hydrodynamic equations used is GMRES. The computational time is about 1 hour on a PC Intel (R) Core (TM) 2 Duo CPU with a frequency of 2.66 GHz equipped with a 8 GB Ram.

2.3.3 Validation of the numerical model

Here for the three analyzed cases the free surface elevation at the first two gauges, located respectively at 0.4 and 0.85 m from the left flume boundary and some snapshots of the simulation are presented.

Figures 2.3, 2.4 and 2.5 show the comparison of some snapshots of the generation phase in the three examined cases at several instants; the simulation is represented on the left while the experiment on right. It can be noticed a very good synchronism during the impact phase and a very good reproduction of the generated and propagating waves by the numerical model. Only in the case of the L10H18P3 an instantaneous splash is generated, and in this case the numerical model has been able to reproduce the general behaviour and the following propagation phase but not the details of the flow field. The reason of that maybe could be found in the resolution of the mesh, that does not allow to represent so instantaneous phenomena.

Comparing the numerical results (continuous line) and the measures (dots line) at the 0.4 m and 0.85 m gauges, a general good agreement has been observed and this is shown in figure 2.6, 2.7 and 2.8, where the numerical results are plotted against experimental data. Both the physical and numerical results in the first case (L10H10M3), in figure 2.6, show that the generated wave is a solitary-like wave with small trailing waves. A slight phase difference could however be observed, which could be caused by the different reference times used in the experiment measurements.

In the second case (L10H10P3) because of the higher initial falling height than that of the previous case, larger waves are generated near the plunging box. The leading wave attenuates significantly between the two wave gauges

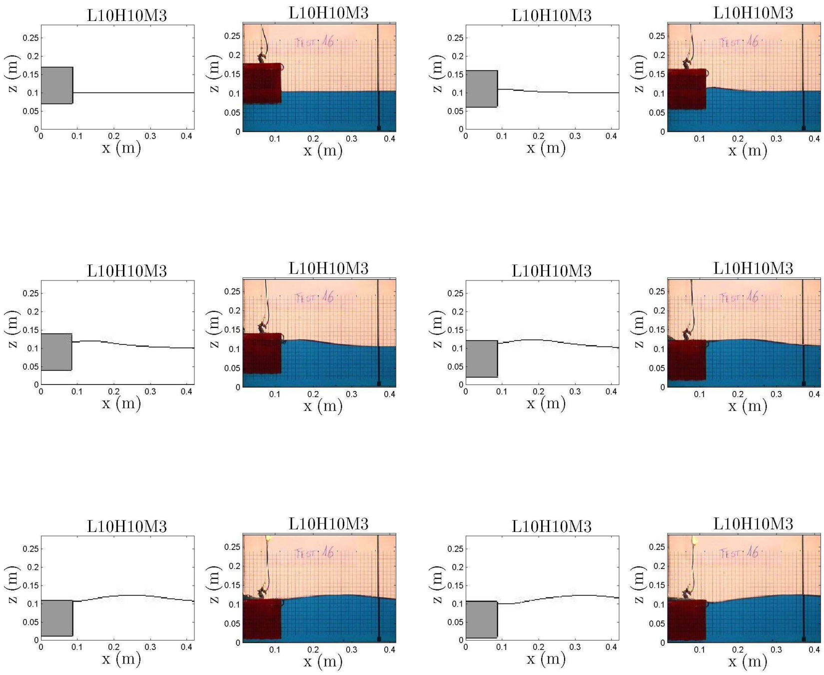

Figure 2.3: Snapshots of the simulation (left) and of the experiment (right) at t=0.2,0.4,0.6,0.8,1.0,1.2 s.The first two panels of the first row represent t=0.2 s while the other two of the same row represent t=0.4 s

and its length increases because of the amplitude dispersion.

It can also be observed that there is a larger fluid motion than in the previous case with an initially submerged position. In the third case (L10H18P3), since the water depth is larger than the height of the falling box, as the box moves further downwards, it is overtopped by a wave propagating towards the left end of the flume, which is then reflected back into the flume (figure 2.5). In this case, as shown in figure 2.8, it is not possible to observe just a solitary wave, but a train of dispersive waves. The amplitude and phase of the leading wave is predicted accurately by the model. The influence of the ratio between the body width (L) and the water depth (h), L/h has been previously studied, and in the work of Panizzo et al. (2001) it was underlined that when the dimensions of the falling body

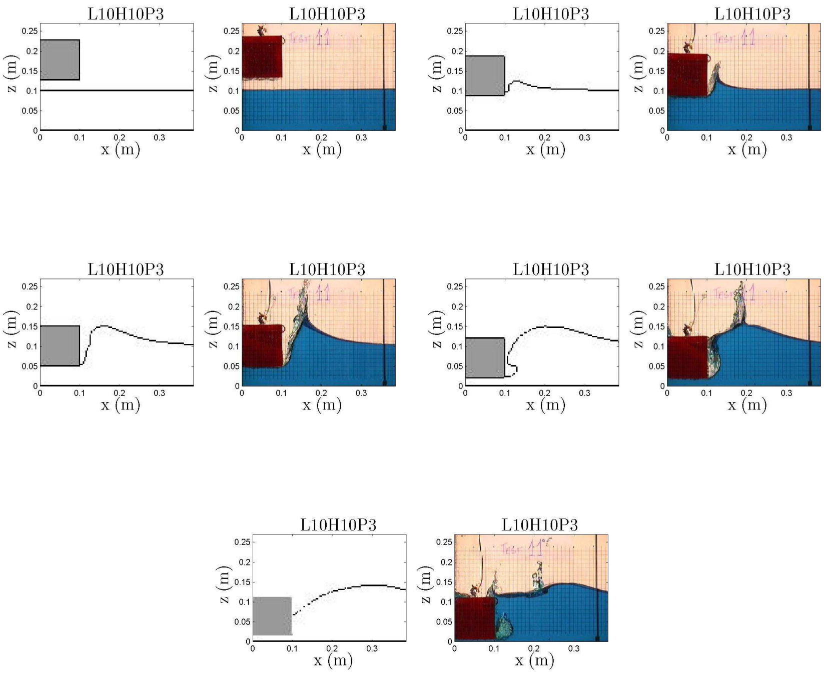

Figure 2.4: Snapshots of the simulation (left) and of the experiment (right) at t=0.2,0.4,0.6,0.8,1.0 s.The first two panels of the first row represent t=0.2 s while the other two of the same row represent t=0.4 s

are large in comparison to water depth, solitary waves are to be expected while a train of dispersive waves is likely to be generated in relatively deep water.

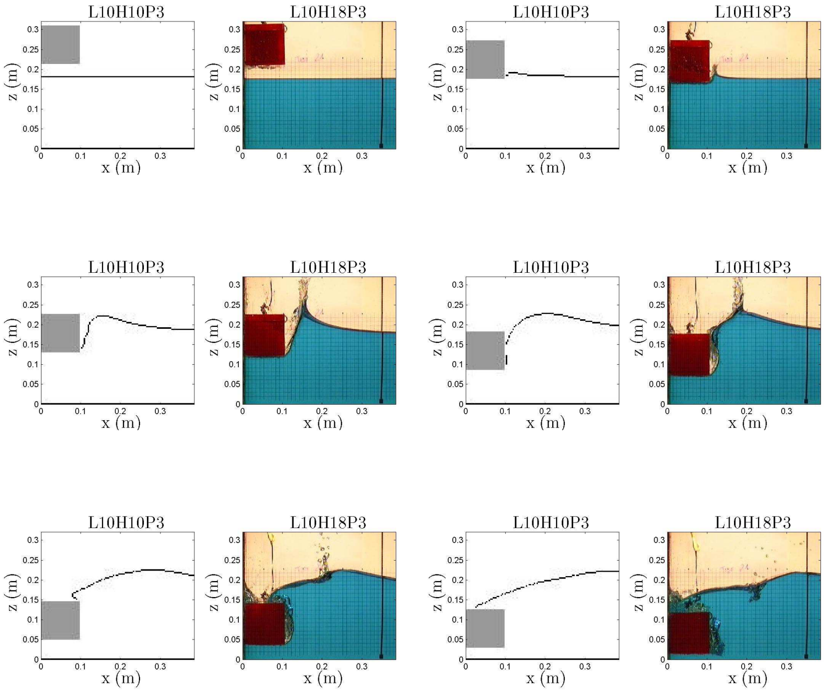

Figure 2.5: Snapshots of the simulation (left) and of the experiment (right) at t=0.2,0.4,0.6,0.8,1.0,1.2 s.The first two panels of the first row represent t=0.2 s while the other two of the same row represent t=0.4 s

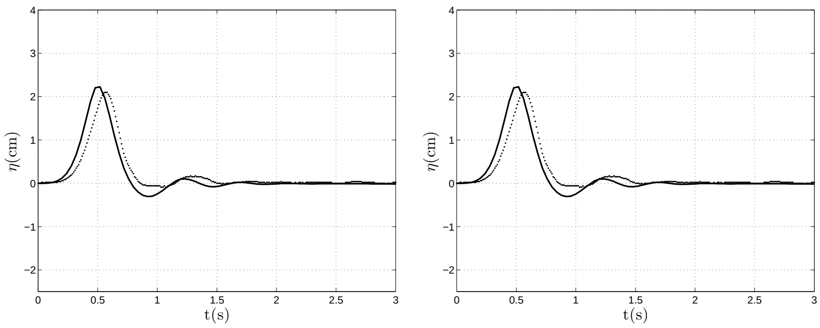

Figure 2.6: The evolution of the free surface elevation at the first (on the left) and at the second gauges (on the right) for test L10H10M3.

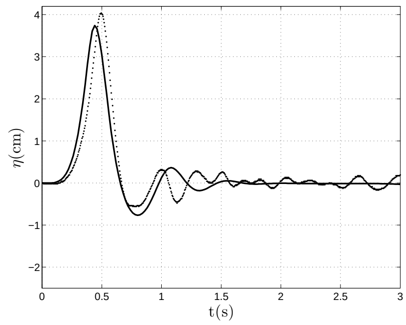

Figure 2.7: The evolution of the free surface elevation at the first (on the left) and at the second gauges (on the right) for test L10H10P3.

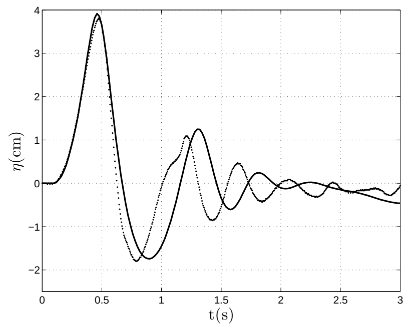

Figure 2.8: The evolution of the free surface elevation at the first (on the left) and at the second (on the right) gauges for test L10H18P3.

Figure 2.9: Picture of the conical island placed at the center of the wave tank.

2.4 3D numerical investigation: landslide generated waves around a conical island

2.4.1 The physical model and the experiments

The experiments have been carried out in a large wave tank (Figure 2.9) at the Research and Experimentation Laboratory for Coastal Defence (LIC) of the Technical University of Bari (Italy) in cooperation with the Environmental And Maritime Hydraulics Laboratory "Umberto Messina" (LIAM) of the University of L'Aquila (Italy). In the following, a brief description of the physical model and of the experiments carried out is outlined. More detailed information can be find in the paper of Di Risio et al. (2009a). The wave tank is 30.00 m wide, 50.00 m long and 3.00 m deep (Figure 2.10); at the wave tank center a conical island is placed. It is built using PVC sheets (thickness 0.01 m) and sustained by a steel frame. The island has a radius of 4.45 m at the tank bottom level and the slope of its flanks is 1/3 (1 vertical, 3 horizontal).

The landslide model has a regular shape that reproduces a half of an ellipsoid. The thickness of the ellipsoid is 0.05 m, its maximum width

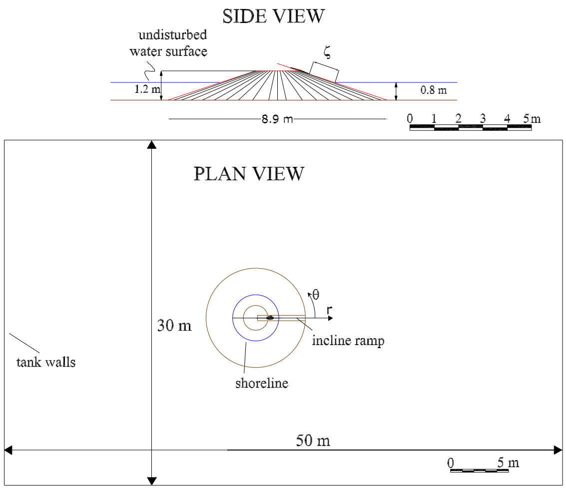

Figure 2.10: Experimental layout.

(parallel to the undisturbed shoreline) is 0.40 m and its maximum length (orthogonal to the undisturbed shoreline) is 0.80 m, for a total volume V=0.0084 m^3. The density of the landslide is 1.83·10^3 kg/m^3 for a total mass of 15.40 kg. The landslide moves down the flank of the island and it is constrained to slide on rails placed along the slope; it therefore moves exactly along a specified line under the gravity action. The radius of the circular shoreline is 2.05 m and the water depth in the tank is 0.8 m.

Several tests have been performed by varying the height from which the landslide falls into the water. The release distance (ζ in Figure 2.10) was set to 0.60 m, 0.50 m, 0.40 m and 0.30 m: only subaerial landslides have been studied. The displacement and the velocity of the landslide have been reconstructed on the basis of the measured acceleration, then the velocity and the position of the landslide is available for each test (Di Risio et al. 2009a, Di Risio et al. 2009b).

The instantaneous displacements of the shoreline have been measured by means of special wave gauges that consist of two steel bars (square section of 4 mm $\times$ 4 mm) directly embedded into the PVC of the slope. The free surface elevation has been measured by means of traditional resistive gauges. All the signals have been acquired simultaneously at a frequency of 1000 Hz. A total of 20 run-up gauges and 21 surface level gauges have been used during each experimental test. The frame of reference used to represent and analyze the experiments (Figure 2.10) is a cylindrical coordinate system (r, θ, z). The origin of the reference frame is located at the center of the conical island.

2.4.2 The application of the numerical model

FLOW-3D has been used to reproduce the experiments of Di Risio et al. (2009a). Experiments with falling height ζ equal to 0.3 m, 0.4 m, 0.5 m and 0.6 m are considered in order to validate the numerical model. Further simulations have been run to perform parametric analysis, varying the release height of the landslide, the shape of the landslide and the radius of the island. Cylindrical coordinates have been used in the numerical model in view of the specific configuration. Furthermore, in order to reduce the computational costs, only half of the domain is reproduced due to the symmetry of the problem with respect to the line along which the landslide falls.

Two meshes with different resolution have been used for solving the equations. The finest mesh is defined for $r \in [1.8, 6]$ m and $\theta \in [0°, 180°]$; it covers the impact area of the landslide with the free surface and enables a detailed reproduction of the shoreline displacements and of the waves propagation offshore. The spatial resolution is 1.5 cm in the radial and z directions, while the angular resolution is 0.416°. At the shoreline ($r = r_0$) the curvilinear abscissa ($s = r_0\theta$) has a resolution of 1.5 cm. Table 2.1 summarizes the different resolutions of the two meshes containing the fluid. It must be noted that, because of the cylindrical coordinates, the curvilinear abscissa ($s(r) = r\theta$) resolution decreases as r increases. The resolution of the finest mesh, shown in table 2.1, has been selected in order to have cells as square as possible at the shoreline (in the r, θ plane).

A critical part of the domain is the interface between the two meshes. By using meshes of too different resolutions, spurious reflections at the interface can occur. Then, the coarse mesh cells dimension in the angular direction at the interface should be less than twice the one of the finest mesh (Flow Science 2007).

In the simulations presented herein, the landslide has been reproduced as a prescribed motion object using the law of Di Risio et al. (2009b).

Different techniques are employed by FLOW-3D in order to model turbulence stresses: LES (Rodi 1980), k-ϵ model (Rodi 1980) and RNG (Renormalization Group; Yakhot and Orszag 1986). In the following simulations the RNG model has been used because of its wider applicability than the standard k-ϵ model and for its accuracy in low intensity turbulence

Table 2.1: Resolution of the fine mesh at its beginning, at the shoreline, at the island foot and at the end of the mesh. Resolution of the coarse mesh at its beginning and at its end.

Fine fluid mesh			
Radius (m)	Δs (m)	Δr(m)	Δz (m)
2.05	0.015	0.015	0.015
4.45	0.032	0.015	0.015
6.00	0.045	0.015	0.015
Coarse fluid mesh			
6.00	0.078	0.05	0.04
12.00	0.156	0.05	0.04

flows (Yakhot and Orszag 1986, Choi et al. 2007). Roughness of 0.2 mm has been considered for the flanks of the island built in PVC.

The offshore circular boundary has been modeled as fully reflective; waves reflected at boundary are therefore expected to affect the results after some time, as outlined in the following section. No slip conditions have been imposed along the solid object boundaries. Each simulation reproduces 20 s in the physical model scale. The total number of computational cells is about $11 \cdot 10^6$ and the computational time is about 36 hours on a PC Intel (R) Core (TM) 2 Duo CPU with a frequency of 2.66 GHz equipped with a 8 GB Ram. It must be underlined that for these simulations all the default values of the program have been used: it means that in this work no calibration was performed.

2.4.3 Validation of the numerical model

In this section the results of the numerical model are compared with the experimental measurements. In the work described herein the experimental data collected by means of the sensors depicted in Figure 2.11 and summarized in Table 2.2, that consist of run-up and water level time series, have been used.

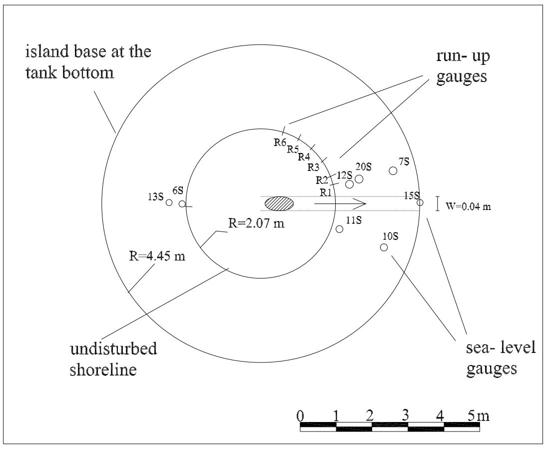

Figure 2.11: Sensors locations (see also table 2.2). The width (w) of the experimental landslide is also reported with dashed line.

It has to be stressed that, as stated in the previous section, the use of reflective boundaries has produced reflected waves that have contaminated the wave field around the island after the first two-three waves have passed. Hence, the validation of the numerical model has been carried out by focusing on the first two waves, inducing the maximum run-up in the area between 0° and 90° from the impact point, which is the area considered in this study for comparison with the experiments. The maximum run-up in the angular sector 90°-180° is induced by the third and the forth waves as pointed out by Di Risio et al. (2009a).

Overview of the numerical results

Figures 2.12 and 2.13 show some snapshots of wave pattern for $\zeta = 0.3$ m test, but similar results are achieved for other values of ζ. The first time step is in the left upper panel, the following one is in the right upper panel. The landslide falls on the left side ($x = r_0 = 2.05$ m, $\theta = 0°$) of the conical

Table 2.2: Sensors naming and location.

Runup gauges		
Sensor name	r (m)	θ (°)
1R	2.05	14.5
2R	2.05	20.6
3R	2.05	34.3
4R	2.05	47.6
5R	2.05	60.2
6R	2.05	72.9
Water level gauges		
Sensor name	r (m)	θ (°)
12S	2.49	11.8
20S	2.80	13.5
7S	3.76	13.7
11S	2.27	19.5
10S	3.64	20.5
15S	4.44	0.1
6S	2.27	178.7
13S	2.65	179.2

island and it firstly generates a crest, and then a trough. It is possible to observe that waves propagate both off-shore and alongshore.

A plan view of the propagation pattern is shown in Figure 2.14. The highest waves propagate along the direction of the landslide and the effects of refraction (different wave celerity) induce the rotation of the wave fronts near the shore. Moreover the distance between the wave fronts highlights that the waves propagate faster radiating offshore than close to the shore because of the water deepening.

Additionally, in the left upper panel of Figure 2.14 it is possible to notice that a first small crest followed by a large trough is generated. The second wave is very steep (see right upper panel of the same Figure).

Comparison of numerical and experimental time series

Figure 2.15 shows the comparison of numerical results against the time series collected by means of run-up gauges for $\zeta = 0.5$ m test. Each panel

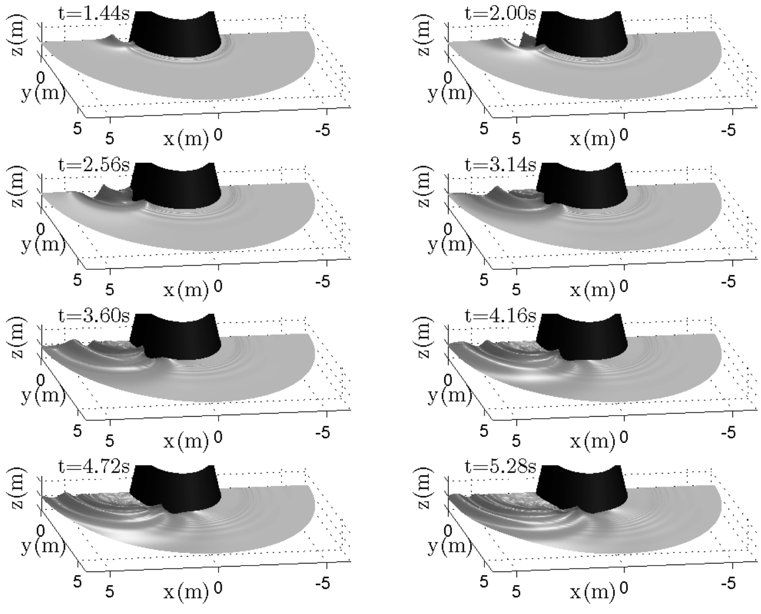

Figure 2.12: Snapshots of computed water surface at different times for ζ=0.3 m. Increasing time left to right (from 1.44 s to 5.28 s).

refers to a single run-up gauge up to about $\theta = 90°$ from the generation area. Continuous lines represent numerical results, dashed lines represent experimental data. An important aspect that has to be underlined is that wave run-up is not a direct output of the model, so an algorithm has been implemented in order to evaluate the maximum run-up. This is calculated extracting from Flow 3D the free surface elevation in the required sections and then identifying the intersection between the free surface elevation in the last filled or partially filled cell and the island flank.

Looking to the generated waves it is possible to observe that the first wave is generated by a piston-like mechanism. At the first run-up gauge it presents a crest, very steep, followed by a larger trough. The second wave, at the same gauge, is steeper than the first one and its trough is very small. Away from the generation area, i.e. starting from the third run-up gauge (3R), the crest of the first wave becomes smaller if compared with the second one, and the trough of the second wave increases.

It could be noted that the numerical model well reproduces the typical

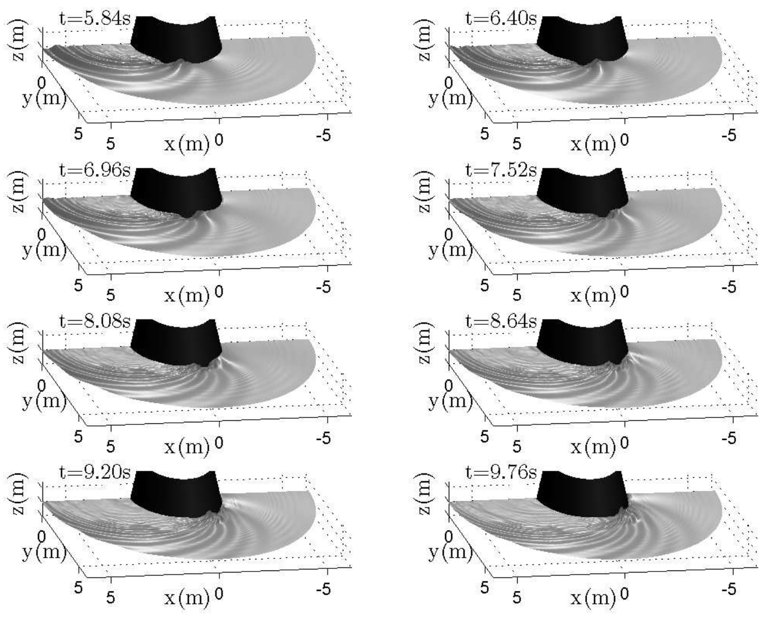

Figure 2.13: Snapshots of computed water surface at different times for ζ=0.3 m. Increasing time left to right (from 5.84 s to 9.76 s).

behavior of frequency dispersive waves, whose energy travels at the group celerity, smaller than waves celerity. Then, the maximum run-up propagates at group celerity, and it is induced by the first wave near the generation area, then by the second one and so on, as distance from impact increases (Di Risio et al. 2009a).

As far as numerical results are concerned, it is possible to point out that crest and trough amplitudes are well predicted by the model and that generated waves travel in phase, i.e. the numerical model reproduces the wave celerity in good agreement with experimental data.

Time series of Figure 2.15 show that, for all the gauges, reflected waves from offshore boundary come back to the island after about 11 s. The higher reflection of the numerical domain is due to the shape of the boundary that, being circular and not rectangular, as in the experiments, reflects back all the waves towards its center.

The comparison between numerical and physical results at the run-up gauges for the other experimented falling height, 0.3, 0.4 and 0.6 m is shown

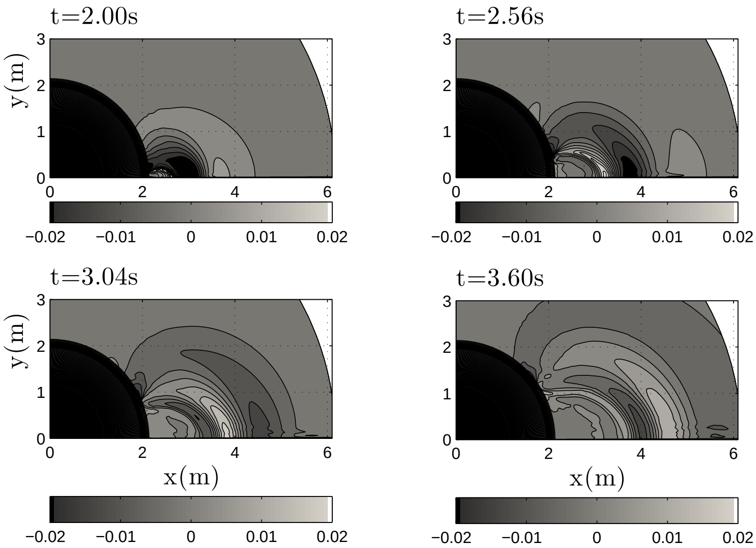

Figure 2.14: Contours of the free surface displacement for ζ=0.3 m (only numerical result for $\theta = 0° \div 90°$ are reported).

in Figure 2.16, 2.17 and 2.18 and also in these cases the goodness of the numerical results can be observed.

Figure 2.19 shows a comparison between experimental and numerical results at the offshore surface elevation wave gauges for ζ=0.5 m. Each panel refers to a single gauge: continuous lines indicate numerical results, dashed lines experimental data. Wave gauge 15S (r = 4.44 m, $\theta = 0.0°$) is placed in front of the landslide path, while two sets of other gauges (12S, 20S, 7S and 11S, 10S) are placed almost along direction $\theta = 15°$ and $\theta = -20°$. For these last gauges the numerical results have been taken considering the symmetry of the domain ($\theta = 20°$). Two other sea-level gauges (6S and 13S) are placed at the rear side of the island.

Also the waves that propagate seaward near the generation area present first a crest and then a trough; this is still due to the generation mechanism, which acts like a piston that generates a positive wave. During the wave propagation waves lengthen. The crest amplitude of the first wave decreases and the one of the trailing waves increases. The wave trains at the gauges placed at the rear side of the island (i.e. wave gauges 6S, r = 2.27 m, $\theta = 178°$, and 13S, r = 2.65 m, $\theta = 179°$) present first a small trough and then a crest. Here, the wave periods are longer if compared to the time

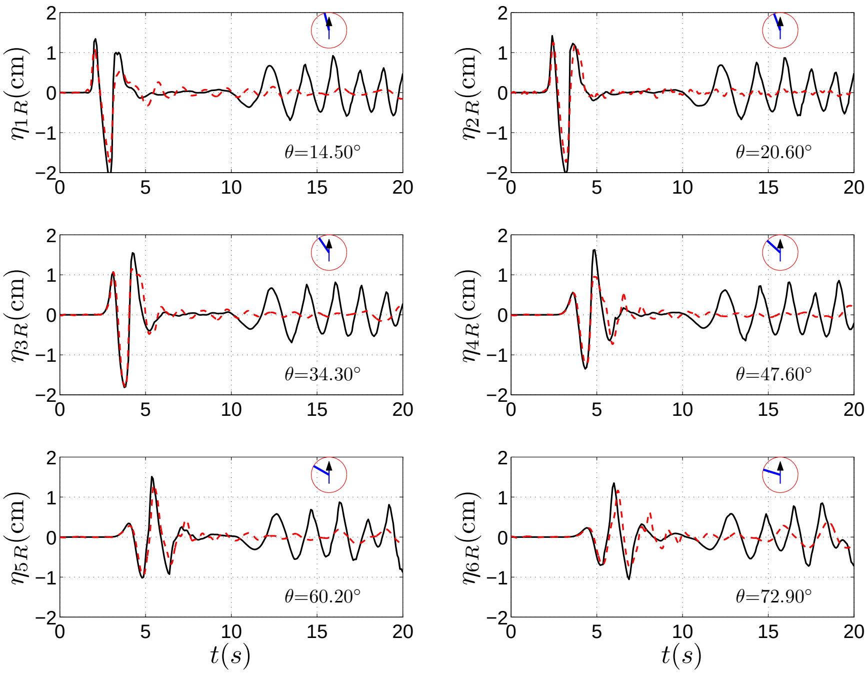

Figure 2.15: Shoreline vertical displacements at run-up gauges (see table 2.2) for ζ=0.5 m. Continuous lines represent numerical results, dashed lines refer to experimental data.

series collected in the front side of the island and the third waves are the highest.

Numerical results agree satisfactorily with experimental data and the general behavior of propagating waves is reproduced with accuracy. In particular, important features of waves propagation, i.e. arrival time of the crest, wave height and wave period are correctly estimated.

The largest crest during the experiments has been observed at the gauge 12S (first upper panel, Figure 2.19), but in this case the numerical model does not agree with experimental time series. However, it has to be stressed that this gauge is placed very close to the generation area and that the results get closer to the experimental data as the distance from the generation area increases. It has been argued that high frequency components are not reproduced depending on the mesh resolution. In the near field high and low frequency waves are superposed, and together contribute to induce the maximum crest elevation. In the far field, on the contrary, due to

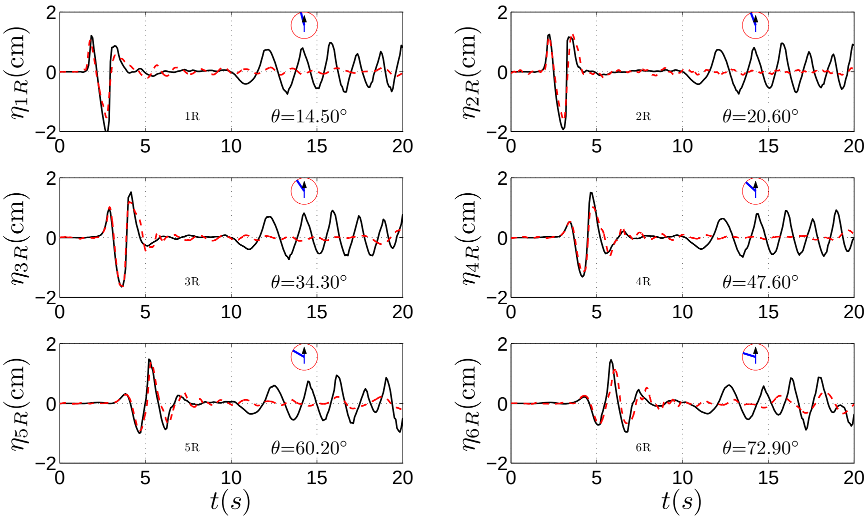

Figure 2.16: Shoreline vertical displacements at run-up gauges (see table 2.2) for ζ=0.3 m. Continuous lines represent numerical results, dashed lines refer to experimental data.

the frequency dispersion mechanism (Panizzo et al. 2001), long frequency components arrive earlier than high frequency ones and induce the largest waves.

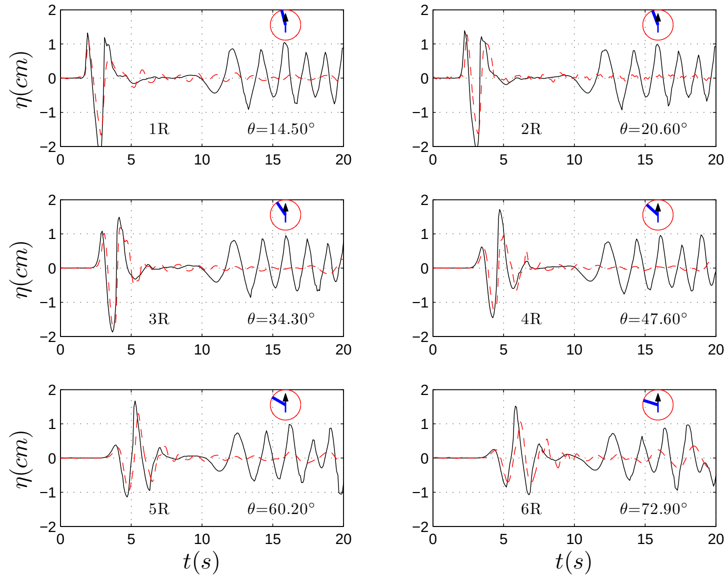

Figure 2.17: Shoreline vertical displacements at run-up gauges (see table 2.2) for ζ=0.4 m. Continuous lines represent numerical results, dashed lines refer to experimental data.

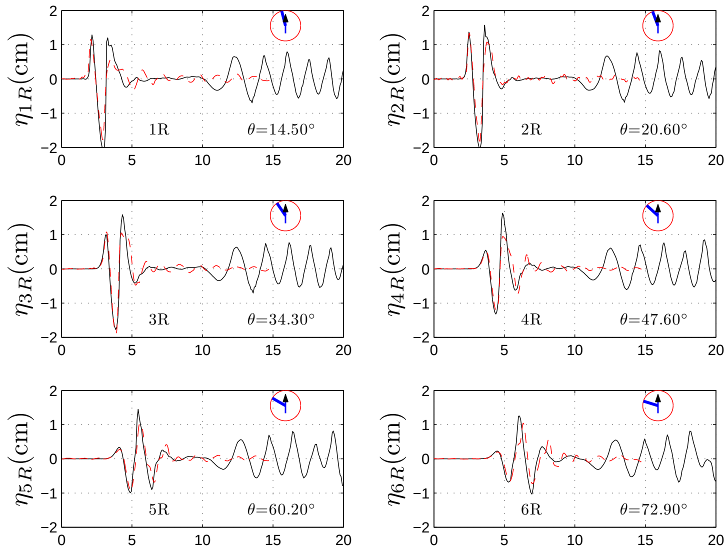

Figure 2.18: Shoreline vertical displacements at run-up gauges (see table 2.2) for ζ=0.6 m. Continuous lines represent numerical results, dashed lines refer to experimental data.

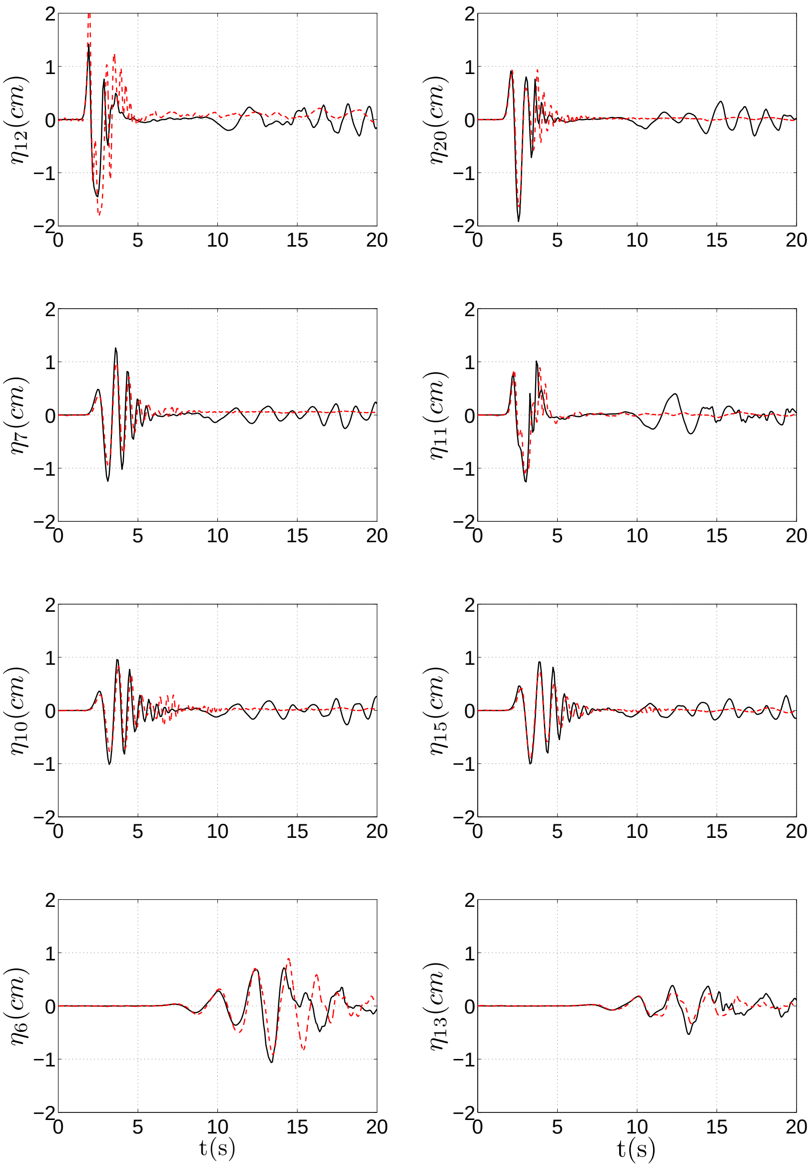

Figure 2.19: Free surface elevation time series at wave gauges for $\zeta = 0.5$ m. Dashed lines indicate experimental data and continuous lines numerical results.

The spatial distribution of run-up

A crucial aspect in run-up and run-down analysis is the evolution of these parameters around the island, i.e. their dependence from the curvilinear abscissa. For this reason, both numerical and experimental time series have been analyzed by using the zero-crossing method, in order to compare the properties of each wave.

Figure 2.20 shows run-up and run-down spatial distribution induced by the first wave (left panels) and by the second wave (right panels), for landslides falling from ζ = 0.4 m (upper panels), 0.5 m (middle panels) and 0.6 m (lower panels). Numerical results are represented as empty squares connected by a line, while experimental data as solid circles. For the experiments carried out with $\zeta = 0.3$ m, 0.5 m and 0.6 m two repetitions of each test are available from the experimental campaign. In Figure 2.20, when available, the results of both repetitions have been plotted.

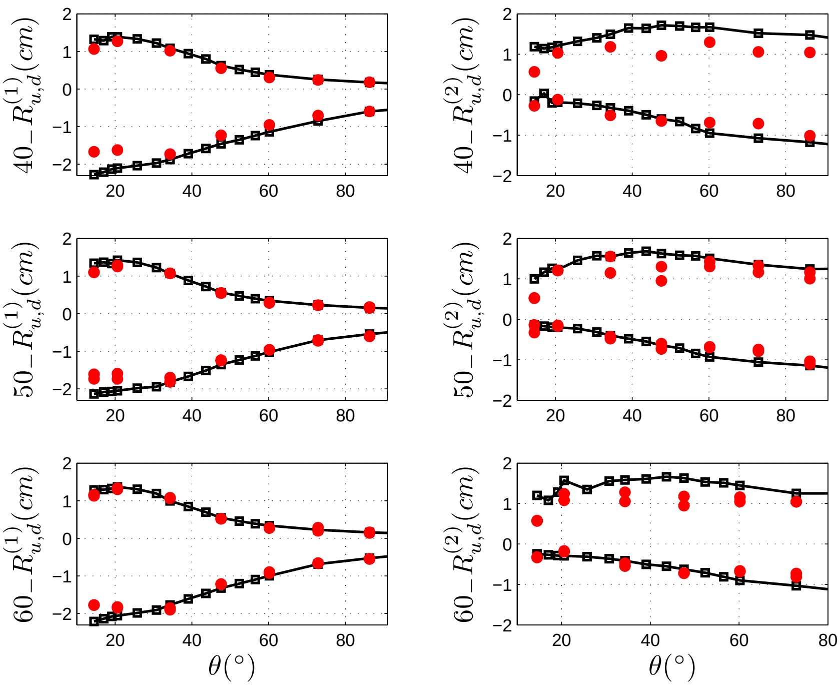

Figure 2.20: Spatial variation of run-up and run-down induced by the first wave (left panels) and by the second wave (right panels) for ζ=0.4 m, 0.5 m and 0.6 m. Solid circles refer to experimental values, squares indicate numerical results.

It has to be noticed that the results shown in the Figure allow to validate the numerical model and, at the same time, to get a higher resolution map of the run-up than the one obtained from the experiments.

FLOW-3D satisfactorily reproduces the first wave run-up and run-down trends for the three falling heights. Very good agreement between numerical and experimental run-up is observed, while wave run-down is slightly overestimated at the first two gauges. Results show that wave run-up reaches its maximum at the second gauge, at about $\theta = 20°$. Then both run-up and run-down decrease.

As far as the second wave is concerned, wave run-down is well reproduced by the numerical model; run-up is overestimated at intermediate gauges ($\theta = 30° - 60°$). It has to be underlined that for these gauges the experimental data show a significant variability between each repetition of the same test, as observed by Di Risio et al. (2009a). Moreover, spatial distributions show that both run-up and run-down absolute values increase away from the generation area but, while the former reaches its maximum between 40° and 60°, the latter continues to increase. For $\zeta = 0.5$ m (middle panels of 2.20) the numerical results seem to be more in agreement with laboratory ones than for the other experiments.

2.5 Parametric studies

2.5.1 The influence of the landslide falling height

A parametric analysis has been carried out in order to evaluate the relationship between the features of the generated waves and the falling height ζ. In particular have been analyzed both aerial and sub aerial landslide; table 2.3 enumerates the simulations carried out, underlining which are added to the ones physically modeled during the physical experiments.

Table 2.3: Physical and numerical models simulations.

Physical model	Numerical model
ζ(m)	ζ(m)
0.6	0.60
0.5	0.50
0.4	0.40
0.3	0.30
	0.15
	0.00
	-0.20
	-0.45
	-0.60
	-0.90

In particular, Figures 2.21 and 2.22 show the computed maximum run-up and run-down (empty squares) generated by the first and the second wave by aerial and submerged landslide at different wave gauges against experimental findings (solid circles). These values have been evaluated for $\zeta = 0.3$ m, 0.4 m, 0.5 m and 0.6 m, as in the experiments, and also for $\zeta = 0$ m, 0.15 m, considering aerial landslide. Some submerged landslides have also been simulated, considering $\zeta = -0.2$ m, -0.45 m, -0.60 m and -0.90 m. All available experimental repetitions of each test are reported. It is possible to observe that the release distance does not influence the maximum run-up and run-down induced by the first wave for the subaerial landslides except the values related to $\zeta = 0$ m at the gauges closest to the generation area that show a slight dependence of the run-up on ζ. Considering the partially and completely submerged landslides, run-up and run-down decrease for smaller falling heights especially at the first gauges.

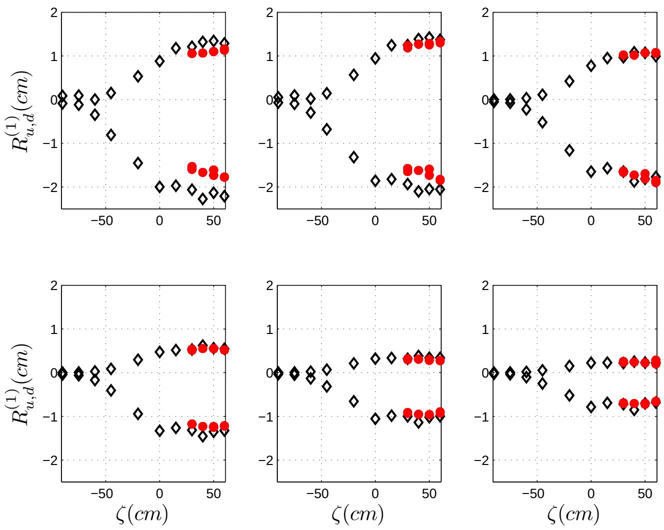

Figure 2.21: Comparison between experimental (solid circles) and numerical results (squares) at run-up wave gauges for second wave induced perturbation as a function of falling height ζ.

Looking at the run-up induced by the second wave (Figure 2.22), it can be observed that it is is overestimated by the numerical model at the first gauge (1R, $\theta = 14.5°$) for the subaerial landslides. The second wave properties do not seem to be affected by ζ for subaerial landslides but it could be noted also that relevant run-up and run-down are generated also by the partially submerged landslides. This confirms the different generation mechanism for subaerial and submerged landslides, that would be better analyzed in the next section.

The parametric analysis has been carried out also for radiating waves measured by the offshore gauges. Figures 2.23 and 2.24 show comparison for the first and the second wave respectively. Very good agreement between numerical and experimental results for the first wave is observed (Figure 2.23), except for the gauge nearest to the generation area (12S, $r = 2.49$ m, $\theta = 11.8°$). The second wave (Figure 2.24), is also well reproduced by the numerical model that still does not reproduce high frequencies at the nearest gauges.

It can be noted a stronger influence of parameter ζ for the offshore waves for subaerial landslides, since at the farthest gauges both the crest and the trough decrease with the growth of the falling height ζ. This is mostly true

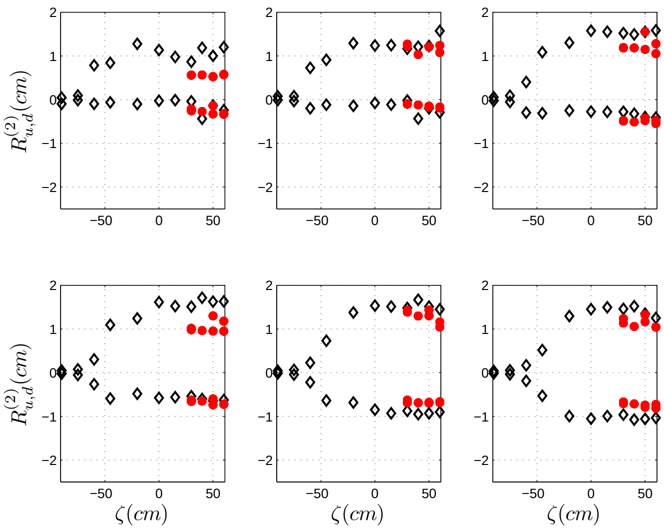

Figure 2.22: Comparison between experimental (solid circles) and numerical results (squares) at run-up wave gauges for second wave induced perturbation as a function of falling height ζ.

at the gauge 15S ($r = 4.44$ m, $\theta = 0.0°$), that is located just in front of the landslide. It can be observed that there is a completely different behaviour for submerged landslide, in fact in this case crest and the trough increase with the growth of the falling height ζ. However it has to be noticed that the numerical study presented herein focus only on the first two waves, i.e. not all the wave train radiated offshore is analyzed.

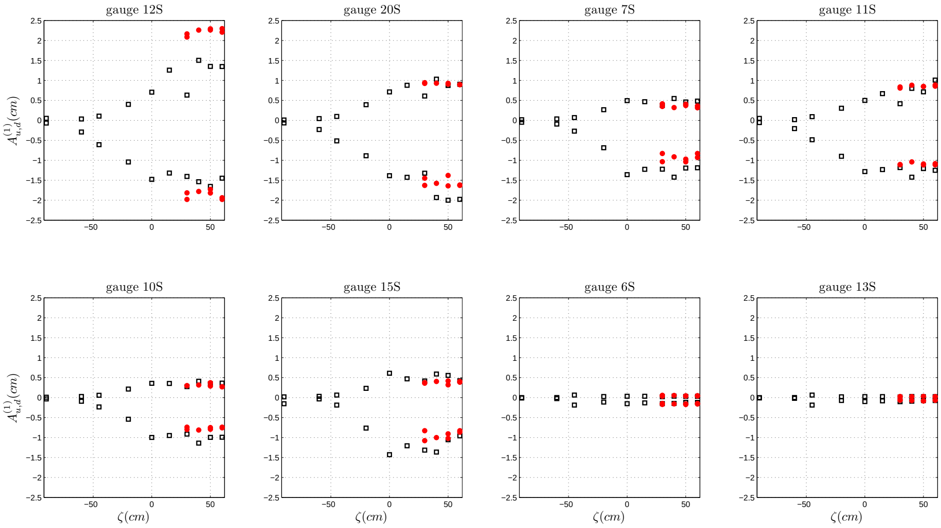

Figure 2.23: Comparison between experimental (solid circles) and numerical results (squares) at wave gauges for first wave induced perturbation as a function of falling height ζ.

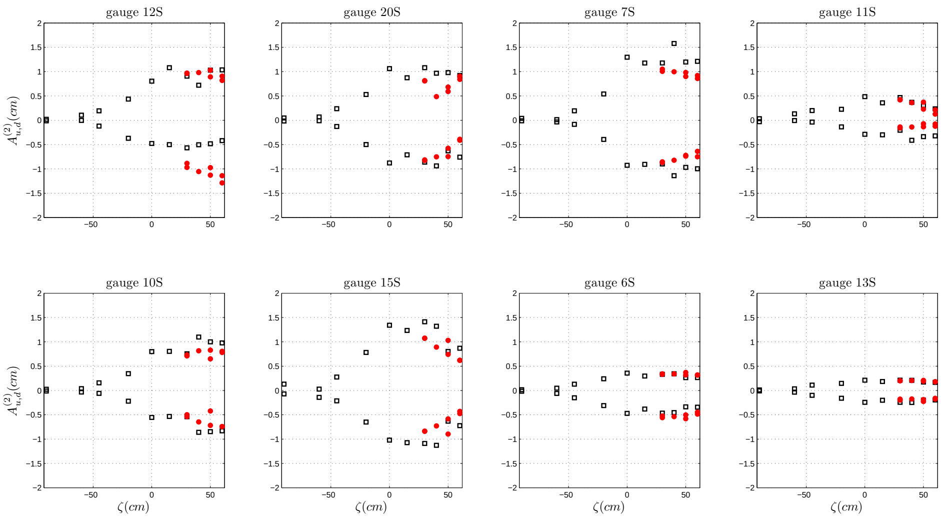

Figure 2.24: Comparison between experimental (solid circles) and numerical results (squares) at wave gauges for second wave induced perturbation as a function of falling height ζ.

2.5.2 Comparison between subaerial and submerged landslide

In order to better understand the difference between subaerial and submerged landslide generated waves, the shape and magnitude of a completely submerged landslide, with a release distance $\zeta = -0.9$ m have been considered. The induced wave run-up and radiating wave amplitude are about one order of magnitude smaller if compared with the case of subaerial landslide. Furthermore, being the waves generation mechanism different, also the wave forms are different.

Figure 2.25 shows the run-up and run-down time series for $\zeta = 0.4$ m (dashed line) and $\zeta = -0.9$ m (continuous line). In order to make detectable the submerged landslide generated waves two different y-axis are employed in the Figure.

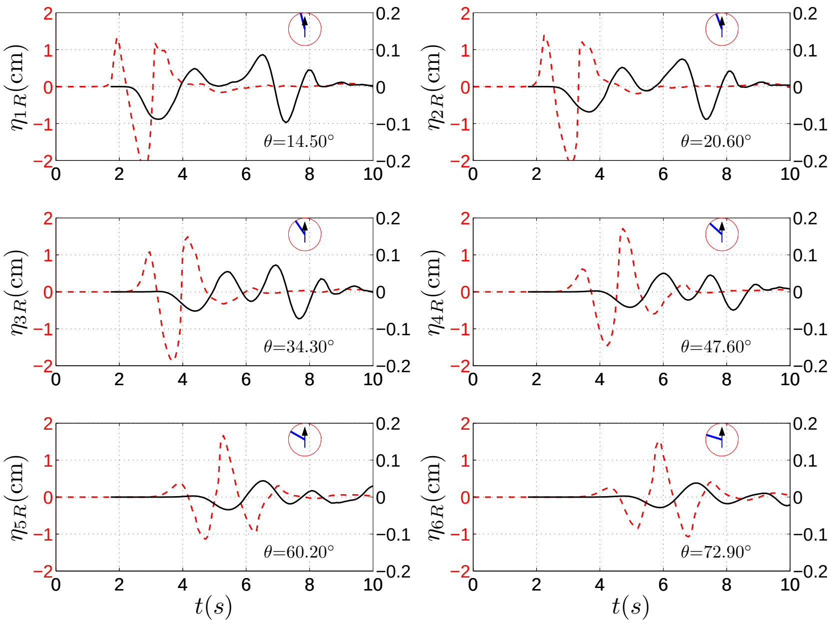

Figure 2.25: Comparison between the waves generated at the run-up gauges by a subaerial (ζ=0.4 m) and a submerged (ζ=-0.9 m) landslide. Two different y-axis are employed. The left one refers to the aerial landslide, the right one to the submerged landslide generated waves. In order to compare the two time series, the $\zeta = -0.9$ m results have been shifted of 1.7 s forward in time.

The left one refers to the aerial landslide, the right one to the submerged landslide generated waves. In order to compare the two time series, the $\zeta = -0.9$ m results have been shifted of about 1.7 s forward in time, in order to have the landslides in the same position at the instant $t = 1.7$ s, i.e. the time needed for the landslide falling from $\zeta = 0.4$ m to reach the initial position of that with $\zeta = -0.9$ m.

The induced waves well reflect the generation mechanism. In the case of subaerial landslide the water is first pushed away, as by a piston, and then, as the landslide penetrates into the water, it generates a depression with a U-shape (Di Risio et al. 2009b). The depression is suddenly filled because of the two vertical sides collapse (Liu et al. 2005), generating the second wave crest. The submerged landslide misses the first steps and therefore does not generate the first wave crest. The depression and trailing crest that occur in this case are smaller if compared with the subaerial landslide ones. Furthermore, in the case of submerged landslide, the generated waves appear to be very much longer if compared with subaerial landslide generated waves.

Figure 2.26 shows a comparison between the run-up generated by two completely submerged landslide, considering two different landslide thickness, in particular one has a double thickness, c=0.1 m (continuous line). It could be observed how the waves are in phase and that the amplitude of the run-up and run-down is larger for the double thickness landslide. It could also be noticed that the first crest is followed by a small run-down and than by another larger crest. The ratio between the amplitude of the run-up and run-down generated by the two slides at the first three gauges has also been evaluated and reported in Table 2.4. It can be noticed that the ratio is very closed to the ratio between the landslides thickness, 2, at the first run-down but that in almost all the other cases it is greater.

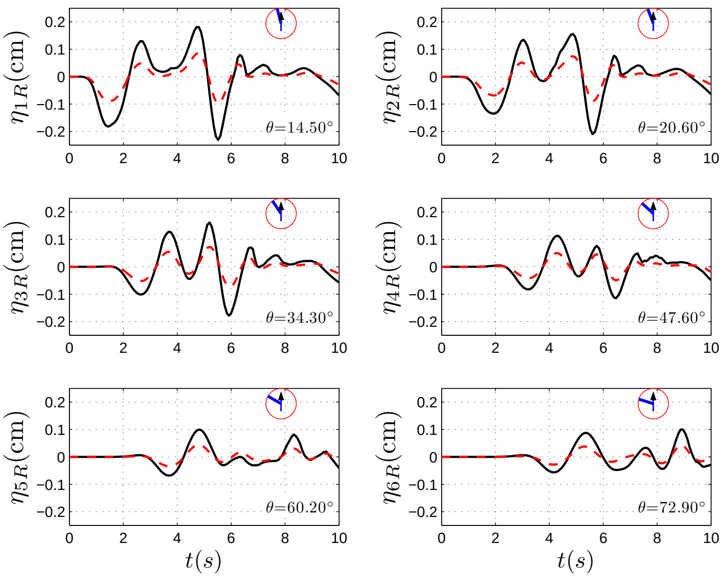

Figure 2.26: Comparison between the waves generated at the run-up gauges by two submerged landslide (ζ=-0.9 m)having different width, c=0.05 m (dashed line) and c= 0.1 m (continuous line).

Table 2.4: Te ratio between run-up and run-down amplitude generated by two submerged landslide: the one of the experiments (c=0.05 m) and one with a double thickness (c=0.1 m).

	$R_d^{(1)}$(cm)	$R_u^{(1)}$(cm)	$R_d^{(2)}$(cm)	$R_u^{(2)}$(cm)	$R_d^{(3)}$(cm)	$R_u^{(3)}$(cm)
1R,c=0.1m	-0.179	0.130	0.0173	0.181	-0.231	0.079
1R,c=0.05m	-0.088	0.046	0.003	0.084	-0.09	0.045
ratio	2.03	2.84	6.06	2.15	2.49	1.75
2R,c=0.1m	-0.135	0.135	-0.001	0.156	-0.210	0.076
2R,c=0.05m	-0.067	0.052	-0.001	0.075	-0.088	0.042
ratio	1.96	2.60	1.00	2.08	2.40	1.84
3R,c=0.1m	-0.101	0.128	-0.044	0.162	-0.178	0.071
3R,c=0.05m	-0.052	0.055	-0.026	0.073	-0.073	0.036
ratio	1.95	2.32	1.73	2.22	2.45	2.00

2.5.3 The influence of the landslide shape

Another parameter that has been varied is the landslide shape. In particular three different cases have been considered, varying the dimensions of the falling body, as shown in table 2.5 and in figure 2.27, with ζ=0.5m.

Table 2.5: The three different landslide shapes.

	a(m)	b(m)	c(m)
experimental	0.8	0.4	0.05
90° turned landslide	0.4	0.8	0.05
double thickness	0.8	0.4	0.10

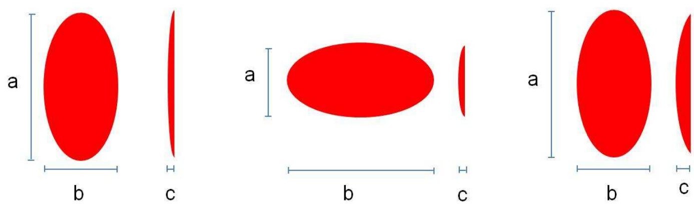

Figure 2.27: The experimental, the 90° turned and the double thickness landslides.

It was observed by Di Risio et al. (2011) that, for the case of subaerial landslide, Ataie-Ashtiani and Nik-Khah (2008a) suggested that the shape does non affect substantially the generated waves. However, comprehensive and parametric experimental investigations aimed at evaluating the influence upon the generated waves of the slope of the landslide front (γ) have not been carried out so far at our knowledge. The topic was only tackled by Kamphuis and Bowering (1970). It must although be underlined that Watts et al. (2005) indicate that semi-elliptical shaped rigid body represents the worst case scenarios, at least for underwater landslides (Watts, 2000; Enet and Grilli, 2007; Di Risio et al., 2009a;b) and also that Watts and Grilli (2003) and Watts et al. (2005) found that the higher the spreading of Gaussian shape, the lower the amplitude of generated waves, at least for underwater landslides.

The two simulated cases added to the experimental one, are characterized by having an higher landslide front slope angle in the x direction, while in

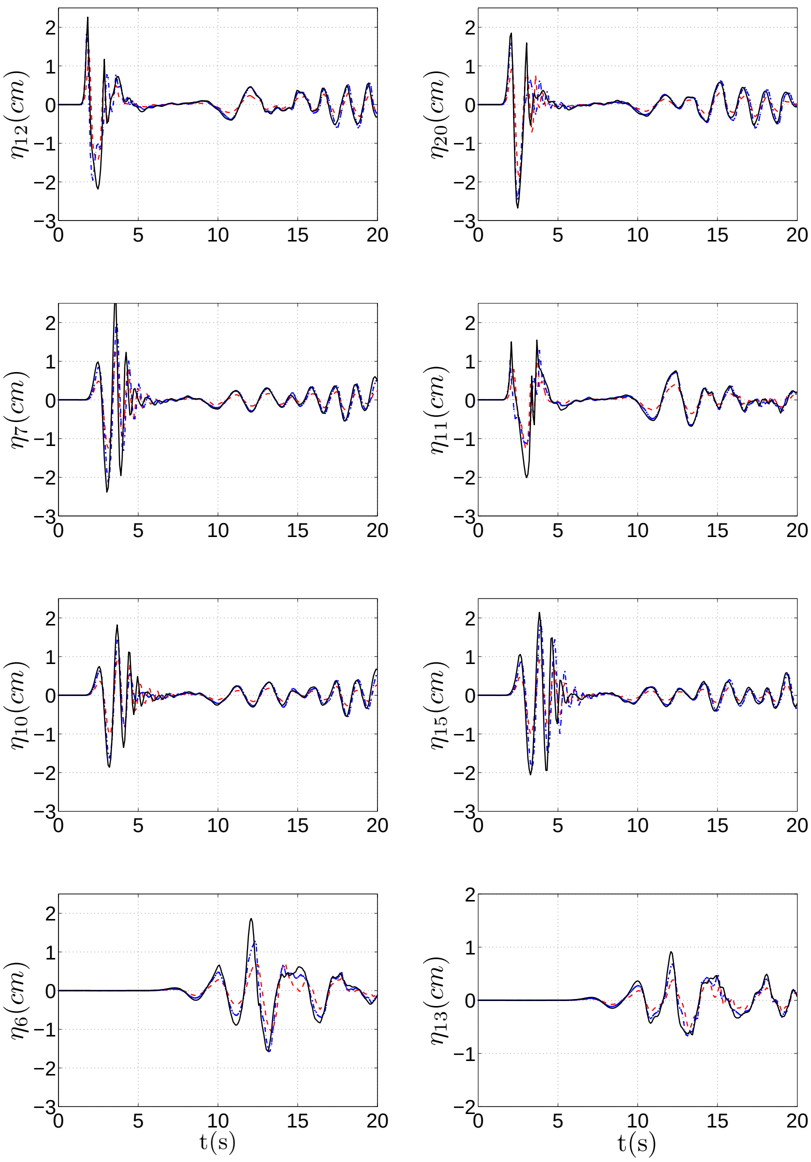

Figure 2.28: Comparison between the waves generated at the sea level gauges by landslides with different shapes; the experimental (red dashed line), the 90° turned (blue dashed line) and the double thickness (black continuous line) landslides.

θ direction in the first case, the 90° turned landslide, the slope is smaller and in the second, the double thickness landslide, higher. Moreover in the first case the time needed by the body to completely enter into the water is reduced.

Figure 2.28 shows the comparison at the sea level gauges of the propagating waves in the three simulated cases; dashed blue line is the 90° turned landslide, the red dashed is the experimental one and the black continuous is the double thickness one.

It could be observed that the generated waves are perfectly in phase but also that bigger amplitude in the cases on 90° turned and double thickness landslides result. When observing figure 2.29, on the contrary, it could be noticed that, although waves are still almost in phase, the higher run-up is generated by the double thickness landslide with a difference with the waves generated by the experimental case that is smaller than at the off-shore gauges. It could also be underlined that the run-up of the first wave generated by the turned landslide is very small and that in this case the second wave is higher also at the first gauge. It seems from these results that the overall behaviour for the turned and double thickness landslide is characterized by an higher propagation offshore, along the landslide axis, than laterally. Regarding the lateral spreading other considerations could arise, related to the generation mechanism. It seems that, in the case of the turned landslide, because of the small lateral body volume, the first wave run-up is very small and that then, the collapse of the two lateral fronts generates an higher second wave run-up. In the case of the double thickness it seems that the influence of the changed volume of the landslide is focused on the first wave run-up more than on the second.

Figure 2.30 shows a comparison of the generated wave field by the experimental landslide (on the left) and the double thickness and the 90° turned landslide (on the right). The white area represent the highest crest, while the black the largest troughs. The red lines represent the position of he run-up gauges. The pictures show clearly how, in both cases, the waves spread more off-shore than laterally and how the fronts are similar although they go faster than in the experimental case.

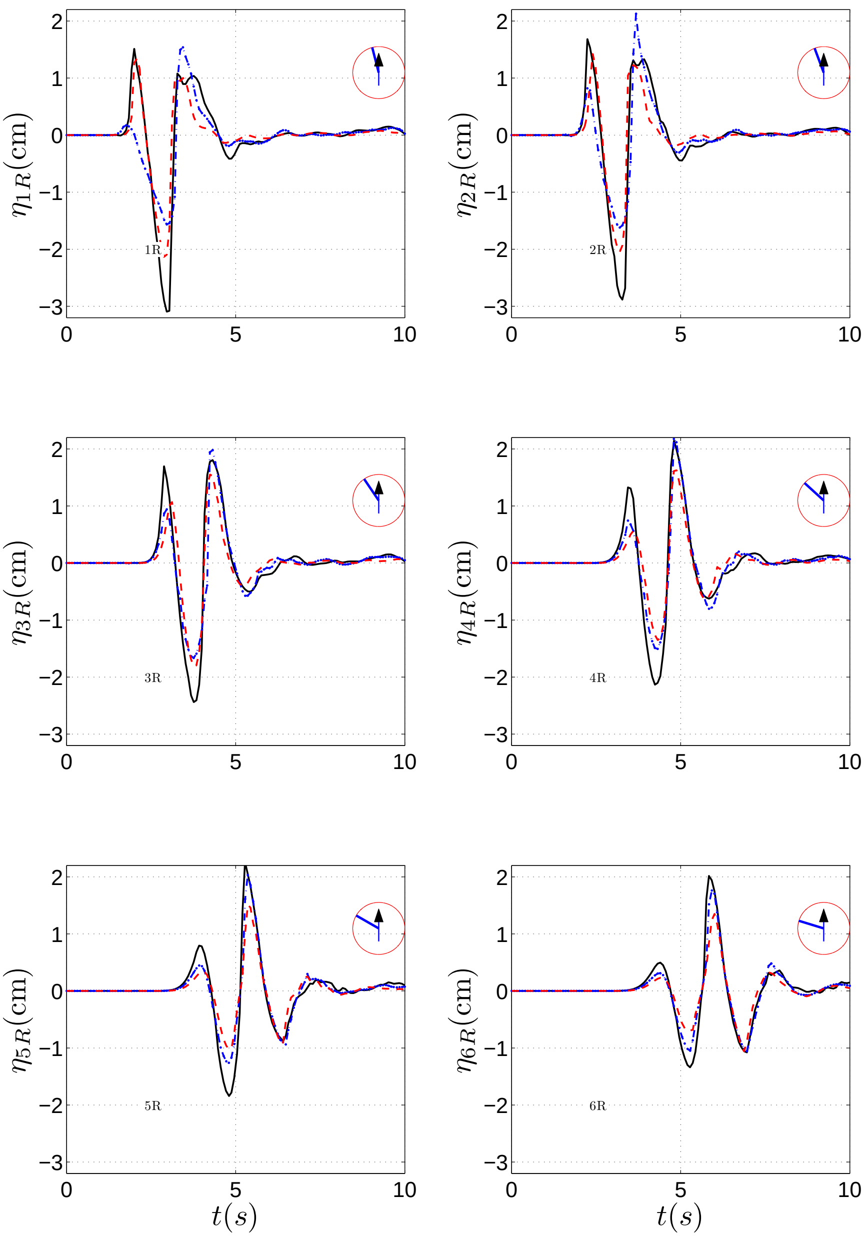

Figure 2.29: Comparison between the waves generated at the run-up gauges by landslides with different shapes; the experimental (red dashed line), the 90° turned (blue dashed line) and the double thickness (black continuous line) landslides.

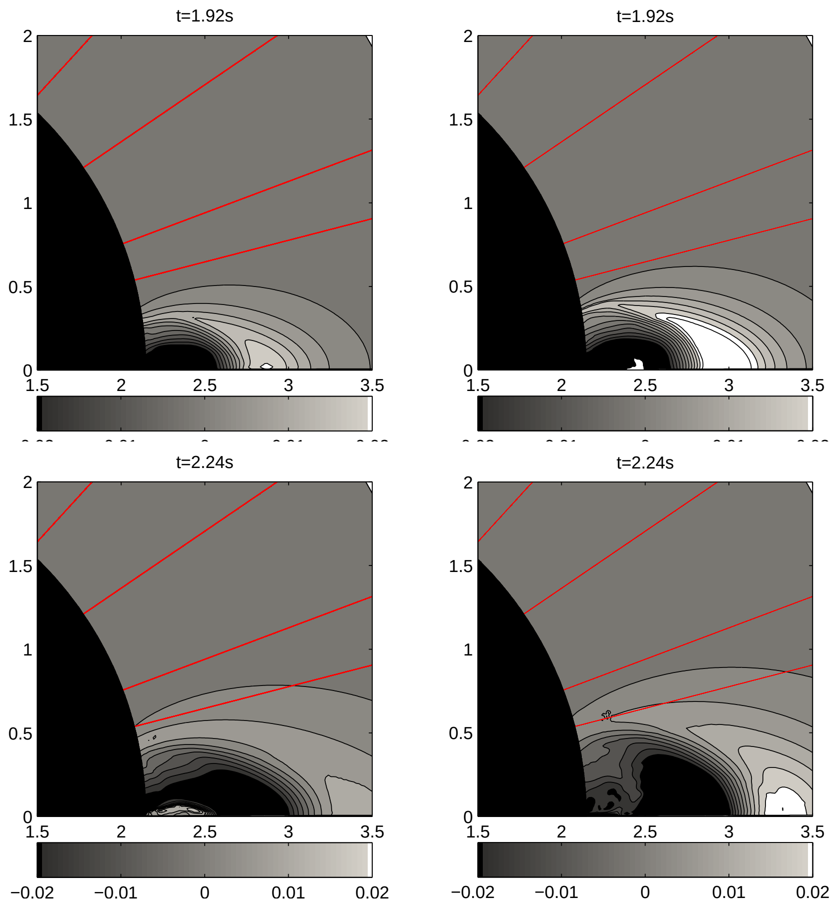

Figure 2.30: UP.Comparison of the wave field generated by the experimental (left) and by the double thickness landslide (right) after 1.92s. DOWN. Comparison of the field generated by the experimental (left) and by the 90° turned landslide (right) after 2.24 s.

2.5.4 The influence of the island radius

Another parameter that has been changed is the island radius. It has been varied considering one smaller, called r_{min}, and one larger radius, r_{max}, keeping constant the increasing and decreasing ratio (r_{min}/r_{exp}=0.78, r_{exp}/r_{max}=0.78). To carry out these simulations the slope of the island flank and the initial water depth have not been varied (1/3 and 0.8 m respectively) and the falling height of the body that has been analyzed is ζ=0.5 m.

Because of the constant ζ and flank slope, the falling body velocity has not changed. Figure 2.31 shows the comparison at the run-up gauges of the generated waves in the case of the experimental island (red dashed line), of the larger radius (blue dashed line) and of the smaller radius (black continuous line). It could be in general observed a shift of the arrival time of the waves at each gauge. In the case of the larger radius, waves are bigger at the first gauges, arriving, obviously, later than the ones of the experiment; the first wave decreases rapidly going away from the generation area, because of the longer distance covered, while the third wave rise earlier. In the case of the smaller radius waves arrive earlier, they are a little bit smaller at the first gauge and they have a lower decrease. Table 2.6 shows, for the three different island radius the traveled distances to reach the six gauges and the maximum run-up generated by the first and the second wave at each gauge.

Table 2.6: Traveled distances, s, and maximum run-up generated by the first ($R^{(1)}$) and the second wave ($R^{(2)}$) at the first 6 run-up gauges considering the 3 different island radius.

	s_1(m)	s_2(m)	s_3(m)	s_4(m)	s_5(m)	s_6(m)
r_{min}	0.40	0.57	0.95	1.33	1.68	2.04
r_{exp}	0.52	0.74	1.22	1.70	2.15	2.61
r_{max}	0.66	0.93	1.56	2.16	2.73	3.30
	$1R^{(1)}$(cm)	$2R^{(1)}$(cm)	$3R^{(1)}$(cm)	$4R^{(1)}$(cm)	$5R^{(1)}$(cm)	$6R^{(1)}$(cm)
r_{min}	0.96	1.12	1.21	0.99	0.82	0.32
r_{exp}	1.34	1.42	1.07	0.56	0.34	0.23
r_{max}	1.41	1.36	0.83	0.43	0.027	0.19
	$1R^{(2)}$(cm)	$2R^{(2)}$(cm)	$3R^{(2)}$(cm)	$4R^{(2)}$(cm)	$5R^{(2)}$(cm)	$6R^{(2)}$(cm)
r_{min}	0.83	1.01	1.17	1.34	1.24	1.19
r_{exp}	1.00	1.23	1.55	1.63	1.51	1.35
r_{max}	1.34	1.46	1.71	1.44	1.50	1.58

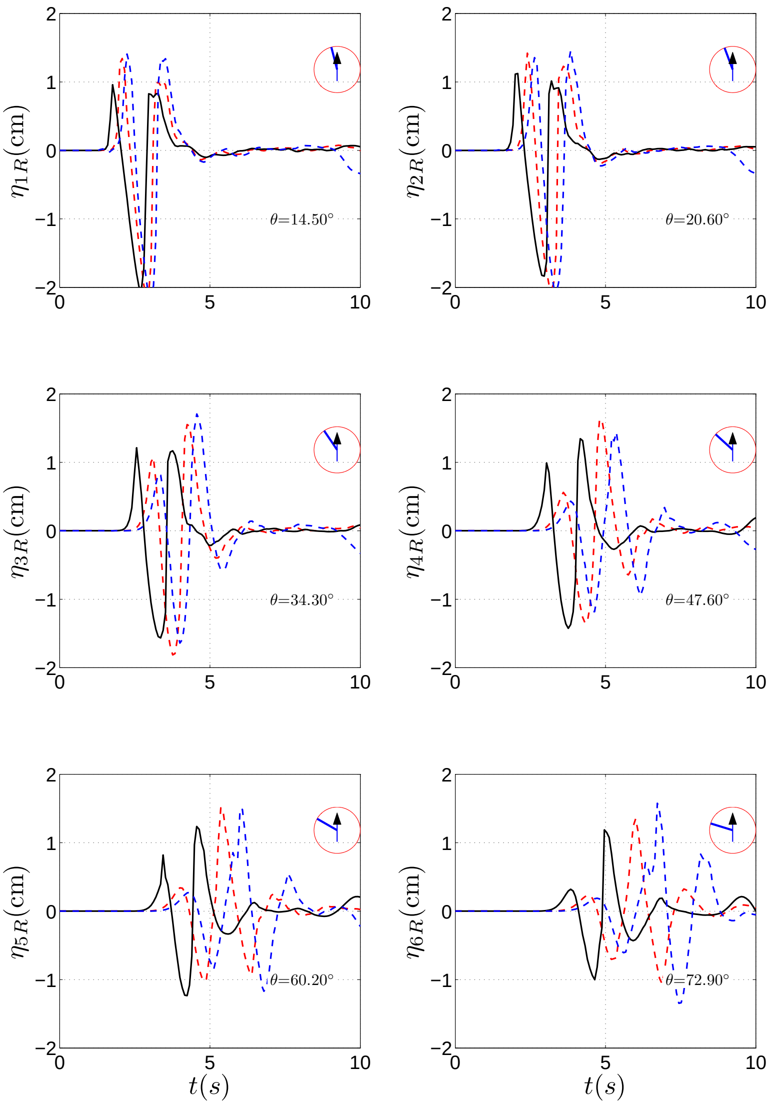

Figure 2.31: Comparison between the waves generated at the run-up gauges considering three different island radius; the experimental (red dashed line) , r_{min} (continous black line), r_{max} (blue dashed line).

Figure 2.32 shows the spatial distribution of run-up and run-down generated by the first ($R^1_{u,d}$) and the second wave ($R^2_{u,d}$) in the three different cases as a function of the curvilinear abscissa s. Diamonds represent the results for r_{min}, squares for r_{max} and circles r_{exp}. It could be observed for both waves a similar behaviour for the three radius; the maximum run-up and run-down by the first and second wave are located at almost the same distance from the generation area, the run-up at less than 1 m for the first wave and at about 3 m for the second. It could also be noticed that the amplitude of both run-up and run-down, especially for the second wave, is smaller in the case of the smaller radius and a little bit higher for the larger radius. The difference with the experimental results seems to be higher for the smaller radius than for the larger one. So, concluding, as observed in DI Risio et al. (2009a), run-up increases when undisturbed shoreline radius increases, and the point at which the maximum runup occurs moves away from the generation area, especially for the second wave.

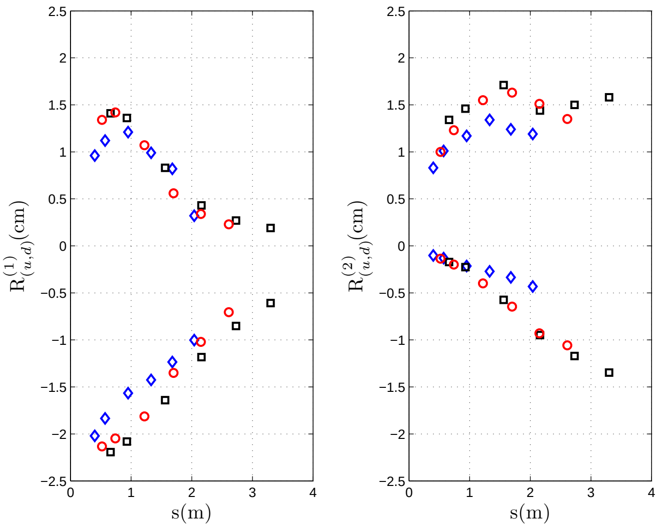

Figure 2.32: spatial distribution of run-up and run-down generated by the first ($R^1_{u,d}$, left) and the second wave ($R^2_{u,d}$, right) in the three different cases as a function of the curvilinear abscissa s. Diamonds represent the results for r_{min}, squares for r_{max} and circles r_{exp}.

2.6 Conclusions

In this section 2D and 3D numerical simulations of tsunamis generated by landslides have been presented. The commercial fully three-dimensional model FLOW-3D has been used and the results have been compared with experimental data. Very good agreement between numerical and experimental results have been obtained, suggesting that the model can be considered to be very accurate for the problem at hand.

Numerical results show that the model can be successfully used for simulating the interaction between moving objects and fluid, also reproducing propagation phenomena related to generated waves, both offshore and along the coast. The model is able to reproduce the waves both very close to the generation area and in the far field, as confirmed by the results at the run-up gauges nearest to the impact area and by the offshore surface gauges in the conical island simulations. However, in the very near field, depending on the grid resolution, high frequency components are not well reproduced, thus underestimating the height of the waves. FLOW-3D has proven to be very accurate also for the calculation of inundation/drying of the island, since predicted shoreline displacements appear to be in agreement with the measured ones.

It finally appears feasible to apply a three-dimensional model such as FLOW-3D to simulate the whole processes of generation, propagation and inundation of landslide tsunamis around an island; computational costs, even if high, are acceptable (36 hours on a standard PC for each simulation of the conical island). The high accuracy suggests the use of the model for few, accurate precomputed inundation maps. It must be underlined that to achieve the results here presented for the conical island there was no need of any calibration of the numerical model.

The results of the parametric analysis have shown the great potentiality of the numerical model to investigate the phenomenon at hand. In particular it has been possible to investigate the differences between subaerial and submerged landslide generated waves and how the shape of the landslide can influence wave generation and spreading. It could also be observed how the diameter of the island influences the coast inundation. Finally it can be noticed that the comparison between numerical and experimental results would be more challenging if velocity measurements from the experiments would be available, even if in such a large scale experimental layout velocity measurements are quite difficult.

Chapter 3

The extreme wind wave heights statistical model and its application to the Italian coast

3.1 Extreme value statistics. Literature review

There are some situations in which extreme values are the most important part of the problem. By definition extreme values are scarce and usually estimates are required on greater number of data than the one observed. This implies an extrapolation from observed levels to unobserved levels. One way to study extreme events is to use the statistical tool of the Extreme Value Theory (EVT). It tries to use all the few available information from the tail of a distribution, do not considering all the other data. One of the most important references on EVT is the work of Gumbel (1958). Gumbel has applied EVT on climate and hydrology. It could be mentioned also the works of Fréchet (1927) who introduced asymptotic models to obtain extreme distribution, Fisher and Tippett (1928) who demonstrated that the distribution limit could converge to just three kind of distribution, Gnedenko (1943) gave a rigorous mathematical justification to the effect that there are just three types of distribution that can arise as limiting distributions of extremes in random samples. Weibull (1939) introduced EVT in different physical and engineering applications. In recent past the mathematical elaborations that characterize the properties of the extreme distribution and their applications could be find in Galambos (1987) and

Resnick (1987). There are also some books on EVT as Kotz and Nadarajah (2000), Coles (2001) and the technical note by Smith (2001).

Nowadays there are two methodologies to solve an extreme value asymptotic model:

1. The classical approximation of extreme value based on theorem I or theorem of Fisher-Tippet (Galambos, 1987).

2. The approximation in which the adaptation of the distribution tail is only carried out. It is based on theorem II or Pickands theorem (Pickands, 1975).

The difference between the two methods is in the starting data. Theorem I considers data coming from the whole population, for instance the annual maxima of a time series, while theorem II considers just the higher data, the ones that exceed a given threshold (POT method, Peak Over Threshold).

Gumbel in his work of 1958 proposed a statistical methodology for extreme values based on fitting the extreme value distributions to data consisting of maxima or minima of some random processes over a fixed time interval, for instance over one year. The fitting at the annual maxima of a temporal series could be carried out, as in more recent works, for instance in Smith (1985), with the generalized extreme values distribution which combines the three types of Fisher-Tippett and Gnedenko into a single three-parameters distribution.

Threshold methods are more flexible than annual maxima methods firstly because, taking all the exceedances over a suitable high threshold into account, they use the data more efficiently and secondly because it comes easier to study the relationships between the extreme levels and some other variables (Smith 2001). For exceedances could be find an analog of the three types theorem but it leads to a different distribution, the generalized Pareto distribution.

Many application of extreme value modeling could be find in literature on Wind Engineering (Harris 2001), assessment of meteorological change (Thompson et al. 2001), assessment of the largest extreme rainfall amounts (Koutsoyannis 2004) or on ocean wave modeling (Dawson 2000).

3.1.1 Extreme waves statistics. Literature review

Wind waves strongly affect all kinds of maritime activities, and their worst effects usually come from the highest waves. For this reason the prediction of the highest wind waves becomes a very important goal in the scientific community.

The paper of Guedes Soares and Scotto (2001) deals with the application of different methods to estimate the occurrences of high sea states. A case study of the Norwegian continental shelf is considered. The Annual Maxima Method and the Peak Over Threshold Method are used to obtain return values for different return periods, Tr. Several parametric models are also used to fit the long-term distribution of significant wave height and to obtain predictions of extremes values. It is shown that the prediction of these sea states depends very much on the tail behaviour of the fitted distribution and that if one wants to make predictions of extreme values the POT method should be preferred.

The same authors in 2004 presented a work on the extremal properties of time series of significant wave height modeled by means of extreme value techniques. They use the limiting joint generalized extreme value (GEV) distribution for the r largest-order (upper-range data) statistic model to estimate return values of significant wave height. A method based on filtering the observations to extract the r largest independent values is adopted and a case study of the northern North Sea data set is presented, comparing the results with those obtained from the Annual Maxima (AM) method. The general conclusion is to favor the method based on the joint GEV distribution.

In 2004 the Italian Wave Atlas was published by APAT now ISPRA, Istituto Superiore per la Protezione e la Ricerca Ambientale))and University of Roma Tre (Franco et al. 2004). This book provides a characterization of the Italian wave climate focusing on extreme sea waves. The data recorded by the Italian wave buoy network (RON, rete ondametrica nazionale) have been used; on them the POT method has been applied and return values of significant wave height have been evaluated finding between three different distribution the one who best fit the data.

Extreme events occur quite often in the Mediterranean basin and the hazard linked with them is mostly related to the presence of highly populated, industrialized and tourist areas close to coasts and rivers. In order to evaluate the possible occurrence of these events, as river and coastal flooding, and to correctly design engineering works is important to predict with accuracy a given return-period occurrence. Advances in the extreme value theory (see Coles, 2001, and Menéndez, 2008a, as general references) have appeared in the state-of-the-art allowing a better description of the natural climate variability of extreme events of geophysical variables. In particular, the modeling of extreme sea waves seasonality can improve the knowledge on some important natural coastal processes and could help in the analysis of coastal flooding risk and the design of maritime works. The definition of working time windows during the construction phase or

the evaluation of the harbour operation time frames after construction during the winter season requires consideration of the seasonality or monthly characteristics in the estimation of the return values. The importance of seasonal variations in extreme statistical analysis of environmental variables has been noted previously (f.i., Carter and Challenor, 1981; Morton et al., 1997; Katz et al., 2002).
A research group of IHCantabria performed in the last years a very accurate study on the variability of extreme sea waves heights. Here just some of their works are mentioned. Recently, Mendez et al. (2006) developed a time-dependent POT model to estimate long-term trends in the frequency and intensity of sever storm waves. The model considers the parameters of the distribution as functions of time (harmonics within a year, exponential long-term trend, El Niño covariate, etcetera). A similar procedure was used in Menéndez et al. (2008a) to study the variability of extreme wave heights in the northeast Pacific Ocean based on buoy measurements. Application of the model to significant wave height data sets from 26 buoys over a period of about 20 years shows significant positive longterm trends in extreme wave height. They also demonstrated an impact of El Niño on extreme wave heights in the northeast Pacific as well as important correlations with mid-latitudinal climate patterns. Ménéndez et al. (2008b) developed a time-dependent model based on the GEV distribution that accounts for seasonality. In particular a time-dependent generalized extreme value (GEV) model for monthly significant wave heights maxima. The model is applied to several time series from the Spanish buoy network. Monthly maxima show a clear non-stationary behavior within a year, suggesting that the parameters of the GEV distribution can be parameterized using harmonic functions. Results show the increased significance of the parameters involved and the reduction of the uncertainty in the return level estimation. The model provides new information to analyze the seasonal behavior of wave height extremes affecting different natural coastal processes.
Different works have been carried out to study extreme events and wave climate variability along the Italian coast, thanks also to the available data recorded by the RON (Piscopia et al, 2002; Lionello et al. 2005; Lionello et al. 2008). In Lionello et al. (2005) the variability of the monthly average significant wave height field in the Mediterranean Sea, in the period 1958-2001 is examined. Principal component analysis (PCA) is applied and it shows that the annual cycle is characterized by two main empirical orthogonal functions (EOF) patterns. It also shows that the resulting wave field variability patterns are associated with consistent sea level pressure

(SLP) and surface wind field structures, analyzing the relationships with North Atlantic Oscillation and Monsoon circulation.

Another study that could be mentioned is the technical report of Lopatoukhin (2000), that presents different methods to estimate extreme wind wave heights using several methods. In particular the Annual Maxima Method and POT method are applied on recorded wave height time series in the Baltic Sea.

3.2 The data

3.2.1 The Italian wave buoy network RON

An idea similar to the one of Ménéndez et al. (2008b), based on independent extreme significant wave heights obtained from a POT analysis, has been developed in this work. The model is applied on the dataset collected by the Italian wave recorded network RON (Rete Ondametrica Nazionale). The Italian wave recording network was activated in 1989. The first RON was composed by eight pitch-roll Datawell WAVEC directional buoys, located offshore of La Spezia, Alghero, Ortona, Ponza, Monopoli, Crotone, Catania and Mazara del Vallo (Figure 3.1).

Figure 3.1: Final layout of the RON.

In 1999 other recording WAVERIDER Datawell directional buoys were added to the previous network in Cetraro and Ancona and the Catania pitch-roll buoy was substituted by a translation one. In 2002 implementation activities of RON began to realize a reliable monitoring system and data spread in real time. Most of the network changes have been oriented to improve the efficiency of the system. The number of stations increased until 15, with the addition of 4 new buoys placed in Capo Linaro (Civitavecchia), Capo Gallo (Palermo), Punta della Maestra (North Adratic Sea) and Capo Comino (Eastern Sardegna) in 2004 and one in 2007 in front of Cagliari. Directional wave buoys TRIAXYS have been used for all RON sites from the third quarterly of 2002. The final list of the entire buoy network is shown in Table 3.1.

Table 3.1: Location of the RON buoys.

BUOY	LAT	LONG	DEPTH
ANCONA	43°49'.9N	13°42'.6E	70 m
ALGHERO	40°32'.1N	08°06'.0E	95 m
CAGLIARI	39° 6'.8 N	9° 24'.3 E	90 m
C.po GALLO	38°15'.5N	13°20'.0E	125 m
C.po COMINO	40°37'.0N	09°53'.5E	115 m
C.po LINARO	42°00'.0N	11°46'.6E	92 m
CATANIA	37°26'.4N	15°08'.8E	70 m
CETRARO	39°27'.2N	15°55'.1E	110 m
CROTONE	39°01'.4N	17°13'.2E	95 m
LA SPEZIA	43°55'.7N	09°49'.6E	90 m
MAZARA	37°31'.0N	12°32'.0E	87 m
MONOPOLI	40°58'.5N	17°22'.6E	90 m
ORTONA	42°24'.4N	14°32'.2E	70 m
PONZA	40°52'.0N	12°57'.0E	100 m
P.ta MAESTRA	44°58'.0N	12°38'.0E	30 m

Onshore a center of data reception and elaboration receives the data by radio. Data have been acquired until 2002 for 30 minutes periods every three hours, except during a sea storm, where they were collected every 30 minutes. The Hs threshold used to define a sea storm and so acquired every 30 minutes are listed in table 3.2. In 2002 data have started to be collected every 30 minutes.

Different synthetic parameters are evaluated by the network as significant wave height (Hs), peak period (Tp), mean period (Tm), and mean direction (Dm). The operational periods of the different buoys are plotted in Fig. 3.2; the recording efficiency of the buoys until 2008 is over the 80%, except at Ancona, Capo Comino,C. Linaro and Punta della Maestra. The buoys used in the extreme value analysis are shown in red. The others buoys have been discarded because of the short recorded time available. It could be noticed that some buoys have started to register again at the end of 2009. These data have not been considered in the analysis because of the big gap, larger more than one year, between the years 2008 and 2009. In addition, the data analyzed in this work have required preliminary pre-processing before the selection of the peaks over a threshold. The pre-process solved the problem of obvious outliers, different sampling intervals, etc.

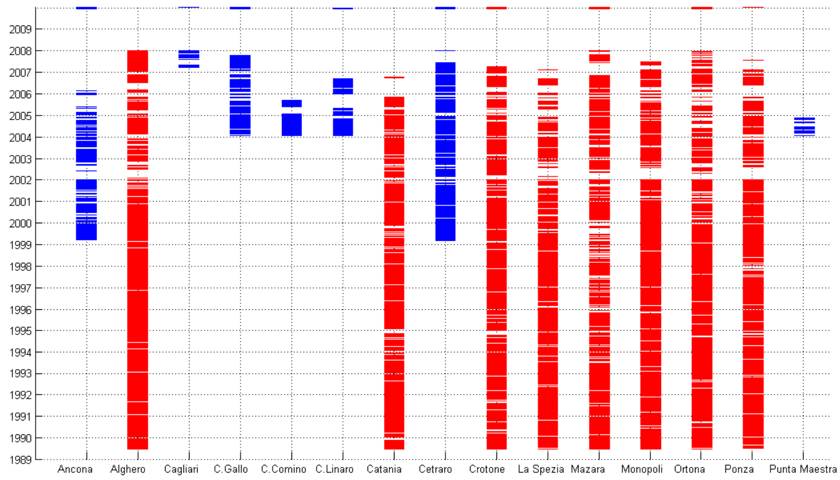

Figure 3.2: RON buoys operational periods until 2010 and the selected buoys for the extreme event analysis.

3.3 The seasonal wave climate variability

Because of the importance of seasonal variations in extreme statistical analysis, a preliminary descriptive analysis of the extreme variability within a year was developed. Figure 3.3 and 3.4 illustrate the variability within a year of the monthly maximum Hs recorded by the buoys in each month. To facilitate the visualization of the extreme events, the winter season has been placed in the center of all figures. In these plots have been shown also Ancona. Capo Gallo and Cetraro records, because of the number of data available, that is not enough for an accurate statistical analysis but could be useful to understand wave climate variability along the Italian coasts.

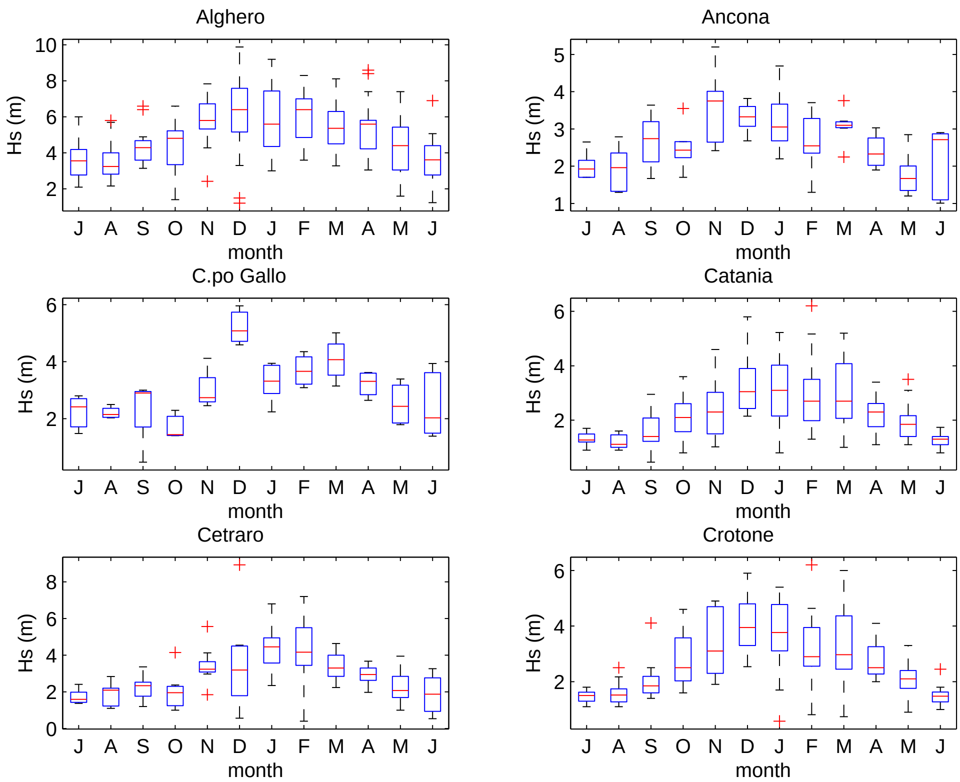

Figure 3.3: Boxplots for monthly maxima significant wave heights. Rectangular boxes have lines at the lower quartile, median and upper quartile values. The whiskers extend to the 1.5 interquartile range or to the range of the data, whichever is shorter, and crosses show unusual values.

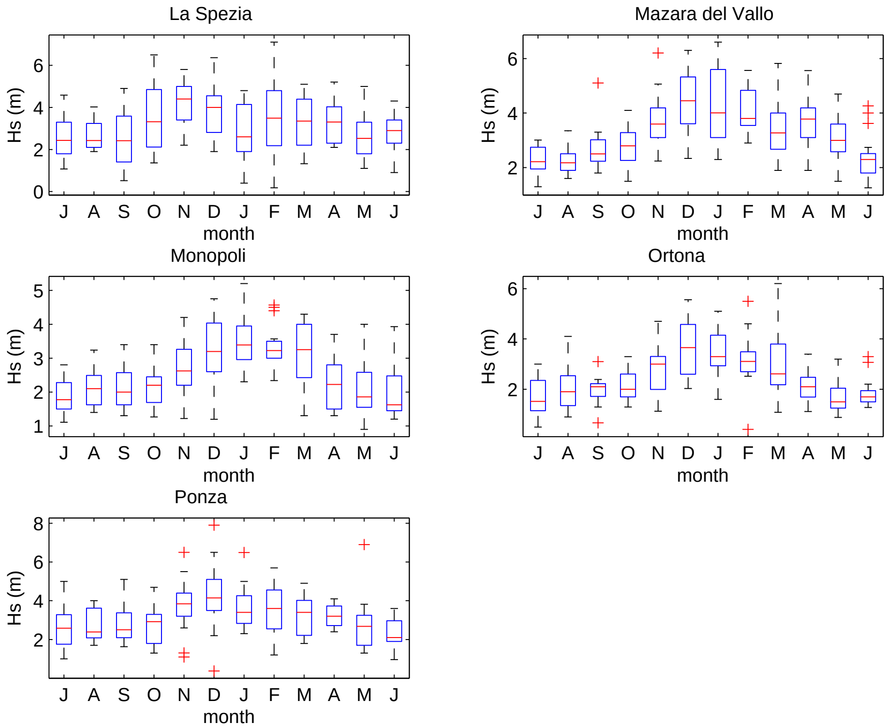

Figure 3.4: Boxplots for monthly maxima significant wave heights. Rectangular boxes have lines at the lower quartile, median and upper quartile values. The whiskers extend to the 1.5 interquartile range or to the range of the data, whichever is shorter, and crosses show unusual values.

Looking at the box plots of figure 3.3 and 3.4, an important modulation of the data is detected and it is possible to observe that the highest waves are recorded in Alghero, Cetraro and Ponza, all placed in the western Mediterranean, as remarked in Lionello et al. (2006), but also in Mazara del Vallo, located in the Straits of Sicily. In general, it seems that an evident seasonal pattern of larger Hs in winter season and lower in summertime is found for all the locations, as observed in Lionello et al. (2006). This feature is weaker in La Spezia buoy where the differences between winter and summer are smaller. A similar behavior but less evident could be found in Ponza, located in the central Tyrrenian Sea. This feature could be related to the presence in the Gulf of Genoa of cyclones during all year. In this sense, Table 1.1 shows the most active regions of the Mediterranean and

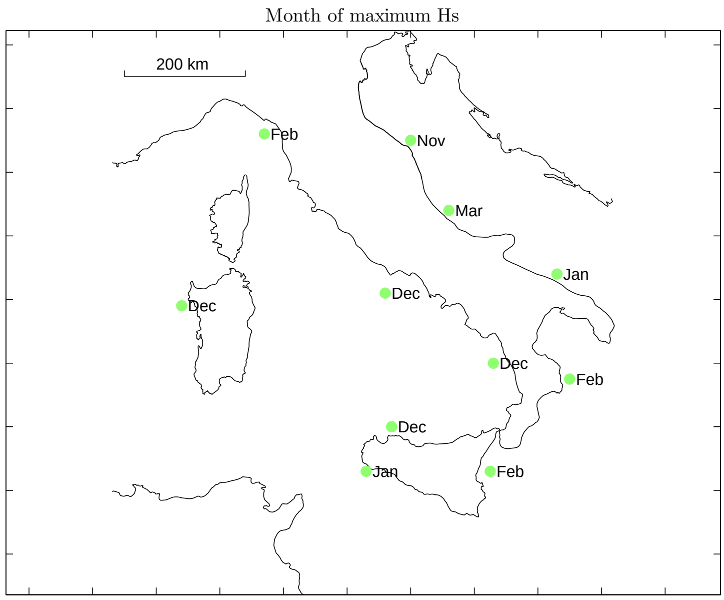

Figure 3.5: Month of the maximum recorded Hs.

their seasonality (Lionello et al. 2006).

The box plots of figure 3.3 and 3.4 also show that the distribution of maxima is characterized by higher waves in spring than in fall. Figure 3.5 shows the spatial distribution of the highest recorded waves: in the western Italian coast these have occurred almost in December, while there is a larger variability along the others coasts, especially in the Adriatic Sea. In the study of Lionello et al. (2006) it is marked that waves in the Mediterranean are mostly present only in correspondence to strong winds (windsea), in fact the swell component plays a minor role. For instance in the Gulf of Lion every year significant waves heights of more than 6 m are reached because of the high frequency and intensity of the Genoa cyclones.

The largest waves occur in the western Mediterranean and in the Ionian Sea due to the presence of Mistral and long fetches. Others winds produce smaller wave heights; Etesian winds generate two maxima, one in the Aegean and another in the Levantine Basin. Sirocco produces maxima in the northern Ionian Sea and in southern Adriatic, Bora in north Adriatic and Vendavel in the Alborean sea. An important factor that influence the generated waves in the basin is the orography of the Mediterranian area because it changes quantitatively and qualitatively the baroclinic instability processes, usually focusing the cyclogenesis (Speranza et al. 1985). The spatial variability of wave heights is joint with a seasonal variability too. The study by Lionello et al. (2005), using a Principal component analysis, PCA, has identified two main empirical orthogonal functions, EOF, that characterize the Mediterranean mean significant wave height annual cycle and that almost represent a large fraction of the total variability. The composition of the two EOFs suggest to consider four seasons: winter (Dec-Jan-Feb.Mar) with waves generated by Mistral wind, summer (Jun.Jul.Aug-Sep), with waves generated by Etesian winds, spring (Apr-May) and fall (Oct-Nov) with waves generated mostly by Libeccio and Sirocco winds.

3.4 The statistical analysis of extreme waves

3.4.1 Previous extreme analysis

In the Italian Wave Atlas (2004), the analysis carried out to forecast the values of Hs in a given time period is composed by different phases:

1. Selection of homogeneous independent data
2. Identification of the probability model that best represent the selected data
3. Determination of waves heights within a given return period
4. Calculation of the confidence interval associated to the expected value

1. In order to obtain a extreme value dataset, the POT (peak over threshold) method has been selected. The independence has been assured by selecting subsequent sea storms occurring further than two days and the climate homogeneity by defining an higher wave height threshold that allows to distinguish between local and vast meteorological perturbations (partial duration series method). The threshold values (see Table 3.2) used in the POT are equal to the averaged maximum peak occurring during the calm season (Piscopia et al. 2002).

Table 3.2: Buoys and threshold values according to the averaged maximum peak occurring during the calm season

BUOY	Threshold (m)
ALGHERO	6.0
CATANIA	3.0
CROTONE	4.0
LA SPEZIA	4.0
MAZARA	3.5
MONOPOLI	3.0
ORTONA	3.0
PONZA	3.5

2. The possible probability distribution considered are Gumbel, Fretchet and Weibull lower limited, with two (location and scale) or three (location, scale and shape) parameters. In order to choose the one who best fit the

data, a probabilistic paper with distorted coordinates was used. To represent the distribution probability as a straight line, the projected empirical data in the corresponding probability scale were plotted and a linear regression was fitted for each model using the least square method (LSM).

3. The risk that is associated to the design of maritime works is generally specified by means of the return period Tr of sea states and the occurrence probability during the work lifetime. Given a return period Tr it is possible to calculate the no-exceedance probability of the threshold H_{Tr} as:

$$F\left(H < H_{Tr}\right) = 1 - \frac{1}{\nu Tr}$$

where ν is the mean number of events over threshold observed in one year and F the cumulative distribution function. Moreover, having established the relationship between the F and Hs, choosing the best fitting statistical distribution, could be easily evaluated Hs knowing $F(H<H_{Tr})$.

4. The confidence intervals have been calculated by interpreting the results obtained by numerous Monte Carlo simulations as shown in Goda (1988). In his work he considers the standard deviation of a wave height Hs'(Tr),σ(Hs'$_{Tr}$) as the product between the standard deviation of the simulated samples (σ_x) and the standard deviation of an empirical adimentional variable z, defined as:

$$z = \frac{H'_{Tr} - H_{Tr}}{\sigma_x}$$

where Hs'$_{Tr}$ is the wave height expected value with return period Tr and H_{Tr} is the expected wave height value with the same return period, calculated on the basis of the distribution assumed during the Monte Carlo simulation. The confidence interval of the estimated corresponding to a significant value of 95% is equivalent to:

$$\pm 1.96\sigma(\mathrm{Hs'}_{\mathrm{Tr}})$$

3.4.2 The non-stationary extreme value method

In this new extreme value analysis the following methodology has been carried out:

1. Selection of extreme values
2. Determination of the extreme value statistical model that best represent the selected data.
3. Assessment of wave heights associated to a given return period.
4. Calculation of the confidence intervals of the extreme H return values.

1. Selection of extreme values
In order to select a extreme value dataset, a procedure similar to the one of the Atlas dataset has been used. The POT (peak over threshold) method has been applied to select a sample of extreme values for each buoy. The thresholds have been chosen by following two criteria: a) the averaged maximum peak occurring during the calm season; and b) the value associated to the 99.5 empirical percentile of the total record for each buoy. The former allows a comparison between the Italian Atlas extreme value methodology and the time-dependent extreme value analysis, since similar thresholds and time records were chosen in order to use identical samples of extreme values. The latter defines an objective criterion to define a threshold and guarantees the selection of values in the upper tail of the distribution. The independence has been assured in both thresholds criteria by selecting subsequent sea storms with peaks occurring with a time-lag larger than two days. Table3.3 shows the selected thresholds using the second criterion.

The buoy Hs time series and the selected extreme values (red circles) over the considered threshold (black horizontal line) are shown in Figure 3.6 and 3.7.

Table 3.3: The periods of the available data, thresholds used in the time varying extreme value analysis, corresponding to the 99.5% empirical percentile, the number of selected events and the mean number of events per year (ν).

BUOY	Recording time	Threshold(m)	Nevents	ν
Alghero	07/1989 - 04/2008	6.5	47	2.47
Catania	07/1989 - 10/2006	3.5	29	1.70
Cetrara	01/1999 - 04/2008	4.0	21	2.30
Crotone	07/1989 - 07/2007	4.0	36	2.00
La Spezia	07/1989 - 03/2007	4.4	39	2.20
Mazara del Vallo	07/1989 - 04/2008	4.2	49	2.6
Monopoli	07/1989 - 04/2008	3.4	45	2.40
Ortona	07/1989 - 03/2008	3.5	42	2.20
Ponza	07/1989 - 07/2007	4.0	50	3.33

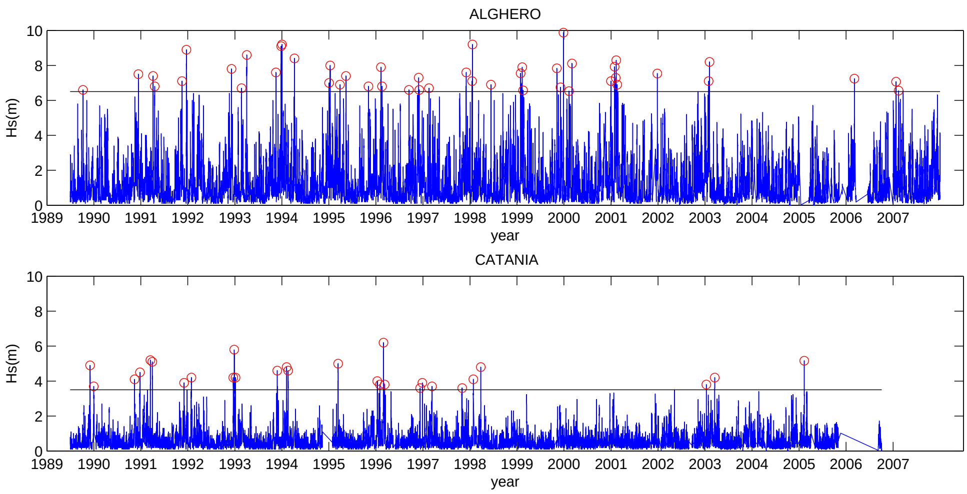

Figure 3.6: Time series and the extreme events selected (red circles) over the threshold (black line).

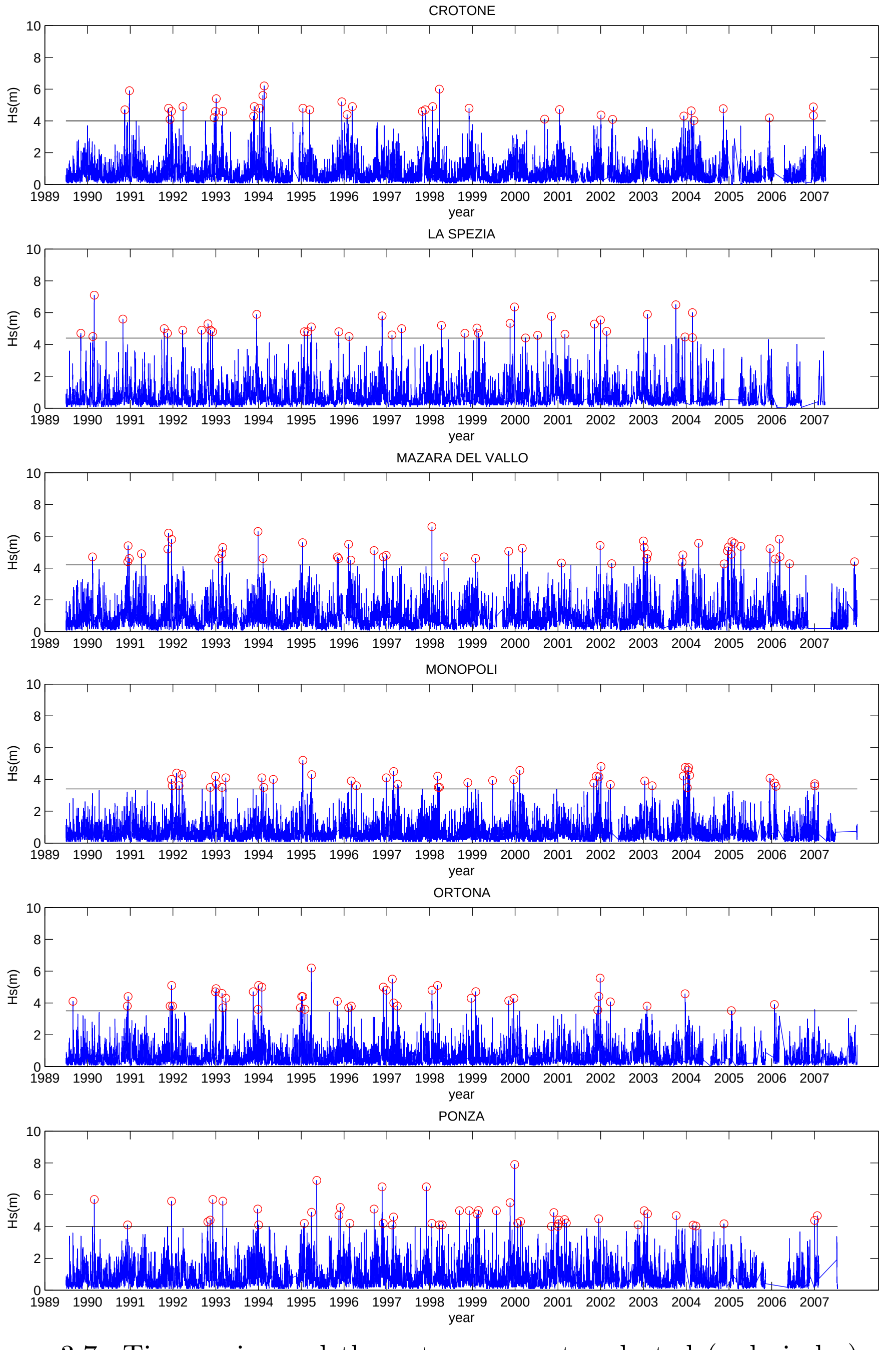

Figure 3.7: Time series and the extreme events selected (red circles) over the threshold (black line).

2. The time varying statistical model

A simple model in extreme value theory is the annual maxima method, which uses only annual maxima values. This is modeled using the generalized extreme value distribution (GEV) given by

$$F(x,\mu,\psi,\xi) = \begin{cases} \exp\left[-\left(1+\xi\frac{x-\mu}{\psi}\right)^{-1/\xi}\right], & \xi \neq 0, \\ \\ \exp\left[-\exp\left(-\frac{x-\mu}{\psi}\right)\right], & \xi = 0, \end{cases} \tag{3.1}$$

where $1+\xi(x-\mu)/\psi>0$, μ is a location parameter, ψ a scale parameter and ξ is the shape parameter which determines the nature of the tail of the distribution. The value of ξ distinguishes different classes of extreme value distribution:

- $\xi = 0$ Gumbel distribution (I type)
- $\xi > 0$ Frechet distribution (II type)
- $\xi < 0$ Weibull distribution for maxima (III type)

An important problem in extreme-value analysis is the scarcity of data for model estimation. To mitigate this problem, the POT method has been used for independent and identically distributed random variables. The basic idea is to pick up a high threshold u and to study the exceedances over this threshold, assuming that the number of exceedances of the level u in any given year follows a Poisson distribution with mean λ and that the excess values y = x-u are modeled using the generalized Pareto distribution, GPD (Pickands, 1975) given by

$$G(y;\sigma,\xi) = \begin{cases} 1-(1+\xi y/\sigma)^{-1/\xi}, & \xi \neq 0, \\ \\ 1-\exp(-y/\sigma), & \xi = 0, \end{cases} \tag{3.2}$$

where σ is a scale parameter and ξ is the shape parameter (similar as in the GEV distribution). The combination of both models for frequency and intensity can be expressed in terms of the GEV parameters for annual maxima:

$$\sigma = \psi + \xi\,(u-\mu)$$

$$\lambda = (1+\xi\,(u-\mu)\,/\psi)^{-1/\xi}$$

Moreover, the hypothesis of homogeneity in the random variable y can be relaxed to model the non-stationarity caused by seasonal effects (Méndez et al., 2006). This extension of the GPD-Poisson model is obtained by allowing its parameters to be time dependent, so that λ(t)>0, σ(t)>0 and -∞< ξ(t)< +∞ may vary throughout the year. Accordingly, the GEV distribution has time-dependent parameters -∞< μ(t)< +∞,-∞< ψ(t)< +∞ and -∞< ξ(t)< +∞; for example they may contain sinusoidal waves representing seasonal effects.

Time variability is represented in the model allowing the parameters in the GEV to be time-dependent, using parametric expressions for the location, scale and shape parameters (μ(t), ψ(t) and ξ(t)). In this work the variations within a year of extreme events of Hs has been introduced in the model by means of sinusoidal functions that represent the annual cycle (first harmonic), a possible semiannual cycle (second harmonic) and a quarterly cycle (third harmonic).

$$\begin{aligned}
\mu(t) &= \beta_0 + \sum_{i=1}^{P_\mu} \left[\beta_{2i-1}\cos(i\omega t) + \beta_{2i}\sin(i\omega t)\right] \\
\psi(t) &= \alpha_0 + \sum_{i=1}^{P\psi} \left[\alpha_{2i-1}\cos(i\omega t) + \alpha_{2i}\sin(i\omega t)\right] \\
\xi(t) &= \gamma_0 + \sum_{i=1}^{P\xi} \left[\gamma_{2i-1}\cos(i\omega t) + \gamma_{2i}\sin(i\omega t)\right]
\end{aligned}$$

where β_0, α_0 and γ_0 are mean values; β_i, α_i and γ_i are the amplitudes of the harmonics; ω=2π year^{-1}; P$_\mu$, P$_\psi$ and P$_\xi$ determine the number of sinusoidal harmonics in a year (the largest parameterization in this model is the expression for P$_\mu$=P$_\psi$=P$_\xi$= 3) and t is given in years.

The method of maximum likelihood estimation is used to estimate the model parameters (Smith, 2001).The log-likelihood function to maximize is:

$$\begin{aligned}
l(y;\theta|t_i) &= \left\{\eta_{t_i}\log\lambda\left(t_i\right) - \frac{\lambda(t_i)}{T_S} - \eta_{t_i}\log\sigma\left(t_i\right) - \eta_{t_i}\left(1+\frac{1}{\xi(t_i)}\right)\right. \\
&\qquad \left.\log\left(1+\xi(t_i)\frac{y_i}{\sigma(t_i)}\right)\right\}, \qquad \xi \neq 0 \\
l(y;\theta|t_i) &= \sum_{i=1}^{N}\left\{\eta_{t_i}\log\lambda\left(t_i\right) - \frac{\lambda(t_i)}{T_S} - \eta_{t_i}\log\sigma\left(t_i\right) - \eta_{t_i}\left(\frac{y_i}{\sigma(t_i)}\right)\right\}, \quad \xi = 0
\end{aligned} \tag{3.3}$$

Where η_{t_i} equals 1 if there is an exceedance on day t$_i$ and 0 otherwise; T$_s$ is a time scaling constant so that T$_s$=365.25 (for a daily time interval);

y_i is the threshold excess on day t_i; θ is a vector of regression parameters; the sum over t is extended to all the days with data available (i.e., days without data are omitted).

Next step of the methodology is to find the best combination of sinusoidal waves. That is, the simplest model which explain more variance of the sample. Following Menéndez et al. (2009), a codification has been created to identify easily which are the chosen parameters for the optimal model,

$$c = [g_1 g_2 g_3 . g_4 g_5 g_6 . g_7 . g_8 g_9],$$

where g_i are binary genes which represent given factors. Each gene g_i has two possible values, g_i=1 if the ith factor is switched on and g_i=0 if it is switched off. Gene g_1 represents the annual cycle (β_1, β_2) for the location parameter, g_2 (β_3, β_4) the semiannual cycle for the location parameter, g_3 (β_5, β_6) the quarterly cycle for the location parameter, g_4 (α_1, α_2) the annual cycle for the scale parameter, g_5 (α_3, α_4) the semiannual cycle for the scale parameter, g_6 (α_5, α_6) the quarterly cycle for the scale parameter, g_7 is a gene that includes a constant non-zero shape parameter (γ_0), g_8 (γ_1, γ_2) allow for the annual cycle for the shape parameter and g_9 (γ_3, γ_4) the semiannual cycle for the shape parameter.

The best combination of annual and semiannual cycles for the location, the scale and the shape parameters is obtained by using the likelihood ratio test with a significance higher than 95 % (Coles, 2001) . By an iterative procedure at each step is added a new gene, g, and evaluated the log-likelihood value, which is then compared with the previous one using the likelihood ratio test. For example, for the Catania buoy, initial model has c=[000.000.0.00], and the optimal model is defined by c=[101.000.1.00]. This codification explain a extreme value model with the parameters: $\{\beta_{0,}\beta_1, \beta_2, \beta_5, \beta_6, \alpha_0, \gamma_0\}$.

3. Assessment of wave heights associated to a given return period.

The evaluation of time varying parameters allows calculating the "effective" time varying design value quantiles (Menéndez et al., 2008b) using the following expression:

$$z_q(t,\theta) = z_q(\mu(t), \psi(t), \xi(t)) = \begin{cases} \mu(t) - \frac{\psi(t)}{\xi(t)} \left[1 - \{-\log(1-q)\}^{-\xi(t)}\right], \xi(t) \neq 0 \\ \mu(t) - \psi(t) \log\{-\log(1-q)\}, \quad \xi(t) = 0 \end{cases} \tag{3.4}$$

where probability q is given by F(z)=1-q and the quantile estimate z_q (t,θ) is the time-dependent return level associated with the return period 1/q. Therefore, the quantity varies depending on the time of the year (Méndez et al., 2007). Confidence intervals can be obtained by the delta method (Rice, 1994), assuming approximate normality for the maximum likelihood estimators. Because of the time-dependent parameters of the distribution, the calculation of extreme Hs return values for a given period, for instance one year, $\overline{z_q}[t_1,t_2]$, requires a more complex approach (Menéndez et al., 2009).

$$1 - q = \exp\left\{ -\int_{t_1}^{t_2} \left[1 + \xi(t)\left(\frac{\overline{z_q}[t_1,t_2] - \mu(t)}{\psi(t)}\right)\right]_+^{-1/\xi(t)} \right\} \tag{3.5}$$

Where 1-q is the probability associated with the return period 1/q. In order to asses these quantiles, as function of a given Tr, a correction of the value of Tr is necessary, using the GPD distribution. The annual maxima method considers just one event per year, while the POT method allows to select more than one event per year, so the corrected return period, Tr*, could be evaluated as:

$$Tr^* = Tr\nu$$

Where ν is the ratio between the number of the peak over threshold and the number of recording years, and represents the mean number of recorded events per year. For the same reason to represent in the quantile plot the empirical quantiles, these must be associated to scaled empirical return periods as:

$$Tr_{emp} = Tr_{emp}/\nu$$

4. Calculation of the confidence intervals of the extreme Hs return values.

The confidence intervals of a certain wave height associated to a return period have been computed using the Delta method (Rice, 1994). Let consider g(Θ) as $\overline{z_q}$ (the wave height associated to a return period). Therefore $\overline{z_q}$ is a function of μ(t), ψ(t), ξ(t), and the vector parameter could be Θ= $\{\beta_0\beta_1...\beta_n\alpha_0\alpha_1...\alpha_n\gamma_0\gamma_1...\gamma_n\}$.

The variance of g(Θ) is :

$$Var\left[g(\Theta)\right] = \left(\frac{\partial g(\hat{\Theta})}{\partial \Theta_i}\right)^T \cdot J_{ij}(\Theta) \cdot \left(\frac{\partial g(\hat{\Theta})}{\partial \Theta_i}\right)$$

Where J_{ij} is the variance-covariance matrix. The standard error of the function $g(\Theta)$ is

$$se\left[g(\Theta)\right] = \left(\sum_{i=1}^{p}\sum_{j=1}^{p}\frac{\partial g(\hat{\Theta})}{\partial \theta\Theta}\frac{\partial g(\hat{\Theta})}{\partial \Theta j}J_{i,j}^{-1}\right)$$

And the 95% confidence intervals of $g(\Theta)$ is estimated as:

$$g(\Theta) = \pm 1.96 se(g(\Theta))$$

3.4.3 Results

The results for the data between 1989-2001

The results here presented have been obtained considering the same threshold of the Atlas (second column of Table 3.4) for selection of the exceedances in order to better compare the results of the two studies. In this case, a stationary model has been imposed with the parameters: β_0, α_0 and γ_0. Therefore, the GPD-Poisson model in stationary mode has been used (θ is [0 0 0 0 0 0 1 0 0]).

Table 3.4: the POT threshold and the ξ parameter.

BUOY	Threshold(m)	ξ
Alghero	6.0	- 0.324
Catania	3.0	-0.390
Crotone	4.0	-0.400
La Spezia	4.0	-0.223
Mazara del Vallo	3.5	-0.182
Monopoli	3.0	-0.231
Ortona	3.0	-0.259
Ponza	3.5	-0.066

Figure 3.8 shows the expected Hs for different Tr for several buoys, the ones with the largest data record. Red dots represent empirical data, solid black line the resulting statistical distribution and the dashed lines the 95% confidence intervals. It could be noticed that the distribution tail behavior is similar at all the buoys. It has been found for all of them a negative ξ as shown in the second column of Table 3.4. The values are almost similar and evidence a clear Weibull behaviour (bounded upper tail of the distribution), except at Ponza, where can be observed a lower value of ξ, so a behaviour that tends to the Gumbel one.

The Table 3.5 shows in the first two columns a comparison at each buoy ot the Hs for a return period of 50 years and the relative 95% confidence intervals contained in the Atlas and obtained with this new analysis. Note that the assessed quantiles using new analysis are a bit lower although quite similar, and tha the confidence intervals are wider and cover the resulting values of the Atlas.

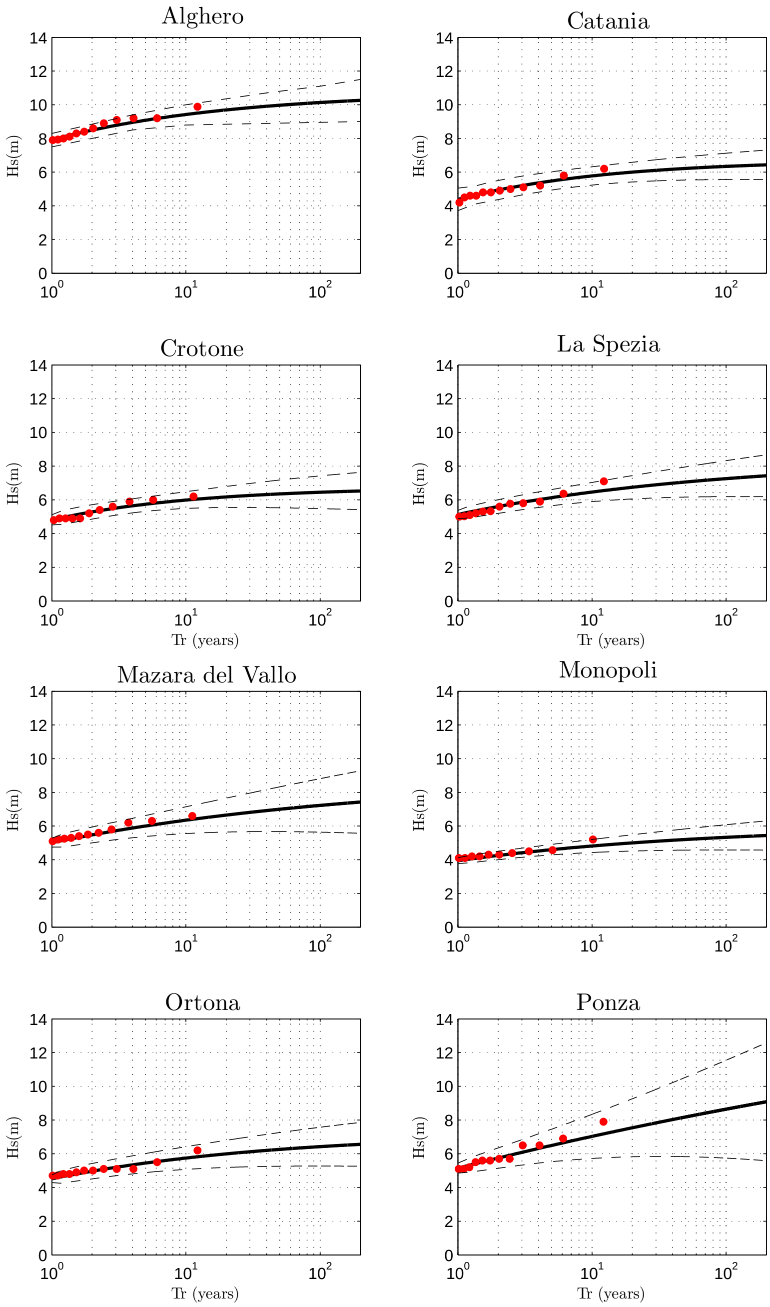

Figure 3.8: Observed (red dots) and estimated (solid black line) return level plots using the GPD-Poisson model in stationary mode. Dashed black lines represents the 95% confidence intervals.

The results for data from 1989 to 2008

The automatic model selection, considering time varying coefficients has been applied to all the data available between 1989 and 2008 at the same eight buoys. The threshold used and the number of events selected are listed in previous Table 3.3. Table 3.6 and 3.7 illustrate a summary of the final results for the time-dependent model of the studied buoys: final combination of parameters, θ, maximum likelihood estimates for the time-dependent location, scale and shape parameters (with standard errors), maximum log-likelihood function (l) and number of involved parameters (p). The standard errors of each parameter g_i has been evaluating defining the vector se[g] as:

$$se\,[g] = \sqrt{inv(\mathrm{J})}$$

where J is the inverse of the hessian matrix.

In general, as it could by observed in the vector θ the distribution for all the buoys are characterized by having an annual harmonic for the location parameter, while the shape parameter γ is different from zero for half of the buoys, indicating a Weibull behavior.
The time-dependent behavior within a year of the occurrence and magnitude of the extreme events are shown in the figures 3.9 to 3.12. Figure 3.9 shows sample results at Alghero (upper panel) and Catania (lower panel) buoys from the model in terms of frequency (fig.3.9(left)) and magnitude (fig.3.9(right)). On the left side of the figure are represented the empirical distribution of the rate of occurrence of threshold excesses (bars) and time-dependent event rate modeled within a year (solid line), that is the λ Pareto-Poisson parameter scaled in order to have the same area of the bars. On the right the exceedances over the threshold are represented with crosses, the instantaneous 20-year quantile, $\mathrm{Hs}_{Tr}(\mathrm{t})$, is plotted with a black solid line. In this figure the integrated 20 year annual quantile return level from the non-stationary model ($\overline{z_q}$) is also plotted (black dashed line). Analyzing the results reported from Figures 3.9 to 3.12 show that the time-dependent parameters are able to model the data variability throughout a year, in contrast to the stationary POT model.
It must be underlined that the instantaneous quantile plots are useful to describe the no stationary behaviour of the model and that these quantiles can not by compared with the classical engineering quantile evaluated with a stationary model. For that reason, in order to make a comparison with the stationary quantile, the representation in the same plots of the integrated 20 year annual quantile return levels has been carried out. The estimation of

the 20 year annual quantile return levels could be considered more detailed and accurate that the stationary one, since it firstly models the seasonality (improving the significance of the parameters involved and reducing the residuals) and subsequently, integrates the modeled variability within a year.

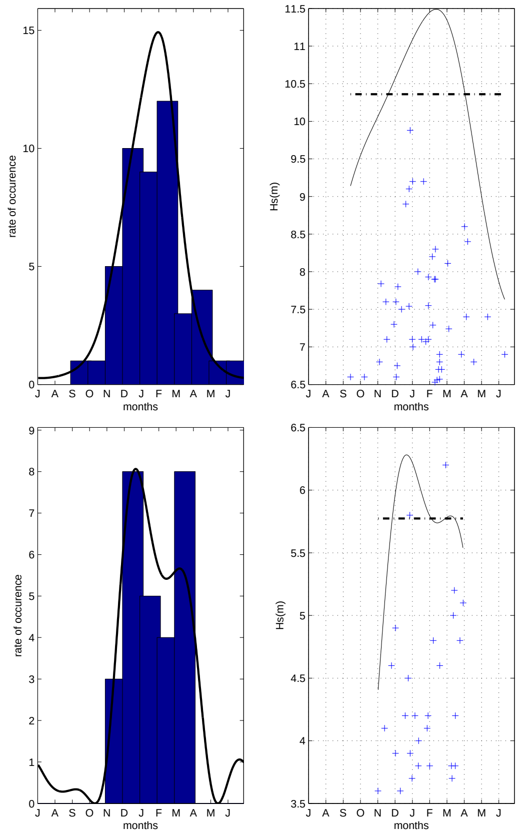

Figure 3.9: (left) Empirical distribution of the rate of occurrence of threshold excesses (bars) and time-dependent event rate modeled within a year (solid line) for Alghero buoy(upper panel) and Catania buoy (lower panel). (right) Exceedances over the threshold (crosses), instantaneous 20-year quantile (black solid line), and the annual extreme significant wave height 20 year return value (black dashed line).

It can be observed that the buoys of the western coast, as Alghero and Mazara del Vallo, are characterized by extreme Hs also during spring season,

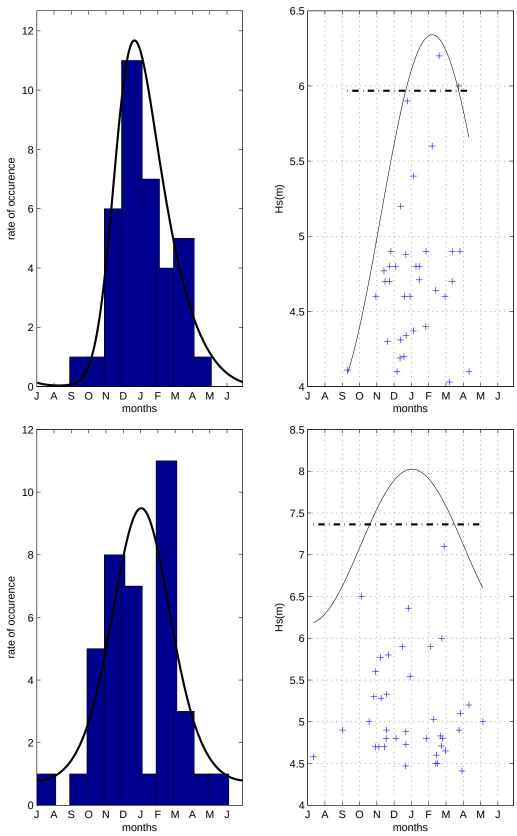

Figure 3.10: (left) Empirical distribution of the rate of occurrence of threshold excesses (bars) and time-dependent event rate modeled within a year (solid line) for Crotone buoy (upper panel) and La Spezia buoy (lower panel). (right) Exceedances over the threshold (crosses), instantaneous 20-year quantile (black solid line), and the annual extreme significant wave height 20 year return value (black dashed line).

except the buoys of La Spezia and Ponza, where extreme waves in autumn have also been recorded.
Figure 3.13 shows the return level plots for all the considered buoys using the GPD-Poisson model in no-stationary mode and the 95% confidence intervals. The return levels here plotted have been obtained as the annual integrated quantiles, $\overline{z_q}[t_1,t_2]$ considering the probability 1-q, associated to each return period Tr. In general it can be observed a good agreement between the

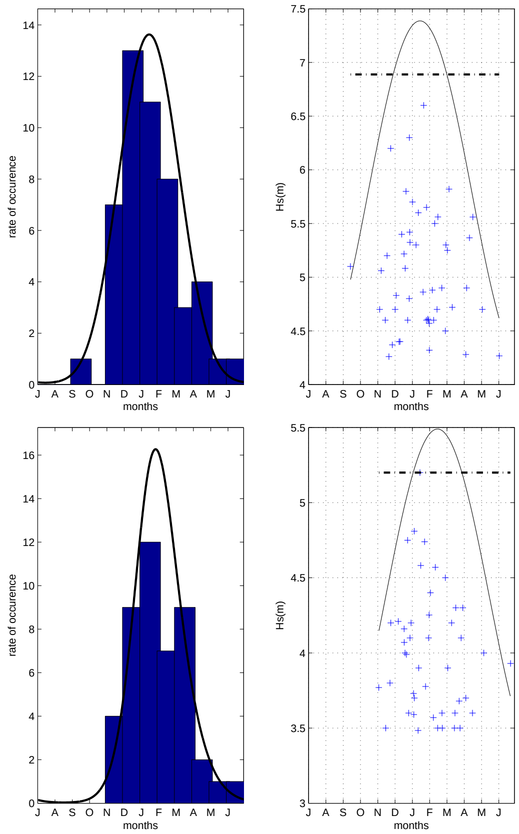

Figure 3.11: (left) Empirical distribution of the rate of occurrence of threshold excesses (bars) and time-dependent event rate modeled within a year (solid line) for Mazara del Vallo buoy (upper panel) and Monopoli buoy (lower panel). (right) Exceedances over the threshold (crosses), instantaneous 20-year quantile (black solid line), and the annual extreme significant wave height 20 year return value (black dashed line).

data and the model. Different distribution tail behaviours have been found, in fact the Gumbel distribution has been obtained for the data collected at the buoys of La Spezia, Ortona and Ponza. The empirical values of Hs are contained in the confidence intervals. It could also be observed an overestimation at Ortona buoy; this could be related to the selected data that do not represent adequately the annual scale. Moreover it must be noticed that the highest waves recorded in Ponza occurred in December

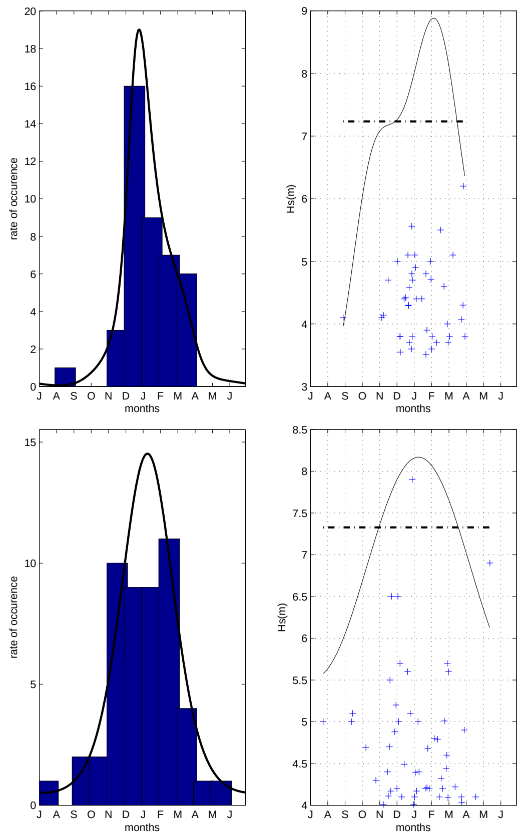

Figure 3.12: (left) Empirical distribution of the rate of occurrence of threshold excesses (bars) and time-dependent event rate modeled within a year (solid line) for Ortona buoy (upper panel) and Ponza buoy (lower panel). (right) Exceedances over the threshold (crosses), instantaneous 20-year quantile (black solid line), and the annual extreme significant wave height 20 year return value (black dashed line).

1999, when a very exceptional storm was registered (Arseni et al., 2001). It could also be observed that at Ponza and Mazara del Vallo buoys confidence intervals are narrower than the ones of the stationary model, although the higher number of parameters, four instead of three for Ponza and five instead of three at Mazara del Vallo.

The Table 3.5 summarizes the Hs for a return period of 50 years and the relative 95% confidence intervals contained in the Atlas and obtained

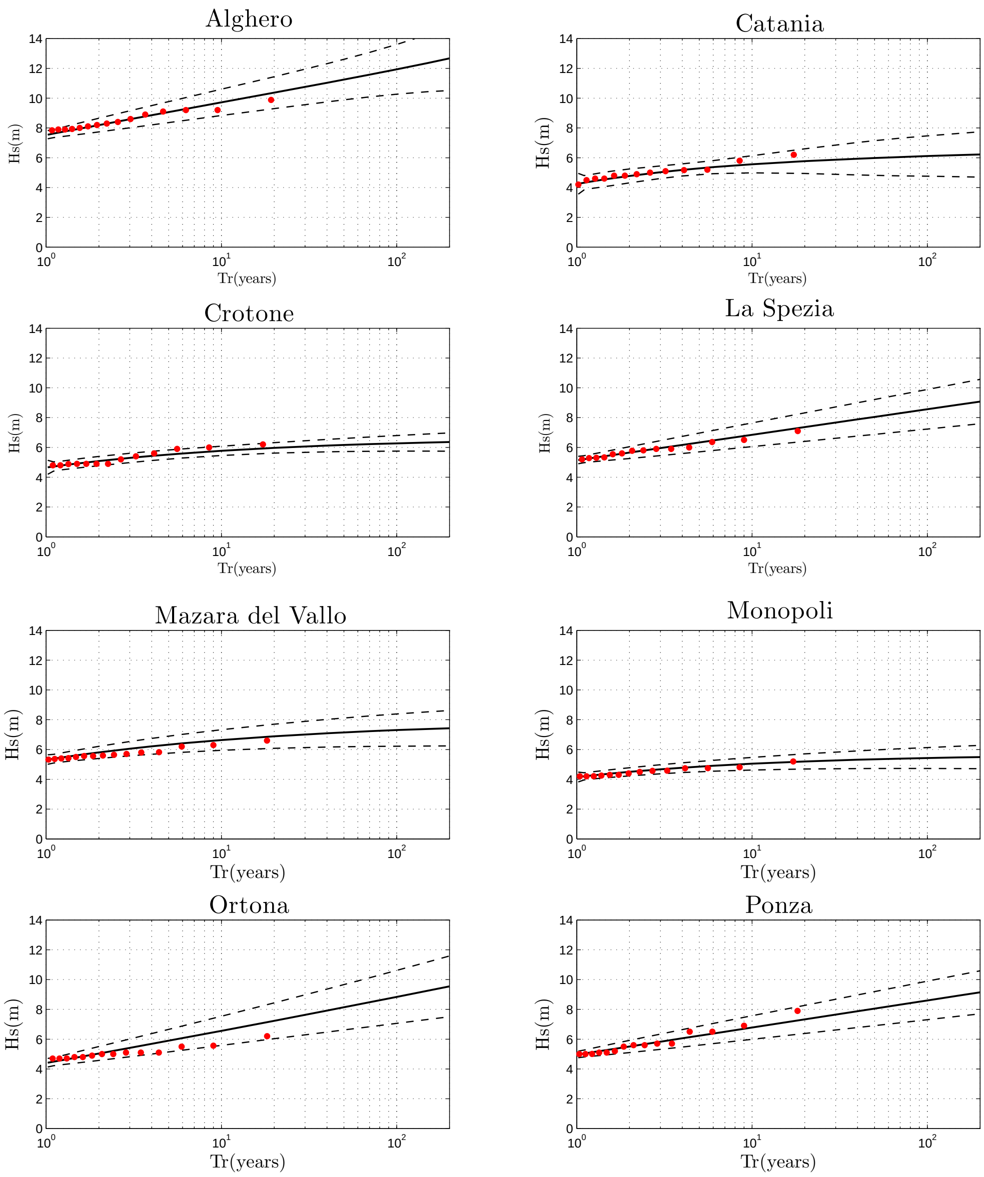

Figure 3.13: Observed (red dots) , estimated return level plots using the GPD-Poisson model in no-stationary mode (solid bold line). black lines represents the 95% confidence intervals.

considering the data until 2001, using the stationary model, and considering the data until 2008, using the time varying model. It can be noted that, comparing the results of the stationary model and the ones obtainded with the time varying model on the data collected until 2008 the results are quite similar, although there are some differences at Ortona, where the Hs for a return period of 50 years obtained with the time varying model is outside the confidence intervals of the stationary model. Looking to the confidence intervals it is not possible to relate directly the number of parameters the their amplitude, in fact while at Alghero, where 6 parameters have been selected for the time varying distribution instead of thre, the interval is wider than in the stationary model, while at Crotone, where 7 parameters have been selected, the confidence interval is narrower.

Table 3.5: Hs for a 50 years return period and the corresponding values of 95% confidence intervals obtained in the Atlas, from the stazionary analysis on the data until 2001 and from the time varying model applied on the data until 2008.

BUOY	Hs_{50}Atlas(c.i)(m)	Hs_{50}staz.m.(c.i)(m)	Hs_{50} t.var. m.(c.i)(m)
Alghero	10.8 (10 - 11.5)	10.0 (9.0 - 10.9)	11.25 (9.89 - 12.61)
Catania	6.9 (6 - 7.5)	6.2 (5.5 - 6.9)	5.98 (4.82 - 7.15)
Crotone	6.7 (6- 7.3)	6.3 (5.5 -7.2)	6.16 (5.72 -6.60)
La Spezia	7.8 (6.4 - 7.8)	7.1 (6.2 - 8)	8.05 (6.88 - 9.22)
Mazara del V.	7.4 (6.8 - 8)	7 (5.7 - 8.3)	7.15 (6.18-8.12)
Monopoli	5.8 (5 - 6)	5.2 (4.6 - 5.8)	5.35 (4.73-5.97)
Ortona	6.6 (5.8 - 7.2)	6.3 (5.3 -7.3)	8.14 (6.62-9.66)
Ponza	8.6 (7.5 - 9.5)	8.2 (5.8 - 10.5)	8.05 (6.91-9.19)

To better understand the usefulness of the time varying model for Alghero has been evaluated the integrated quantile per each month, as shown in the Figure 3.14. There it is possible to observe both the annual and the monthly quantiles and evaluate the extreme events that could be expected during each month, and so, for example use this results to establish working time windows for maritime works or properly decide a design wave for structure used just in the calm season.

Figure 3.13 shows the spatial distribution of the location, scale and shape parameters and the significant wave height 20 year return values integrated for an year. From this figure it is possible to obtain some useful information in order to geographically characterize extreme Hs. The spatial

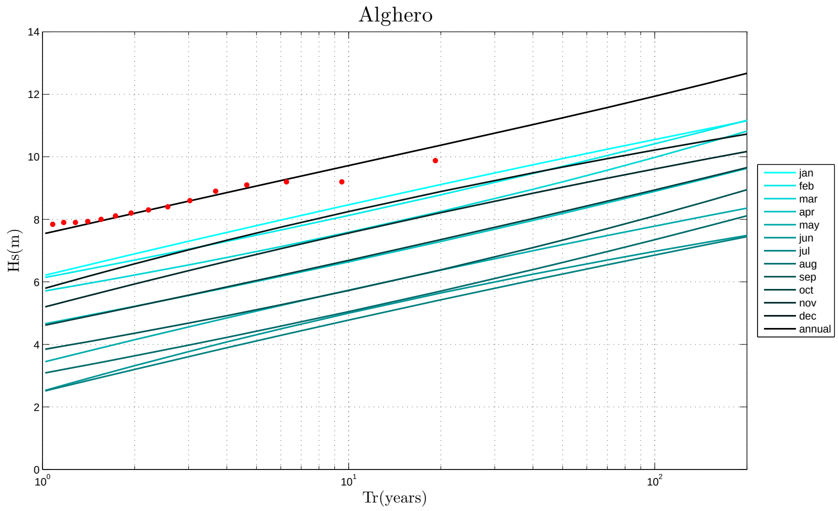

Figure 3.14: Monthly and annual return level plots for Alghero buoy.

distribution of the location parameter, β_0, indicates that the western coasts are characterized by higher values of this parameter and so by greater extreme Hs. The scale parameter, α_0, shows an higher dispersion on the northern coasts and in the Tyrrhenian Sea. The shape parameter,γ_0, assumes values different from zero for South Italy, indicating up bounded conditions. Last panel of figure 3.13 shows that Alghero has the highest probability for extreme events and that the western and northern Italian coasts are in general characterizer by higher extreme events than the southern coast. The last three panels show also that the two buoys of the Adriatic Sea, Ortona and Monopoli, are characterized by evident different behaviors.

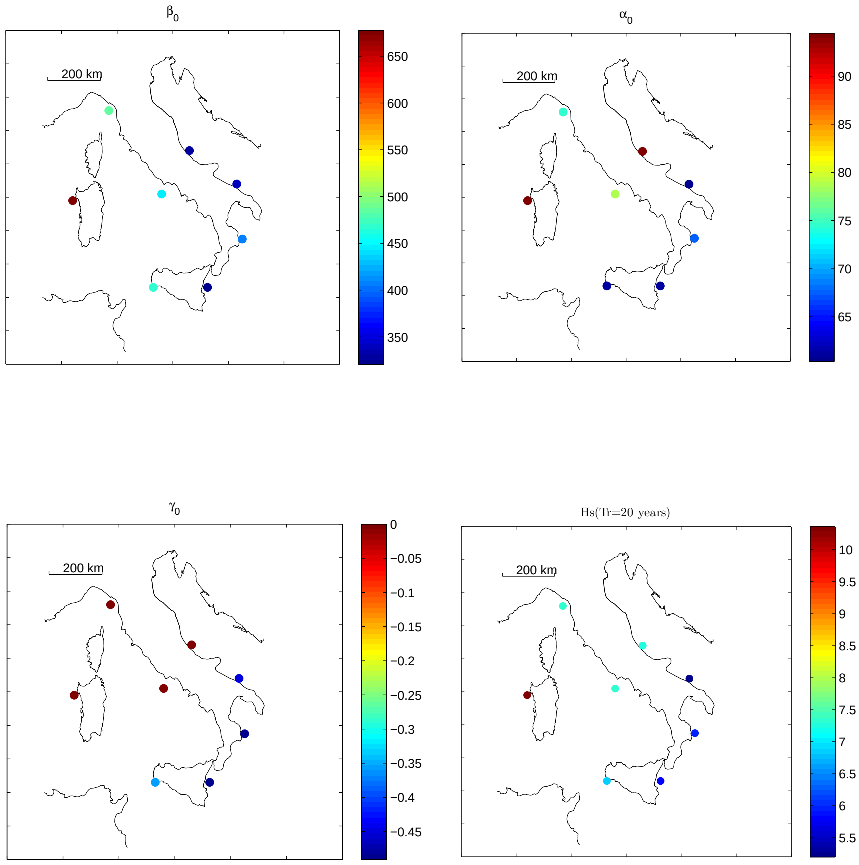

Figure 3.15: Spatial distribution of the location, scale and shape parameters and the extreme significant wave height 20 year return values integrated for an year.

Table 3.6: Summary of the final results for the time-dependent model for the studied buoys: final θ, maximum likelihood estimates for the location, scale and shape parameters (with standard errors), maximum log-likelihood function (l) and number of involved parameters (p).

BUOY	Alghero	Catania	Crotone	La Spezia
θ	100;000;0;01	101;000;1;00	100;100;1;00	100;000;0;00
β_0(cm)	677.6	320.8	405.5	487.4
se(β_0)	(25.3)	(45.4)	(24.8)	(17.8)
β_1(cm)	181.3	196.6	136.8	92.4
se(β_1)	(42.0)	(58.6)	(30.4)	(25.5)
β_2(cm)	43.9	81.7	36.4	2.0
se(β_2)	(28.0)	(25.5)	(19.2)	(18.1)
β_3(cm)				
β_4(cm)				
β_5(cm)		8.0		
se(β_5)		(22.5)		
β_6(cm)	-48.9			
se(β_6)		(32.7)		
α_0(cm)	94.1	61.4	67.5	74.3
se(α_0)	(13.8)	(15.6)	(19.2)	(11.9)
α_1(cm)			-24.0	
se(α_1)			(27.1)	
α_2(cm)			22.8	
se(α_2)			(11.2)	
α_3(cm)				
α_4(cm)				
α_5(cm)				
α_6(cm)				
γ_0(cm)		-0.49	-0.49	
se(γ_0)		(0.33)	(0.22)	
γ_1(cm)				
γ_2(cm)				
γ_3(cm)	-0.08			
se(γ_3)	(0.1)			
γ_4(cm)	0.07			
se(γ_4)	(0.1)			
l	-237.9	-137.69	-169.1226	-196.63
p	6	7	7	4

Table 3.7: Summary of the final results for the time-dependent model for the studied buoys: final θ, maximum likelihood estimates for the location, scale and shape parameters (with standard errors), maximum log-likelihood function (l) and number of involved parameters (p).

BUOY	Mazara del Vallo	Monopoli	Ortona	Ponza
θ	100;000;1;00	100;100;1;00	100;001;0;00	100;000;0;00
β_0(cm)	466.8	338.1	329.2	448.7
se(β_0)	(17.8)	(23.6)	(37.1)	(19.3)
β_1(cm)	155.5	122.4	224.2	130.6
se(β_1)	(33.6)	(28.5)	(55.5)	(29.7)
β_2(cm)	36.7	84.5	59.8	17.0
se(β_2)	(19.1)	(23.8)	(31.1)	(18.0)
β_3(cm)				
β_4(cm)				
β_5(cm)				
β_6(cm)				
α_0(cm)	61.2	60.35	94.5	78.9
se(α_0)	(10.7)	(14.9)	(15.7)	(11.2)
α_1(cm)		-25.3		
se(α_1)		(18.4)		
α_2(cm)		-4.5		
se(α_2)		(14.0)		
α_3(cm)				
α_4(cm)				
α_5(cm)			-11.8	
se(α_5)			(10.5)	
α_6			(cm) 16.9	
se(α_6)			(10.7)	
γ_0(cm)	-0.36	-0.45		
se(γ_0)	(0.12)	(0.17)		
γ_1(cm)				
γ_2(cm)				
γ_3(cm)				
γ_4(cm)				
l	-228.37	-196.80	-198.7961	-236.3164
p	5	7	6	4

3.5 Conclusions

In this section the extreme wave climate along the Italian coast has been analyzed using the data collected by the RON and two different statistical analysis.
Firstly the seasonal variability of extreme events along the Italian coast has been analyzed, showing an evident seasonal pattern of larger Hs in winter season and lower in summertime for all the locations, except for the Ligurian Sea buoy where the differences between winter and summer are smaller. A similar behavior but less evident has been found in the central Tyrrenian Sea. This has been related to the presence in the Gulf of Genoa of cyclones during all year.
The two statistical analysis presented in this work, have been applied on the data collected by eight RON buoys on different time intervals and a POT method has been used in both cases to select extreme values. This method allows to focus on the modeling of the intensity of a physical phenomena as sea storm waves.
The first statistical analysis has been carried out on the data collected from 1989 to 2001 using a stationary GPD-Poisson model. The obtained results have been compared with the results of the Italian Atlas, giving similar extreme value distribution and so similar Hs(Tr).
Then the second analysis has been applied on the data collected between 1989 and 2008 and it has tried to understand and model the intra-annual variability, using a more complex approach. In particular the inclusion in the model of time dependent parameters that represent location, scale and shape parameters of the GPD-Poisson distribution, such as sine waves to model seasonality, has improved the goodness of the model fit to the data and also allows to characterize extreme events that could occur within a year.
The results obtained in this work show that the seasonality of the extreme wave height events is variable and depends on the local wave climate. The comparison between the results and the recorded data, indicates that in general the introduction of seasonal variability could improve the shape of the statistical distributions, as for instance could be observed at the buoys of Alghero, La Spezia and Ponza.
The inclusion of seasonality leads to more reliable designs of maritime works, due to the facts that the model allows a better explanation of the variability of extreme significant wave height throughout a year. This could also be very useful, for instance, to define a working windows for maritime works.
The spatial variability of the obtained parameters of the distribution has also

been observed, allowing to distinguish different extreme waves behaviours between easter and western Seas. In particular it has been shown that Alghero has the highest probability for extreme events and that the western and northern Italian coasts are in general characterized by higher extreme events than the southern coast. Other efforts can be carried out to model also the inter-annual variability and to understand which are the patterns that most influence the Italian wave climate.

Chapter 4

Conclusions

In this thesis two different coastal extreme events, landslide generated tsunamis and extreme sea waves, have been studied using different tools. The two subjects treated in this work have analyzed the hazard of an extreme event with, fortunately, a small occurrence probability, and the probability of occurrence of more frequent and dangerous events, extreme sea waves.
The fully 3D numerical model, Flow-3D has allowed to model and analyze landslide generated tsunamis and a statistical analysis has allow to study the extreme wave climate variability around the Italian coasts.
The conclusions for each topic have been exposed respectively in the paragraphs 2.6 and 3.5. As a general conclusion it can be said that the numerical model Flow-3D has shown its robustness and accuracy, allowing to consider the model as a useful tool to study fluid-structure interaction and especially landslide generated tsunamis. The model, with its reasonable computational costs, can provide precomputed inundation maps and give information on the parameters that most influence the propagation in the near and far field of landslide generated tsunami. It is reasonable to think at the model as a tool in a Early Warning System for tsunami events.
The statistical analysis and in particular the no-stationary GPD-Poisson model has allowed to study the intra-annual variability of the extreme wave climate around the Italian coast and to characterize the spatial distribution of extreme events. Different behaviours have been observed, identifying a clear distinction between eastern and western Seas. It can also be underlined the utility of the model in the field of maritime engineering to define working windows and to define design waves for seasonal structures.

Bibliography

[1] Abadie S., Morichon D., Grilli S., Glockner S. (2008a). VOF/Navier-STokes numerical modeling of surface waves generated by subaerial landslides. *La Houille Blanche* 1,pp. 21-26

[2] Alcamo J., Moreno J.M., Nováky B., Bindi M., Corobov R., Devoy R.J.N., Giannakopoulos C., Martin E., Olesen J.E., Shvidenko A. (2007). Europe. Climate change 2007: impacts, adaptation and vulnerability. In: Parry, M.L., Canziani, O.F., Palutikof, J.P., van der Linden, P.J., Hanson, C.E. (Eds.), Contribution of Working Group II to the Fourth Assessment Report of the Intergovernmental Panel on Climate Change. *Cambridge University Press*, pp. 541-580

[3] Arseni A., Corsini S., Franco L., Inghilesi R. (2001). Analisi della tempesta del 28-29 dicembre 1999 nei mari occidentali italiani. *Convegno AIPCN, Salerno*

[4] Assier Rzadkiewicz S., Mariotti C., Heinrich P. (1997). Numerical Simulation of Submarine Landslides and their hydraulic effects. *Journal of Waterways, Port, Coastal and Ocean Engineering* 123(4), pp. 149-157

[5] Ataie-Ashtiani B., Nik-Khah A. (2008a). Impulse waves caused by subaerial landslides. *Environmental Fluid Mechanics* 8(3), pp. 263-280

[6] Ataie-Ashtiani B., Nik-Khah A. (2008b). Laboratory investigations on impulsive waves caused by underwater landslide. *Coastal Engineering* 55(12), pp. 989-1004, doi: 10.1016/j.coastaleng.2008.03.003

[7] Bellotti G., Cecioni C., De Girolamo P. (2008). Simulation of small-amplitude frequency-dispersive transient waves by means of the mild-slope equation. *Coastal Engineering* 55, pp. 447-458

[8] Bertotti L., Cavaleri L., De Girolamo P., Franco L., MAgnaldi S. (2008). Hindcast and forecast of he Parsifal storm. *Il nuovo Cimento* 21C-3, pp. 281-298

[9] Billi A., Funiciello R., Minelli L., Faccenna C., Neri G., Orecchio B., Presti D. (2008). On the cause of the 1908 Messina tsunami, southern Italy. *Geophysical Research Letters* 35, L06301

[10] Brocchini M., Bernetti R., Mancinelli A., Albertini G. (2001). An efficient solver for nearshore flows based on the WAF method. *Coastal Engineering* 43, pp. 105-129

[11] Carter D. J.T., Challenor P.G. (1981). Estimating return values of environmental variables. *Quart. J. Roy. Meteor. Soc.* 107, pp. 259-266

[12] Cecioni C.(2010). Numerical modeling of waves for a tsunami early warning system. *Ph.D. Thesis. University of Roma Tre*

[13] Choi B.H., Kim D.C., Pelinovsky E. and Woo S.B. (2007). Three dimensional simulation of tsunami run-up around conical island. *Coastal Engineering* 54,374 pp. 618-629

[14] Choi B.H., Pelinovsky E., Kim D.C., Didenkulova I. and Woo S.B. (2008). Two- and three-dimensional computation of solitary wave runup on non-plane beach. *Nonlinear Processes in Geophysics* 15, pp. 489-502

[15] Chopakatla S.C., Lippmann T.C. and Richardson J.E. (2008). Field verification of a computational fluid dynamics model for wave transformation and breaking in the surf zone. *Journal of Waterway, Port, Coastal, and Ocean Engineering* 134(2), pp. 71-80

[16] Coles S. G. (2001). An introduction to statistical modeling of extreme values. *London: Springer*

[17] Dawson T. H. (2000). Maximum Wave Crests in Heavy Seas. *J. Offshore Mech. Arct. Eng.* 122(3),pp. 222

[18] Di Risio, M. (2005). Landslide generated impulsive waves: Generation, propagation and interaction with plane slopes. *Ph.D. Thesis. University of Roma Tre*

[19] Di Risio M., De Girolamo P., Bellotti G., Panizzo A., Aristodemo F., Molfetta M.G. and Petrillo A.F. (2009a). Landslide generated tsunamis runup at the coast of a conical island: New physical model experiments. *Journal of Geophysical Research* 114, C01009

[20] Di Risio M., Bellotti G., Panizzo A. and De Girolamo P. (2009b). Three-dimensional experiments on landslide generated waves at a sloping coast. *Coastal Engineering* 56 , pp. 659-671

[21] Di Risio M., De Girolamo P., Beltrami G.M., (2011). Forecasting Landslide Generated Tsunamis: a Review, The Tsunami Threat - Research and Technology, *Nils-Axel Mörner (Ed.)*, ISBN: 978-953-307-552-5, InTech.

[22] Enet F., Grilli S.T. (2007). Experimental study of tsunami generation by three-dimensional rigid underwater landslides. *Journal Waterway, Port, Coastal, and Ocean Engineering, ASCE* 133(6), pp. 442-454

[23] Fisher R. A., Tippett L.H.C. (1928). Limiting forms of the frequency distribution of the largest or smallest member of a sample. *Procs. Cambridge Philos. Soc.* 24, pp.180-190

[24] Fleming J.G., Walters R.A., Sue L.P., Nokes R.I. (2005). Experimental design for solid block and granular submarine landslides: a unified approach. *Tsunamis: case studies and Recent Developments, Springer, K. Satake (ed.)*, pp. 259-277, doi: 10.1007/1-4020- 3331-1 16

[25] Flow Science Inc (2007) FLOW-3D User's Manual

[26] Franco L., Contini P. (1997). Wave measurements and climatology in the Italian Seas. *PIANC Bulletin* 94, pp.67-76, Bruxelles

[27] Franco L., Piscopia R., Corsini S., Inghilesi R.(2004). L'Atlante delle onde nei mari italiani - Italian Wave Atlas, Full Final Report. *APAT-University of Roma Tre, sponsored by AIPCN Italian Section and Italia Navigando*, Roma

[28] Fréchet, M. (1927). Sur la loi de probabilité de l'écart maximum, *Ann. Soc. Polon. Math. Cracovie* 6, pp. 93-116

[29] Fritz H.M. , Hager W.H. , Minor H.E. (2001). Lituya Bay case: rockslide impact and wave run-up. *Sci. Tsunami Hazard* 19, pp. 3-21

[30] Fritz H.M. , Hager W.H., Minor H.E. (2004). Near field characteristics of landslide generated impulse waves. *Journal Waterway, Port, Coastal, and Ocean Engineering, ASCE* 130(6), pp. 287-302

[31] Fritz H.M., Mohammed F., Yoo J. (2009). Lituya Bay Landslide Impact Generated Mega-Tsunami 50th Anniversary. *Pure and Applied Geophysics* 166, pp. 153-175

[32] Galambos, J. (1987). The Asymptotic Theory of Extreme Order Statistics, Robert E. Krieger. *Malabar, Florida. 2nd ed.*

[33] GEO-3 2002 Global Environment Outlook 3. Past, present and future perspectives. Natural disasters. See http://www.grida.no/publications/other/geo3/?src=/geo/geo3/

[34] Gnedenko B. (1943) Sur la distribution limite du terme maximum d'une série aléatoire. Translated and reprinted in *Breakthroughs in Statistics* I, 1992, Springer-Verlag, pp. 195-225

[35] Goda Y.(1988). On the methodology of selecting design wave height. *ICCE'88*, Malaga

[36] Grilli S.T., Watts P. (2005). Tsunami generation by submarine mass failure. I: modeling, experimental validation, and sensitivity analyses. *Journal of Waterway, Port, Coastal, Ocean Engineering* 131(6), pp. 283-297

[37] Gumbel, E. J. (1958) Statistics of Extremes. *Columbia University Press*

[38] Hawkes P.J., Gonzalez-Marco D., Sánchez-Arcilla A.,Prinos P. (2008). Best practice for the estimation of extremes: A review. *Journal of Hydraulic Research* 46:2, pp. 324-332

[39] Harris R.I.(2001). The accuracy of design values predicted from extreme value analysis. *Journal of Wind Engineering and Industrial Aerodynamics* 89-2, pp. 153-164(12)

[40] Heinirich P.H. (1992). Non linear water waves generated by submarine and aerial landslides. *Journal of Waterways, Port, Coastal and Ocean Engineering* 118, 249

[41] Hirt C.W. and Nichols B.D. (1981) Volume of fluid (VOF) method for the dynamics of free boundaries. *Journal of Computational Physics* 39, pp. 201-225

[42] Huber A. and Hager W.K. (1997). Forecasting impulsive waves in reservoirs. In *Commission internationale des grands barrages, Dix-neuvieme Congres des Grands Barrages*, Florence, Italy, pp. 993-1005

[43] Katz R. W., Parlange M. B., Naveau P. (2002). Statistics of extremes in hydrology. *Adv. in Water Resour.* 25,pp. 1287-1304

[44] Keasavan P.C. and Swaminathan M.S. (2006). Managing extreme natural disasters in coastal areas. *Phil. Trans. R. Soc. A* 364, pp. 2191-2216

[45] Kotz, S. y Nadarajah, S. (2000) Extreme Value Distributions: Theory and Applications. *Imperial College Press, London*

[46] Koutsoyannis D. (2004).Statistics of extremes and estimation of extreme rainfall: I. Theoretical investigation. *Hydrological Sciences-Journal-des Sciences Hydrologiques* 49(4)

[47] Lionello P., Sanna A. (2005). Mediterranean wave climate variability and its links with NAO and Indian Monsoon. *Clim.Dyn.* 25, pp. 611-623

[48] Lionello P., Bhend J., Buzzi A., Della-Marta P.M., Krichak S., Jansà A., Maheras P., Sanna A., Trigo I.F., Trigo R. (2006). Cyclones in the Mediterranean region: climatology and effects on the environment. *Mediterranean Climate Variability. Elsevier (NETHERLANDS)*, Amsterdam, pp. 324-372

[49] - Lionello P., Cogo S. , Galati M.B., Sanna A. (2008). The Mediterranean surface wave climate inferred from future scenario simulations. *Global and Planetary Change* 63, pp. 152-162

[50] Liu P.L-F., Cho Y.S., Briggs M.J., Kano.glu U., Synolakis C.E. (1995). Run-up of solitary waves on a circular island, *Journal of Fluid Mechanics*, 302, pp. 259-185

[51] Liu P.L-F, Wu T-R, Raichlen F., Synolakis C.E. and Borrero J.C. (2005). Runup and rundown generated by three-dimensional sliding masses. *The Journal of Fluid Mechanics* 536, pp. 107-144

[52] Lopatoukhin L.J., Rozhkov V.A., Ryabinin V.E., Swail V.R., Boukhanovsky A.V.,Degtyarev A. B. (2000). Estimation of extreme wind waves heights.WORLD METEOROLOGICAL ORGANIZATION *World Meteorological Organization*, JCOMM Technical Report 9

[53] Lynett P., Liu P.L-F. (2002). A numerical study of submarine-landslide-generated waves and run-up. *Proc. The royal Society London* 458, pp. 2885-2910

[54] Lynett P., Liu P.L-F. (2005) A numerical study of the run-up generated by three-dimensional landslides, *Journal of Geophysical Research* 110, C03006, doi:10.1029/2004JC002443

[55] Madsen P.A., Murray R., Sorensen O.R. (1991). A new form of boussinesq equations with improved dispersion characteristics. *Coastal Engineering* 15, pp. 371-388

[56] Martinelli L., Zanuttigh B., Corbau C. (2010). Assessment of coastal flooding hazard along the Emilia Romagna littoral, IT, *Coastal Engineering* 57, pp. 1042-1058

[57] Méndez F. J., Menéndez M., Luceño A., Losada I. J.(2006). Estimation of the long-term variability of extreme significant wave height using a time-dependent Peak Over Threshold (POT) model. *J. Geophys. Res.* 111, C07024, doi:10.1029/2005JC003344

[58] Menéndez M. (2008). Metodología para el análisis estadístico no-estacionario de valores extremos de variables geofísicas. *Ph.D. Thesis. University of Cantabria*

[60] Menéndez M., Méndez F. J., Losada I. J., Graham N. E. (2008a). Variability of extreme wave heights in the northeast Pacific Ocean based on buoy measurements. *Geophys. Res. Lett.* 35, L22607, doi:10.1029/2008GL035394

[60] Menéndez M., Méndez F.J., Izaguirre C., Luceño A., Losada I.J. (2008b). The influence of seasonality on estimating return values of significant wave height. *Coast. Eng.*, doi: 10.1016j

[61] Miller D. J. (1960). Giant waves in Lituya Bay, Alaska. *Geological Survey Professional Paper* 354-C US Government Printing Offce, Washington DC

[62] Monaghan J.J., Kos A. (2000). Scott Russell's wave generator *Physics of Fluids* 12(3), pp. 622-630

[63] Morton I.D., Bowers J., Mould G.(1997). Estimating return period wave heights and wind speeds using a seasonal point process model, *Coastal Eng.* 31,pp. 305-326

[64] Nicholls R.J., Wong P.P., Burkett V.R., Codignotto J.O., Hay J.E., McLean R.F., Ragoonaden S., Woodroffe C.D.(2007). Coastal systems and low-lying areas. Climate change 2007: impacts, adaptation and vulnerability. In: Parry, M.L., Canziani, O.F., Palutikof, J.P., van der Linden, P.J., Hanson, C.E. (Eds.), Contribution of Working Group II to the Fourth Assessment Report of the Intergovernmental Panel on Climate Change. *Cambridge University Press*, pp. 315-356

[65] Nicholls, R.J., de la Vega-Leinert A.C. (2008). Implications of sea-level rise for Europe's coasts. *Journal of Coastal Research* 24 (2), pp. 285-442

[66] Noda E. (1970). Water waves generated by landslides. *Journal of Waterway, Harbours, and Coastal Engineering Division-ASCE* pp. 835-855

[67] Nwogu O. (1993). Alternative form of the boussinesq equations for nearshore wave propagation. *Journal of Waterway Port Coastal and Ocean Engineering-ASCE* 119, pp. 618-638

[68] Panizzo A., Bellotti G., De Girolamo P. (2001). Application of wavelet transform analysis to landslide generated waves. *Coastal Engineering* 44, pp. 321-338

[69] Panizzo A., De Girolamo P., Di Risio M., Maistri A., Petaccia A. (2005). Great landslide events in italian artificial reservoir. *Natural Hazards and Earth System Science* 5, pp. 733-740

[70] Peregrine D.H. (1967). Long waves on a beach. *Journal of Fluid Mechanics* 27, pp. 815-827

[71] Pickands J. (1975). Statistical inference using extreme order statistics. *Ann. Statist.* 3, pp. 119-131

[72] Piscopia R., Inghilesi R., Panizzo A., Corsini S., Franco L. (2002a). Analysis of 12-year wave measurements by the Italian wave network, *Proc. 28th ICCE Conference*, pp. 121-133, Cardiff

[73] Piscopia R., Corsini S., Inghilesi R., Franco L. (2002b). Misure strumentali di moto ondoso della Rete Ondametrica Nazionale: analisi statistica aggiornata degli eventi estremi, *Atti 28° Convegno Nazionale di Idraulica e Costruzioni Idrauliche*, Potenza, vol.IV, pp. 271-280, Ed.Bios-CNR-GNDCI

[74] Prins, J.E. (1958). Characteristics of waves generated by local disturbance. *Transactions, American Geophysical Union*, pp. 865-874

[75] Renzi E., Sammarco P. (2010). Landslide tsunamis propagating around a conical island. *Journal of Fluid Mechanics* 650, pp. 251-285

[76] Resnick S. I. (1987). Extreme values, Regular Variation and Point Processes. *Springer- Verlag*

[77] Rice, J. (1994). Mathematical Statistics and Data Analysis. *2nd ed. Duxbury*

[78] Rodi W. (1980). Turbulence models and their application in hydraulics: a state of the art review. The Netherlands, International Association for Hydraulic Research

[79] Sammarco P., Renzi E. (2008). Landslide tsunamis propagating along a plane beach. *Journal of Fluid Mechanics* 598, pp. 107-119

[80] Smith, R. L. (1985). Maximum likelihood estimation in a class of nonregular cases. *Biometrika* 72,pp. 67-90

[81] Smith, R. L. (2001). Environmental statistics, technical report. *Dep. of Stat.,Univ. of N. C., Chapel Hill*

[82] Guedes Soares C., Scotto M. (2001). Modelling uncertainty in long-term predictions of significant wave height. *Ocean Engineering* 28, pp.329-342

[83] Speranza A., Buzzi A., Trevisan A., Malguzzi, P. (1985). A theory of deep cyclogenesis in the lee of the Alps. Part I: modifications of baroclinic instability by localized topography. *J. Atmos. Sci.* 42, pp. 1521-1535.

[84] Synolakis C.E., Bardet J.P., Borrero J., Davies H., Okal E., Silver E., Sweet J., Tappin D. (2002). Slump origin of the 1998 Papua New Guinea tsunami. *Proceedings of the Royal Society of London* 458, pp. 763-789

[85] Tadepalli S., Synolakis C.E. (1994) The run-up of n-waves on sloping beach *Proceedings of the Royal Society of London* 445, pp. 99-112

[86] Thompson M. L., Reynolds J., Cox L. H., Guttorpa P., Sampsona P. D. (2001). A review of statistical methods for the meteorological adjustment of tropospheric ozone. *Atmospheric Environment* 35-3,pp. 617-630

[87] Tinti S., Bortolucci E., Chiavettieri C. (2001) Tsunami Excitation by Submarine Slides in Shallow-water Approximation. *Pure and Applied Geophysics* 158, pp. 759-797

[88] Tinti S., Manucci A., Pagnoni G., Armigliato A. and Zaniboni F. (2005). The 30 December 2002 landslide-induced tsunamis in Stromboli: sequence of the events reconstructed from the eyewitness accounts. *Natural Hazards and Earth System Sciences* 5(6), pp. 763-775

[89] Tinti S., Maramai A., Armigliato A., Graziani L., Manucci A., Pagnoni G., Zaniboni F. (2006a). Observations of physical effects from tsunamis of December 30, 2002 at Stromboli volcano, southern Italy. *Bulletin of Volcanology* 68(5), pp. 450-461

[90] Tinti S., Pagnoni G., Zaniboni F., (2006b). The landslides and tsunamis of the 30th of December 2002 in Stromboli analysed through numerical simulations. *Bulletin of Volcanology* 68(5), pp. 462-479

[91] Ursell F. (1952). Edge waves on a sloping beach, *Proceedings of the Royal Society A* 214(1116), pp. 659-593

[92] Yakhot V. and Orszag S.A. (1986). Renormalization group analysis of turbulence. I. Basic theory. *Journal of Scientific Computing* 1, pp. 1-51

[93] Yim S. C., Yuk D., Panizzo A., Di Risio M., Liu P. L.-F. (2008). Numerical Simulations of Wave Generation by a Vertical Plunger Using RANS and SPH Models*Journal of waterway, port, coastal and ocean Engineering.* 134, pp. 143-159

[94] Watts P., Grilli S.T., Kirby J.T., Fryer G.J., Tappin D.R. (2003). Landslide tsunami case studies using a boussinesq model and a fully nonlinear tsunami generation model. *Natural Hazards and Earth System Sciences* 3, pp. 391-402

[95] Wei G., Kirby J.T. (1995). A time dependent numerical code for extended boussinesq equations. *Journal of Waterway Port Coastal and Ocean Engineering-ASCE* 120, pp. 251-261

[96] Weibull W. (1939). A statistical theory of the strength of materials. *Ingeniors Vetenskaps Akademien, Handlingar* 151-3, pp. 45-55

[97] Weiss R., Fritz H.M., Wuennemann K. (2009). Hybrid modeling of the mega-tsunami runup in Lituya Bay after half a century. *Geophysical Research Letters* 36, L09602

[98] Wiegel R.L., Noda E.K., Kuba E.M., Gee D.M., Tornberg G. (1970). Water waves generated by landslides in reservoirs. *Journal of Waterway Port Coastal and Ocean Engineering-ASCE* 96, pp. 307-333